

Charles University in Prague  
Faculty of Mathematics and Physics

## Doctoral Thesis



### **Magnetic and transport properties of f-electron compounds under extreme conditions**

Martin Míšek

Department of Condensed Matter Physics

Supervisor: Doc. Mgr. Pavel Javorský, Dr.

Prague, 2012



## **Acknowledgements**

At this place, I would like to express my sincere thanks to all the people who helped me during my work on this thesis. My deepest gratitude belongs to my supervisor Doc. Mgr. Pavel Javorský, Dr. for his patient guidance and support throughout the whole PhD study.

I would like to thank RNDr. Jan Prokleška, Ph.D. for help with preparation of most of the experiments described in this thesis, as well as for his kind help with careful reading and finalizing this manuscript.

I wish to thank Ing. Jiří Kamarád, CSc. for introducing me into the area of high pressure physics and passing to me his extensive knowledge and experience in this field.

I am also grateful to Prof. RNDr. Vladimír Sechovský, DrSc. and RNDr. Zdeněk Arnold, CSc. who as the leaders of the group of magnetism at DCMP and the High pressure laboratory of IoP inspired and encouraged me to further continue in the study of magnetism and high pressure physics and for their help on numerous occasions on both professional and personal level.

This work could not be possible without high quality samples of studied materials. I would like to thank to Mgr. Klára Uhlířová, Ph.D., Mgr. Marie Kratochvílová and Mgr. Jiří Pospíšil, Ph.D. for preparing the single crystals of compounds studied in this work.

I am very thankful to Dr. Konstantin V. Kamenev and Dr. Anya F. Kusmartseva for allowing me to stay in the Centre for Science at Extreme Conditions during my PhD study and learn some advanced high pressure experimental techniques and many useful tricks for delicate experiments.

Finally, I would like to thank all my colleagues at DCMP and High pressure lab for friendly atmosphere and to all my friends and family for supporting me..

Thank You



**Název Práce:** Magnetické a transportní vlastnosti sloučenin s f-elektrony za extrémních podmínek

**Autor práce:** Martin Míšek

**Katedra/Ústav:** Katedra fyziky kondenzovaných látek

**Vedoucí doktorské práce:** Doc. Mgr. Pavel Javorský, Dr., Katedra fyziky kondenzovaných látek, Matematicko-fyzikální fakulta, Univerzita Karlova v Praze, Praha, Česká republika

**Abstrakt:** V této práci byl studován vliv vnějšího hydrostatického tlaku i jednoosého zatížení na magnetické vlastnosti vybraných sloučenin. Největší pozornost byla věnována sloučenině  $\text{ErCo}_2$ , jejím analogům s Dy a Ho na místě vzácné zeminy a vlivu substitucí Si na místo Co. V případě  $\text{ErCo}_2$  byla poprvé pozorována tlakem vyvolaná změna typu magnetického fázového přechodu z 1. druhu na 2. druh a separace uspořádání Er a Co magnetických podmříží, které byly předpovězeny v dřívějších pracích. V celé sérii byly úspěšně pozorovány anomálie objemových vlastností, spojené s existencí a krátkodosahovým uspořádáním Co momentů v paramagnetickém stavu ( $T > T_C$ ), které byly nedávno pozorovány za atmosférického tlaku pomocí experimentů XMCD.

Byla provedena série vysokotlakých experimentů s monokrystalem UNiGa, materiálu s výraznou anizotropií výměnných interakcí a bohatým magnetickým fázovým diagramem. Vedle působení hydrostatických tlaků byly studovány vlastnosti této sloučeniny také za jednoosého zatížení ve směru krystalografické c-osy její hexagonální struktury.

Významnou součástí práce bylo rozšíření dostupných experimentálních technik pro studium vlastností materiálů za působení vnějšího tlaku. Byly implementovány metody pro velmi citlivé měření střídavé magnetické susceptibility a měrné tepelné kapacity v pístových tlakových celách do tlaků  $\sim 3$  GPa v aparatuře PPMS (Quantum Design, 14 T magnet, 1,8 – 380 K). Dále byla zkonstruována a úspěšně otestována série nových tlakových komor pro studium objemových (DC magnetizace, AC susceptibilita, elektrická vodivost) i mikroskopických (rozptyl neutronů) experimentů za působení jednoosého zatížení vzorku v požadovaném směru. Završením instrumentální části práce potom bylo zkonstruování diamantové tlakové komory (DAC) pro měření magnetizací v komerčním SQUIDovém

magnetometru za působení extrémně vysokých tlaků. V prvních měřeních bylo dosaženo tlaků až 15 GPa, při zachování velmi vysoké citlivosti až do  $10^{-6}$  emu. Podle veškerých dostupných zdrojů v současnosti ve světě existuje pouze jedna další tlaková komora srovnatelných kvalit. Bez těchto pokroků v instrumentaci by nebylo možné pozorovat většinu fyzikálních jevů studovaných v této práci na reálných materiálech.

**Klíčová slova:** intermetalické sloučeniny kovů vzácných zemin, sloučeniny uranu, magnetické vlastnosti, vysoké tlaky

**Title:** Magnetic and transport properties of f-electron compounds under extreme conditions

**Author:** Martin Míšek

**Department/Institute:** Department of Condensed Matter Physics

**Supervisor of the doctoral thesis:** Doc. Mgr. Pavel Javorský, Dr., Department of Condensed Matter Physics, Faculty of Mathematics and Physics, Charles University in Prague, Prague, Czech Republic

**Abstract:** This thesis deals with the effect of hydrostatic and uniaxial pressures on the magnetic properties of selected compounds. Main emphasis was given to the ErCo<sub>2</sub> compound, its analogs with dysprosium and holmium at the rare-earth site and the influence of Si substitutions for the Co. In the case of pure ErCo<sub>2</sub>, we observed for the first time the pressure induced change of the type of the magnetic phase transition from the first to second order-type and the decoupling of the ordering of Er and Co magnetic sublattices. These effects were only theoretically predicted in the previously published works. Tiny anomalies in the bulk properties related to the existence and short-range ordering of Co magnetic moments in the paramagnetic phase ( $T > T_C$ ), recently deduced from the XMCD experiments at ambient pressure, were successfully observed in this high pressure study as well.

Series of high pressure experiments on the UNiGa single crystal, compound with high anisotropy and rich ambient-pressure phase diagram, has been performed. Besides the measurements under hydrostatic conditions, the experiments under uniaxial compression along the crystallographic c-axis of the compound's hexagonal structure, have been prepared as well.

Important aspect of the presented work lies in the instrumentation development for studying the material properties under high pressures. Methods for sensitive measurements of the AC susceptibility and the specific heat under high pressures were implemented for the piston-cylinder pressure cells under the pressures up to 3 GPa within the PPMS apparatus (Quantum Design, 14 T magnet, 1.8 – 380 K). Set of several new pressure cells for measuring both, the bulk (DC magnetization, AC susceptibility, electrical conductivity) and the microscopic (neutron diffraction) properties under uniaxial compression of the sample along desired direction, was constructed and successfully tested. Finally, the diamond anvil pressure cell for

precise magnetization measurement within commercial SQUID magnetometer under very high pressures has been constructed. Pressures up to 15 GPa have been achieved in the first tests, while preserving a remarkable sensitivity down to  $10^{-6}$  emu. To our best knowledge, there currently exist only one such a device in the world with comparable capabilities. Without this advances in the available experimental methods, most of the physical effects studied in this thesis would not be possible.

**Keywords:** rare-earth intermetallic compounds, uranium compounds, magnetic properties, high pressures

Prohlašuji, že jsem tuto disertační práci vypracoval samostatně a výhradně s použitím citovaných pramenů, literatury a dalších odborných zdrojů.

Beru na vědomí, že se na moji práci vztahují práva a povinnosti vyplývající ze zákona č. 121/2000 Sb., autorského zákona v platném znění, zejména skutečnost, že Univerzita Karlova v Praze má právo na uzavření licenční smlouvy o užití této práce jako školního díla podle § 60 odst. 1 autorského zákona.

V ..... dne.....

podpis



## Contents

<b>1</b>	<b>Introduction.....</b>	<b>13</b>
<b>2</b>	<b>General theory.....</b>	<b>17</b>
	2.1 Magnetic moments, Localized and Itinerant models.....	17
	2.2 Magnetic interactions.....	19
	2.3 Magnetism in uranium compounds.....	20
	2.4 Pressure influence on the magnetic properties of materials.....	21
<b>3</b>	<b>Experimental methods.....</b>	<b>23</b>
	3.1 Sample preparation and characterization.....	23
	3.2 Macroscopic techniques at ambient pressure – PPMS and MMPS apparatus.....	25
	3.3 Existing pressure cells in the JLMS.....	29
	3.4 Neutron diffraction.....	32
	3.5 AC calorimetry.....	35
<b>4</b>	<b>Results and discussion.....</b>	<b>39</b>
	4.1 New high pressure experimental options in the JLMS.....	39
	4.1.1 Introduction.....	39
	4.1.2 AC susceptibility in piston-cylinder pressure cells.....	41
	4.1.3 AC calorimetry in piston-cylinder pressure cells.....	45
	4.1.4 Diamond anvil cell for the magnetization measurements in SQUID magnetometer under very high pressures.....	49
	4.1.5 Uniaxial pressure cells.....	61
	4.1.6 Conclusions.....	65
	4.1.7 Plans for future development.....	66

4.2 Magnetism in $R(\text{Co}_{1-x}\text{Si}_x)_2$ under hydrostatic pressures.....	67
4.2.1 Introduction and previous results.....	67
4.2.2 Results and discussion.....	69
4.2.2.1 $\text{Er}(\text{Co}_{1-x}\text{Si}_x)_2$ .....	69
4.2.2.2 $\text{Ho}(\text{Co}_{1-x}\text{Si}_x)_2$ .....	79
4.2.3 Conclusions.....	81
4.3 Magnetism of UNiGa under uniaxial and hydrostatic pressures.....	83
4.3.1 Introduction and previous results.....	83
4.3.2 Results and discussion.....	88
4.3.2.1 Sample preparation and characterization.....	88
4.3.2.2 Experiments under hydrostatic pressures.....	89
4.3.2.3 Experiments under uniaxial pressure.....	94
4.3.3 Conclusions.....	101
4.4 Magnetism and superconductivity in selected $\text{CeTX}_5$ and $\text{Ce}_2\text{TX}_8$ compounds under high hydrostatic pressures.....	103
<b>5 Conclusions.....</b>	<b>107</b>
<b>Bibliography.....</b>	<b>113</b>

## Chapter 1 Introduction

Intermetallic compounds of the rare-earth metals and transition elements have been intensively studied for a long time, owing mainly to the fact that their behavior is in most cases considerably different compared to the properties of the constituent elements. Besides the large number of crystal structures, electronic ground states and complex magnetic phase diagrams, many unusual phenomena have been observed as well, e.g. non-Fermi liquid behavior, quantum criticality, coexistence of magnetic ordering and superconductivity and many others. Application of high pressure represents the way of well controllable and reversible tuning of the sample volume, resulting in changes of their crystal and electronic structure. Consequently, broad range of phenomena, arising from the modification of the nature of electronic states, has been observed in the condensed matter systems subjected to the external compression.

$\text{ErCo}_2$  and related compounds have been chosen as a main subject of this work owing to the instability of the cobalt sublattice arising from the proximity to the conditions for formation of magnetic moment. Naturally, such a system is highly susceptible to slight changes in the chemical composition and/or external conditions, such as an applied pressure. Indeed, various aspects of the itinerant electron metamagnetism in the  $\text{ErCo}_2$  compound have been thoroughly studied in the past. However, there were some open questions in the scenario of physics of these materials and some previously predicted effects that have not been observed up to now. In addition, the recent microscopic experiments (XMCD, SANS) demonstrated the existence and short-length correlations of the cobalt magnetic moments in the paramagnetic region, well above the Curie temperature of ferrimagnetic ordering,  $T_C = 33$  K at ambient pressure, rather surprising feature of this spectacular material.

Significant influence of the applied pressure can be generally expected also in the uranium compounds due to much higher spatial extent of the 5f-wavefunctions compared to the 4f-states of the rare-earths. Among the rare-earth based compounds, those containing cerium and ytterbium are particularly interesting for pressure studies owing to the proximity of their 4f-states to the Fermi energy and a tendencies for creating different (mixed and fluctuating) valence states.

The influence of hydrostatic and uniaxial pressure on the electronic properties of the uranium based system is demonstrated here on the case of UNiGa single crystal. This compound shows a huge anisotropy of magnetic interactions and a rich magnetic phase diagram - there exist five different antiferromagnetic phases below  $T_N = 40$  K already at the ambient pressure. Effects of high hydrostatic and uniaxial compression (along the crystallographic c-axis of the hexagonal structure) on the magnetic phase diagram have been thoroughly studied.

Another important part of this work lies in the instrumentation development for high pressure experiments. The other large areas of instrumentation (best example being magnets and cryostats) over the years went through such a development, that today most of the needed instruments are available commercially. There are, however, only few companies (e.g. Betsa [1], EasyLab [2]) which offer pressure cells and auxiliary equipment for high pressure experiments. Due to the fact, that the pressure cell design depends strongly on the type of considered experiment, the market is somewhat limiting. For this reason, most of the recognized high pressure facilities build their own experimental equipment tailored specifically to their research.

High pressure laboratory of the Institute of Physics of the Czech Academy of Sciences (IoP) has very long tradition in the instrumentation development for the experiments under extreme conditions. In the presented work, great deal of effort has been devoted to implementation of methods for basic bulk properties measurements using existing pressure cells as well as construction of several new pressure vessels. Most notably the successful construction of the diamond anvil cell for precise magnetic measurements in the commercial SQUID magnetometer under very high pressures and the series of uniaxial pressure cells for various types of experiments.

With regard to the modern topics in the physics of strongly correlated electronic systems, there is an ongoing work focused on the combination of high pressures and magnetic fields with very low temperatures, using the newly acquired He<sup>3</sup>/He<sup>4</sup> dilution refrigerator in the Joint Laboratory for Magnetic Studies (JLMS). Very recent experiments performed with the unique samples of novel cerium based magnetic superconductors, grown in the Technology lab (TL) of the Department of Condensed Matter Physics (DCMP) will be presented at the end of the text.

## **Thesis organization**

The thesis is organized as follows: Chapter 2 presents the theoretical background for the observed phenomena. Chapter 3 introduces the existing experimental methods for investigating the properties of studied compounds. Chapter 4 summarizes the results of the experimental work. This chapter is divided into four self-contained sections, each focused on one of the goals of the thesis. Each of these sections is introduced with an overview of previous results, where the motivation for the following work is clearly established, and is concluded by a short partial summary. First of these sections is devoted to the instrumentation development achieved during the author's PhD work, the second section presents a thorough high pressure study of selected members of the  $R(\text{Co,Si})_2$  family with the main focus on the  $\text{ErCo}_2$  compound. Third section of this paragraph shows the results of the uniaxial and hydrostatic pressure study of the  $\text{UNiGa}$  single crystal. The last section of this chapter presents the recent results of high pressure experiments performed on the novel Ce-based superconductors from the  $\text{CeTX}_5$  and  $\text{Ce}_2\text{TX}_8$  families ( $T =$  transition metal,  $X =$  p-element). All results are summarized and discussed in the Chapter 5.



## Chapter 2 General theory

### 2.1 Magnetic moments, Localized and Itinerant models

Material properties of solid compounds are mainly derived from the nature of electronic states in the considered system. As a good starting point for understanding the magnetic properties of materials, there are two basic approaches – the *localized* („free-ion like“) and the *itinerant* (magnetism of delocalized electrons) models.

The first of the above applies to the systems with the well localized electrons. This situation usually well describes the state of the rare-earth ions in compounds, where the magnetism originates from the unfilled 4f shell, lying well within the 5d and 6s shells. Despite the chemical environment within the solid compounds, the spatial localization and negligible overlap of the 4f wavefunctions of neighboring ions lead to the situation, where these states keep the similar character as in a free ions. As a consequence, the ground state can be described with the Hund’s rules, with the orbital moment  $L$ , spin  $S$  and total momentum  $J$  as a valid quantum numbers. These states do not contribute to conductivity or chemical bonding and from the point of view of the electronic band structure form (in most cases) a narrow band lying well below the Fermi energy.

The main characteristic of the itinerant model is a significant overlap of the electronic wavefunctions of the neighboring atoms. The resulting states are strongly delocalized, contribute to the conductivity and chemical bonding. As a consequence of the delocalization, the orbital momentum  $L$  is no longer a valid quantum number, the magnetism is mainly of the spin origin and the observed magnetic moments are in most cases lower compared to the value expected from the Hund’s rules in the free-ion model. This model is well established for the description of properties of elements with unfilled 3d (and 4d, 5d) electronic shells.

After the simplest model of the non-interacting electron gas [3] and the introduction of the electron band theory [4-6], the magnetism of delocalized electrons has been finalized by Stoner [7]. His phenomenological molecular field description (analogous

to the Weiss molecular field) incorporated the electronic band structure instead of the discrete energy levels. Stoner formulated his model with the following assumptions

- the states responsible for the magnetism are the unsaturated spins in the d-band
- exchange interactions are treated with the molecular field approximation
- Fermi-Dirac statistics has to be accommodated

Under these assumptions, the rule for the spontaneous ordering of the itinerant electrons, so called Stoner criterion, can be derived

$$I_S N(E_F) > 1 \quad .$$

Where  $I_S$  is the Stoner exchange integral [7] and  $N(E_F)$  is the density of state at the Fermi energy. The model can be understood as moving some of the electrons from the majority to the minority band. They must be shifted to higher energies in order to satisfy the Pauli exclusion principle. Related increase in their kinetic energy is compensated by the drop in the exchange energy and a new magnetic configuration is stable. Several types of magnetic materials can be distinguished by characterizing the value of the Stoner product  $I_S N(E_F)$

- $I_S N(E_F) < 1$  Pauli paramagnet
- $I_S N(E_F) \sim 1^-$  close to the onset of ferromagnetism, collective electron metamagnetism occurs
- $I_S N(E_F) \sim 1^+$  Stoner's criterion is fulfilled, but the spontaneous magnetization is small, the compound is called very weak itinerant ferromagnet
- $I_S N(E_F) > 1$ 
  - a) subbands with the opposite spins are not filled – weak ferromagnet
  - b) subband lying lower in energy is completely filled – strong ferromagnet

The transition from the low to the high magnetization state in the external magnetic field is called the metamagnetic transition. In the itinerant systems close to the fulfilling the Stoner criterion for the formation of band ferromagnetism, the field-induced ferromagnetic state can occur under the assumption of the strong positive curvature of the electronic density of states in the vicinity of the Fermi energy  $E_F$  [8] and the effect is called the itinerant electron metamagnetism. The main fingerprint of this phenomenon are the exchange enhanced susceptibility with the broad maximum around the ordering temperature, large high-field susceptibility and a significant sensitivity to external pressures and alloying.

Wolfarth, Rhodes and Shimizu [8-9] further developed a model suitable for describing the itinerant electron metamagnetism in the case of weak itinerant ferromagnets and the exchange enhanced paramagnetism. In these situations, the magnetization is small enough for the molecular field approximation to be applied and the Landau expression of the magnetic free energy in terms of magnetization can be used [10]. The coefficients of the expansion in the Landau series can be then used to characterize the type of magnetic material [11].

## 2.2 Magnetic interactions

The magnetic ordering originates from the exchange interactions between the magnetic moments. The basic types of exchange interactions is illustrated in Fig. 2.1. Direct exchange arises from the overlap of the wavefunctions of the neighboring atoms, the best example of the system governed by the direct exchange interaction are the 3d transition metal ferromagnets. In compounds, where the magnetic ions are separated with the nonmagnetic ones, the indirect exchange plays the dominant role. The interaction, mediated by the conduction electrons polarized by the

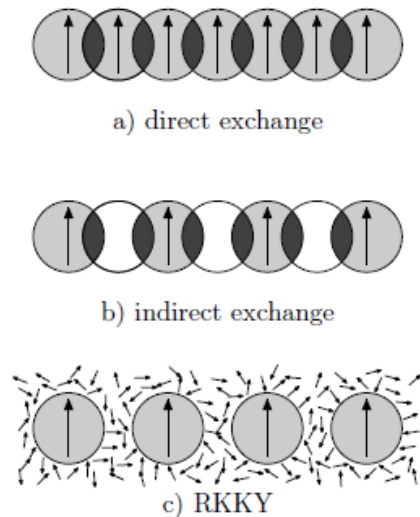


**Fig. 2.1:** Schematic representation of the different types of exchange interactions.

magnetic ions, is described by the *RKKY* model (Ruderman-Kittel-Kasuya-Yosida [6, 12]). The indirect exchange is much weaker (typically 0.1 – 10 meV compared to the 10 – 100 meV in the case of direct exchange in the 3d metals) and can play an important role only when the direct exchange is absent [13].

Formally, the exchange interactions between spins are treated with the Heissenberg-type hamiltonian [14]

$$\hat{H}_{ex}^{ij} = -2 \sum_{i,j} J_{ij} \hat{S}_i \hat{S}_j \quad (2.1)$$

where the  $\hat{S}_i$  and  $\hat{S}_j$  denotes the spin operators at  $i$ -th and  $j$ -th lattice site and  $J_{ij}$  is the exchange integral. The exchange integral  $\mathbf{J}$  can have either positive or negative sign, promoting the parallel or antiparallel orientation of the spins, respectively. The value of the  $\mathbf{J}$  depends on the distance between the  $i$ -th and  $j$ -th site, this dependence is derived from the microscopic mechanism of the exchange (direct vs indirect, nature of the electrons mediating the indirect exchange, etc.).

### 2.3 Magnetism of uranium in compounds

In uranium, the 5f electronic states, responsible for the magnetic properties, are more spatially extended when compared to the 4f wavefunctions of lanthanides. This leads to the stronger delocalization of the 5f electrons and their interaction with other ions in the lattice, both the direct interaction with a nearest uranium neighbor and the hybridization with the valence states of the neighboring non-uranium atoms in the lattice, these two being the most crucial ingredients of the magnetism in the uranium compounds.

In the case of the direct interaction, the most important role is played by the distance of the nearest uranium ions  $d_{U-U}$ . By the simple criterion, most of the uranium compounds can be classified either as a superconductors ( $d_{U-U} < 3.5 \text{ \AA}$ ) or being magnetically ordered ( $d_{U-U} > 3.5 \text{ \AA}$ ), where the  $d_{U-U} = 3.5 \text{ \AA}$  is called the Hill limit [15]. The appearance of the magnetic ground state is governed by Stoner like criterion with the width of the 5f band as a crucial factor.

To certain extent, the character of the 5f states resembles the one of the 3d states in transition metals and an electronic band description is suitable for the vast majority of uranium intermetallic compounds. One fundamental difference is the (usually) considerably narrower 5f band and a more pronounced role of the spin-orbit interaction in the actinides. The strong spin orbit coupling in actinides provides a mechanism for significant orbital polarization in the 5f band systems with consequent coupling of the 5f magnetic moments to the crystal structure, which is most evidently demonstrated by huge magnetocrystalline anisotropy. As a consequence the hard magnetization axis appears by rule perpendicular to the U-U nearest neighbor planes (chains) leading to the easy axis (easy plane) anisotropy [16]. The specific character of the 5f-electron magnetism in uranium compounds appearing somewhere between localized and itinerant behavior due to various 5f-5f overlap and 5f-ligand hybridization implies the sensitivity of magnetic properties to the variation of the external parameters like magnetic field, pressure or alloying with other elements.

## **2.4 Pressure influence on the magnetic properties of materials**

Application of external pressure affects the distances of the atoms in the crystal lattice and consequently the strength of the interactions between them. The possibility of changing the lattice parameters with the pressure then effectively provides a tool for „tuning“ of the related physical properties to a desired regime by modifying the strength of the interactions involved in the studied situation. In the solid state physics, the application of pressure can be used as a complementary tool to the chemical substitutions, which are commonly used for the same purpose. Moreover, the external pressure can be considered as a „pure“ alternative to them, since it does not directly bring any chemical changes into the investigated compound and the study of „intrinsic“ properties is possible. Given the complexity in research of many novel phenomena in the condensed matter physics, the high pressure is often an indispensable tool for unraveling the essential information of various competing mechanisms involved in the description of unusual physical properties of novel materials.

Effects of applied pressure on material properties largely depend on the initial state at the ambient conditions even in the relatively narrow selected class of materials. Due to the enormous diversity of systems studied under high pressures, formulation of general trends arising from the compression can be extremely difficult. To our best knowledge, last such attempt in the area of magnetism has been made more than three decades ago [17]. Despite this fact, few general remarks for the simple model situations can be made.

In some sense, the high pressure applied to the condensed matter tends to further support the trends observed in the condensation of the atoms into the solid state. As the interatomic distances are shortened, the overlap of the wavefunctions of neighboring atoms increases, enhancing the overlap integral, leading to the higher degree of delocalization of the electrons, broadening of the electronic bands and modification of bonding. Naturally, the outer electronic shells ( $\sim 3d$  metals) are more susceptible to such a changes, however, under sufficiently high pressure the same scenario would apply to the core states as well, ultimately leading to delocalizing entire electron cloud and forming a state similar to the Thomas-Fermi plasma. This is, however, far beyond the range of static high pressure experiments routinely accessible in laboratory. Realistic scenario for the types of materials ( $3d + 4f$  or  $5f$  electrons) and accessible pressures in this thesis (up to  $\sim 10$  GPa) can be characterized in the following way. Given the very low spatial extent of the  $4f$  states of lanthanides and their shielding by the  $5d$  and  $6s$  shells, influencing the  $4f$  moments with this kind of moderate pressures usually does not have any direct effect and the  $4f$  states can be only influenced by changes in the indirect mediated exchange. The exception represent various Ce- and Yb-based compounds, where the proximity of the  $4f$  states to the Fermi level and a tendency to completely fill/empty the  $4f$  shell leads to stronger sensitivity to the pressure compared to other lanthanides. On the other hand, the  $3d$  states of transition metals can be easily directly influenced. The increase in the overlap of the wavefunctions of the neighboring ions leads to the broadening of the  $3d$  band [17, 18], usually reducing the density of states at Fermi level and eventually suppressing the values of the induced magnetic moments and reducing the ordering temperatures.

## Chapter 3 Experimental methods

### 3.1 Sample preparation and characterization

All samples studied in this thesis have been prepared in the TL. The laboratory has been extensively updated in the last few years and today comprises the equipment for most of the known techniques for growing the high quality crystals [19]. Three different sample growth methods have been used for different samples studied in this work.

Polycrystalline samples have been prepared by the arc melting in the monoarc furnace, Fig. 3.1. Stoichiometric amount of the constituent elements is placed on the Cu crucible inside the chamber. The chamber is first evacuated (typically  $10^{-3}$  mbar) and then filled with the protective atmosphere of high purity Ar (6N), which serves as a charge carrier for the arc. The copper crucible and the upper electrode are both water-cooled. The sample is usually turned and remelted several times to reach better homogeneity. Alternative crucible



**Fig. 3.1:** Monoarc furnace for preparation of the polycrystalline samples

can be used to prepare the rod-like shaped polycrystals, e.g. for the single crystal growth using the zone melting within the optical furnace in TL.

First of the techniques used for the single crystal growth is the modified Czochralski method for pulling crystals from the melt. Triarc furnace made by the VAKUUM Praha [20], used in TL for this method, is shown in the Fig. 3.2.

Constituent elements are weighed and placed in the copper crucible. Due to the long time of the single crystal growth, small amount of elements with high evaporation may be added to reduce the possibility of the deviations from the ideal stoichiometry. Chamber is then evacuated ( $\sim 10^{-6}$  mbar) and the walls are heated to desorb the water and gases. After proper evacuation, the chamber is filled with protective atmosphere of pure argon (6N). Melt is heated by arcs provided by three symmetrically positioned electrodes. To improve the homogeneity of heating of the melt, the water-cooled crucible is rotating ( $\sim 5$  rpm). The melt is touched either by the polycrystalline seed of the material or the unsolvable tungsten rod and growing crystal is slowly pulled by lifting the rod up. Further information can be found in [21] and references therein. The typical size of the grown crystal is few centimeters in length and 3-5 mm in diameter.

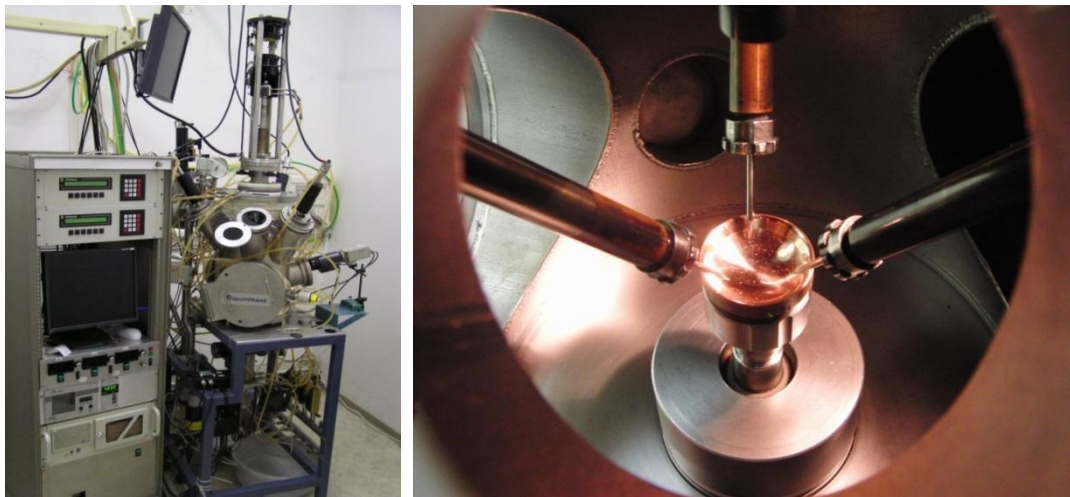


**Fig. 3.2:** Triarc furnace (VAKUUM Praha) for single crystal growth using the modified Czochralski method (left), detail of the copper crucible and the electrodes inside the apparatus (right).

Other method used for the preparation of the single crystals is called „molten metal solution growth“ or simply „flux growth“. The method resembles the common way of growing crystals from the solution (i.e. NaCl dissolved in water), the solvent here is however metallic. Naturally, higher temperatures well above the room temperature are needed. To keep the saturation of the solvent, cooling of the solution is used instead of the evaporation of the solvent. The method offers two great

advantages over the Czochralski technique. First, growing the crystals of the incongruently melting materials is possible. Secondly, the compounds containing the elements with high vapor pressure (e.g. Mn or Yb) can be prepared without the unwanted changes in the stoichiometry of the melt. There are many parameters (e.g. type and composition of the flux, cooling schedule) that have to be considered for successful crystal growth and the experience of the experimenter plays the crucial role. The crystals of the  $\text{Ce}_2\text{PtIn}_8$  and  $\text{CeRh}_{0.75}\text{Pd}_{0.25}\text{In}_5$ , studied in this work have been grown by RNDr. Klára Uhlířová, Ph.D. and Mgr. Marie Kratochvílová. Detailed description of the flux-growth technique can be found in [22] and references therein.

As-cast samples suffer from the rapid cooling of the melt after the arcs are discontinued, leading to material stresses and imperfect occupancy of the correct atomic positions. Equilibrium state, where the atoms occupy the proper sites and the stresses are released, can be achieved by annealing. For this purpose, TL is equipped with the series of furnaces, which offer smoothly controlled annealing up to the temperatures  $1800^\circ\text{C}$ . As-cast samples are sealed in the quartz tubes under high vacuum  $10^{-5} - 10^{-6}$  mbar. Samples are usually wrapped in the tantalum foil to prevent the reaction with the silicon from the quartz tube walls. The temperature and duration of the annealing strongly depends on the particular material under consideration.

X-ray powder diffraction is used for the basic structural characterization of prepared samples. Two diffractometers - Bruker D8 Advance and Seifert XRD7 - can be used for the powder x-ray diffraction experiments. Bragg-Brentano geometry and Cu  $K_{\alpha 1}$  radiation ( $1.540598 \text{ \AA}$ ) has been used in both cases. Small piece of the sample is pulverized into the fine powder, which is then attached on a glass with an Apiezon grease. The Fullprof program [23] with implemented Rietveld analysis procedure [24] is used to process the measured diffraction spectra.

Laue x-ray diffraction in the back-reflection geometry has been used to orient the single crystals and check their quality. Micrometa 600 apparatus with polychromatic Cu radiation at 30 kV potential has been used. The Laue patterns have been recorded on the photostimulable phosphor plates and analyzed on Scanner Vista Scan (Duerr). Compared to the classical films, the phosphorous plates offer much higher sensitivity, leading to much shorter times necessary to record the data ( $\sim 10$  min). No solutions are needed to evaluate the patterns and plates can be erased and used again (up to  $\sim 1000$  cycles). The orientation of the crystals is deduced from

the symmetry of recorded patterns, the sharpness of the reflections is considered as a sign of good/poor quality of the crystal.

Convenient way for analyzing the composition of the samples is the microprobe analysis. This technique is based on analysis of the x-ray radiation emitted by the sample subjected to the high voltage electron beam. Each element has a characteristic spectra. The energy of the emitted lines corresponds to the element and intensity is proportional to the content of the element in the studied area on the sample. Penetration depth of the electrons is up to  $\sim 0.5 \mu\text{m}$  (depending on their energy), this has to be considered when analyzing objects of comparable size. This analysis has been performed on the scanning electron microscope Tescan Mira I LMH with the energy dispersive x-ray detector Bruker AXS.

In addition, the TL is equipped with several machines for final forming of the samples to a shape preferable for the experiment. Spark-erosion cutter and the wire saw with the SiC abrasive can be used for cutting the sample to desired dimensions. Grinder/polisher (Boehler) with the diamond paste (1 – 10  $\mu\text{m}$  grains) is used for fine finish of the sample surfaces, required for many experiments, i.e. the microprobe analysis or the uniaxial pressure experiments.

### **3.2 Macroscopic techniques at ambient pressure – PPMS and MPMS apparatus**

All bulk properties of the studied compounds have been measured in JLMS, conducted by the Department of Condensed Matter Physics of the Faculty of Mathematics and Physics, Charles University in Prague and the Institute of Physics of the Academy of Sciences of the Czech Republic. The laboratory is equipped with a commercial SQUID magnetometer with a 7 T magnet (MPMS7, Quantum Design [25]), two PPMS apparatus (Physical Property Measurement System, Quantum Design) with 9 T and 14 T magnet, respectively and the He<sup>3</sup>/He<sup>4</sup> dilution refrigerator (Leiden Cryogenics), has been added to the portfolio only very recently.

## **PPMS9 (14) apparatus**

Physical Property Measurement System (PPMS) is a versatile instrument offering the options for measuring a large variety of physical properties. Basic setup consist of dewar with the superconducting magnet, pump for evacuating the sample chamber, power source and a lock-in amplifier. The chamber incorporates an universal 12-pin platform and each of the experimental options uses its own specific insert. Machine is controlled by sophisticated user friendly software (MultiVu [26]), which provides easy control over the environment conditions during the experiment. Most of the experimental options can be operated in the temperature range 1.8 – 400 K with applied magnetic fields up to 9 T (14 T).

### **Magnetic measurements**

Basic magnetic characteristics of the sample can be measured within the PPMS apparatus using the ACMS (AC Measurement System) and VSM (Vibrating Sample Magnetometer) options. First of them uses the set of excitation and detection coils to measure the DC magnetization (extraction method – sample, attached to a thin rigid rod, is moved through the coils) or AC susceptibility (inductive measurement) of the sample. The drive coil is able to generate the driving fields with the amplitude up to 10 Oe in a frequency range 10 Hz to 10 kHz. In the case of the VSM, the system oscillates the position of the sample with respect to the detection coil set and synchronously record the induced voltage. This setup provides very fast measurement of the DC magnetization of the sample with very good sensitivity down to  $10^{-6}$  emu. In addition, the complementary oven can be used to extend the temperature range up to 900 K.

### **Electrical transport measurements**

AC Transport measurement system incorporates a precision current source with a resolution 0.2  $\mu$ A and maximum output 2 A, currents with frequency 1 Hz – 1 kHz can be used. Standard four-probe method is used to measure the resistivity of studied samples. Advantage of this technique lies in the elimination of the contribution of the contacts and wires and consequent ability to detect very small signals. Minimizing

the resistivity of contacts of the attached wires is important not only to provide better sensitivity of the measurement but also to minimize the heating of the sample during the measurement. In most cases, either a colloidal silver or the conductive low-temperature epoxy has been used. Recently, custom-made machine for spot-welding of the thin (20-50  $\mu\text{m}$ ) golden wires has been built and successfully used in the JLMS for contacting the samples for the transport measurements. This proved to be extremely helpful namely for the experiments in very low temperatures ( $\text{He}^3$  insert in PPMS, dilution refrigerator) and in some cases for contacting extremely tiny samples prepared by the flux-growth method. The apparatus allows the simultaneous measurement of two samples. Alternatively, electrical resistivity and a Hall voltage can be both measured in one experiment.

### **Specific Heat**

The PPMS apparatus utilizes the  $2\tau$ -relaxation method for the specific heat measurements. The relaxation calorimeter consist of a  $3 \times 3 \text{ mm}^2$  alumina platform, connected to the puck by eight thin wires. The Cernox thermometer (Lakeshore) and a RuO thin-film heater are attached to the bottom side of the platform. The sample is attached to the platform with a small amount of the Apiezon N grease. The sample puck is sealed with a cap that acts as a radiation shield and placed inside the chamber under high vacuum ( $<10^{-3}$  mbar). In the experiment, the platform is heated above the reservoir temperature and then left to relax. The decay can be described by two exponential components, depending on thermal link between sample and the platform. The relaxation process is recorded and the value of the sample specific heat is obtained from the fit of the data. Before the measurement with the sample, the heat capacity of puck with the grease is measured separately.

### **MPMS7 SQUID magnetometer**

The MPMS7 commercial SQUID magnetometer can be considered as modification of the extraction method for the magnetization measurement. Advantage over the „classic“ method comes from the use of superconducting material for the detection coils instead of the classical ohmic conductor. The detection coil consists of the loop of superconducting wire separated by two Josephson's junctions. The voltage

between the two junctions is a periodic function of the magnetic flux inside the loop. Compared to the conventional magnetometers, the SQUID offers much higher sensitivity. In principle, signals corresponding to the magnetic flux quantum  $\hbar/2e$  can be detected. The scheme of the magnetometer is in the Fig. 3.3 (left). Typical response curve, i.e. induced voltage as a function of the position of the sample with respect to the coil set. is shown in the Fig. 3.3 (right). The sensitivity of the MPMS7, as declared by the manufacturer Quantum Design, is  $10^{-7}$  emu.

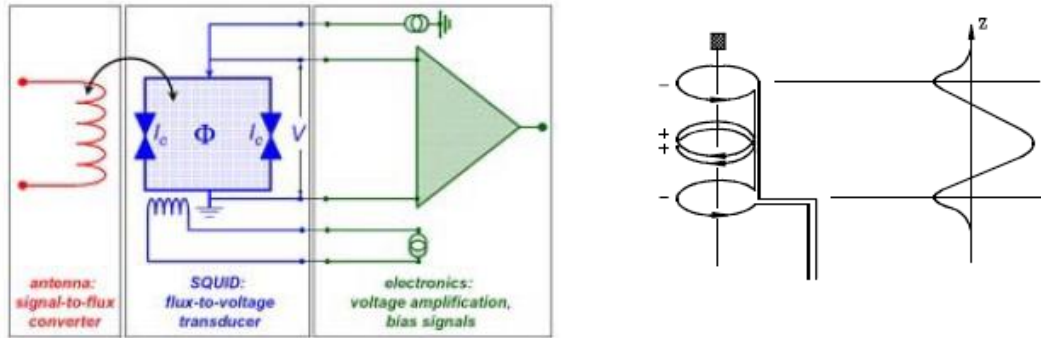


**Fig. 3.3:** Scheme of the MPMS SQUID magnetometer (left), geometry of the detection coils and typical sample-response curve (right)

### 3.3 Existing pressure cells in the JLMS

#### Pressure cell for magnetization measurements in the MPMS7

Piston-cylinder type of pressure cell for the magnetic measurements within the commercial SQUID magnetometer (MPMS7, Quantum Design) has been constructed in the IoP [27]. The cell is shown in the Fig. 3.4, Fig. 3.5 shows the scheme and parts of the cell in detail.



**Fig. 3.4:** Hydrostatic piston-cylinder pressure cell for the magnetization measurements in the MPMS SQUID magnetometer.

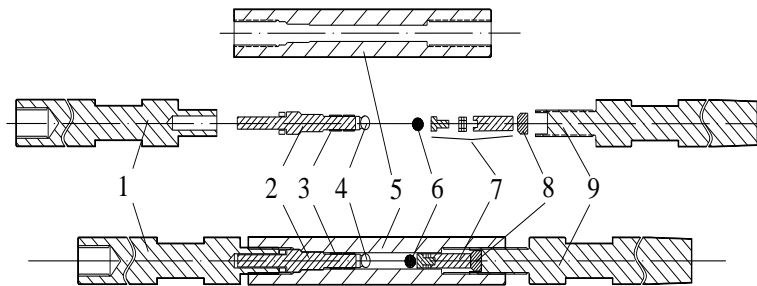


**Fig. 3.5:** 1-upper clamping bolt, 2-plug, 3-plug sealing rings, 4-sample holder with sample, 5-body of the cell, 6-lead manometer, 7-piston, 8-piston backup, 9-lower clamping bolt.

All parts of the cell, except for the sealing rings is made from non-magnetic CuBe alloy. Outer diameter of the cell's body is 8.6 mm, the diameter of the sample area inside the cell is 2.5 mm. The plug with the sample holder is sealed with the combination of one plastic and one Sn-coated copper sealing ring. The piston on the other side of the cell is sealed using the so called „Bridgman Mushroom“ [28, 29]. The piston consists the of mushroom-shaped top and a hollow cylinder. A set of thin metallic rings with different hardness (Cu-Sn-In-Cu) is placed between the two parts. Due to the unsupported area under the mushroom's „leg“, the pressure in the metallic sealing rings exceeds the pressure inside the sample chamber, the liquid pressure medium is then successfully sealed inside and the cell can be pressurized.

The construction of the pressure cell uses the autofrettage procedure with the hardened CuBe alloy [30] to increase the maximum load, that can be supported by the body of the cell. The maximum pressure that can be safely generated is ~1.2 GPa. OL-3 spindle oil is used as a pressure transmitting medium. Pressure in the cell is determined in the low temperatures by the shift of the superconducting transition of the lead sample [31], which is placed at the bottom of the cell. More details of the construction together with functional and destruction tests can be found in [27].

### **Pressure cell for PPMS apparatus**

The piston-cylinder pressure cell for the PPMS apparatus, designed by Prof. Takashi Naka (NIMS, Tsukuba) is shown in the Fig. 3.6. The cell uses the double layered construction, where the initial diameter of the inner cylinder slightly exceeds the

inner diameter of outer part (by  $\sim 20 \mu\text{m}$ ). The two parts are assembled together by cooling the inner part, heating the outer one and using the open space created momentarily by the thermal expansion/contraction of the two parts. Once the thermal equilibrium is reached, the mismatch in the original size results in the pre-tension on the interface of the cylinders, which allows achieving higher pressures compared to the single-wall cylinder of the same diameter. The outer part is made of the CuBe alloy, the inner part is from the NiCrAl.

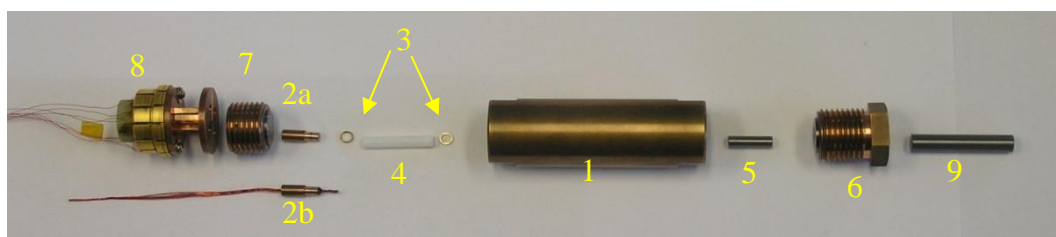


**Fig. 3.6:** Double layered CuBe/NiCrAl piston-cylinder pressure cell for the PPMS apparatus. 1- body of the cell, 2a-plug, 2b-plug with sealed Cu wires, 3-CuBe sealing rings, 4-PTFE capsule, 5-nonmagnetic WC piston, 6-upper clamping bolt with the WC piston support, 7-lower clamping bolt with the WC plug back-up, 8-modified PPMS puck, 9-WC rod for applying the load in the hydraulic press.

Inner diameter of the pressure cell is 4 mm. The sample assembly is sealed inside the teflon capsule with the diameter of the working space  $\sim 3$  mm. Two non-hardened CuBe rings are used to seal the teflon capsule on both sides. The CuBe plug allows to lead 10-12 copper wires ( $50\text{-}80 \mu\text{m}$ ) inside the cell. The wires are fixed in the plug by the Stycast 2850 FT epoxy. The Daphne 7373 is used as a pressure transmitting medium and the pressure inside the cell is determined by the resistive manganin manometer [18].

This pressure cell was originally intended for the measurements of electrical resistivity. However, any quantity that can be transformed to the electric current/voltage can be in principle measured as well. Some instrumental advancements have been achieved in the JLMS, the results are reported in the Chapter 4.1.

### 3.4 Neutron diffraction

Neutron diffraction is a powerful tool for investigating properties of the condensed matter systems. Reason for this comes from several unique properties of neutrons. Absence of the electrical charge gives rise to a long penetration depth of neutrons into the matter (order of few centimeters) compared to the charged particles which can see only thin surface layer of the sample. The wavelength of the thermal neutrons is comparable to the interatomic distances within the solid compounds and can be therefore used for investigating their structure on the microscopic level. Neutrons are scattered by the nuclei of the atoms in the studied sample, bringing a complementary information to the x-rays, which are scattered by the electrons. Consequently, the scattering length, describing the scattering process of neutrons on the nuclei, is rather random function of the atomic number, compared to the smooth dependence of the atomic form factor in the case of the x-rays. This has substantial consequences for various experimental situations. Most notably, the structures containing light elements (hydrogen, oxygen) in the presence of the heavy atoms can be successfully studied and different isotopes of the same element can be distinguished. Due to the  $S = 1/2$  spin, neutron bears a magnetic moment and interacts with magnetic moments in the sample via the dipole-dipole interaction. This attribute is widely used for investigating the magnetic structures and excitations in solids. In addition, incident neutron beam can be prepared in the polarized state and used to separate magnetic and nuclear contributions to the scattered intensities.

The scattering process is described by double differential cross-section (3.1) for neutrons scattered into the spatial angle  $\Delta\Omega$  within the energy  $\Delta E$ . With the initial state characterized by the energy  $\hbar\omega_i$ , wavevector  $\mathbf{k}_i$  and polarization  $\rho_i$ , which is scattered to the final state ( $\hbar\omega_f$ ,  $\mathbf{k}_f$  and  $\rho_f$ ), the Fermi Golden rule can be used to calculate the double differential cross-section [32]

$$\frac{d^2\sigma}{d\Omega d\omega} = \frac{|k_f|}{|k_i|} \left( \frac{m_n}{2\pi\hbar^2} \right)^2 \sum_{\lambda, \rho} \left| \langle k_f \rho_f \lambda_f | U | k_i \rho_i \lambda_i \rangle \right|^2 \delta(\hbar\omega + \hbar\omega_i - \hbar\omega_f) \quad (3.1)$$

where the sum runs over all initial and final states. The interaction potential  $U$  contains both, the nuclear and magnetic contributions to the scattering process. The delta function represents the conservation of the energy. Depending on the energy

transfer, two situations – elastic and inelastic scattering – can be distinguished. Given the main interests of this thesis, only the elastic scattering (i.e. the energy transfer  $\hbar\omega = 0$ ) is considered in the following text.

With the dimensions of the atomic nuclei being much smaller compared to the neutron wavelength under consideration, the potential for the nuclear scattering can be described with the delta function

$$U_N(\vec{r}) = \frac{2\pi\hbar^2}{m_n} \sum_j b_j \delta(\vec{r} - \vec{R}_j) \quad (3.2)$$

where the summation goes over the unit cell. Using the potential (3.2) in the equation (3.1), the differential cross section can be rewritten in the following form

$$\frac{d^2\sigma}{d\Omega d\omega} \approx \langle b \rangle^2 e^{-i(\vec{k}_i - \vec{k}_f)(\vec{R}_j - \vec{R}_{j'})} + N(\langle b^2 \rangle - \langle b \rangle^2) = \left( \frac{d^2\sigma}{d\Omega d\omega} \right)_{\text{coh}} + \left( \frac{d^2\sigma}{d\Omega d\omega} \right)_{\text{incoh}} . \quad (3.3)$$

The incoherent part of the cross section is independent of the spatial variables, therefore it does not result in any reflections and only causes uniform increase of the background signal and lower signal to noise ratio. Finally, the coherent elastic nuclear contribution to the can be rewritten into the formula

$$\left( \frac{d\sigma}{d\Omega} \right)_{\text{Cohelast,nucl.}} = \frac{(2\pi)^3}{V_{\text{cell}}} \sum_{\vec{r}} |F_N(\vec{Q})|^2 \delta(\vec{Q} - \vec{r}) \quad F_N(\vec{Q}) = \sum_j b_j e^{i\vec{Q} \cdot \vec{R}_j} \quad (3.4)$$

where the nuclear form factor  $F_N(\mathbf{Q})$  contains all information on the structure of investigated material,  $\mathbf{Q} = \mathbf{k}_i - \mathbf{k}_f$  is the momentum transfer and the delta function on the right side of the cross-section formula represents the Bragg's law [33].

Neutron with the magnetic dipole moment  $\mu_n = -\gamma_n \mu_N \boldsymbol{\sigma}$  ( $\gamma_n = -1.913$  is the gyromagnetic factor of neutron,  $\mu_N$  is the nuclear magneton and  $\boldsymbol{\sigma}$  is the spin operator) interacts with magnetic field  $\mathbf{B}(\mathbf{r})$  of the electrons in the sample

$$U_M(\vec{r}) = - \sum_j \vec{\mu}_N \cdot \vec{B}_j(\vec{r} - \vec{R}_j) . \quad (3.5)$$

The magnetic field  $\mathbf{B}_j(\mathbf{r})$  can be expressed [34] as

$$B_j = B_j^S + B_j^L = \nabla \times \left( \frac{\vec{\mu}_e \times \vec{r}_j}{r_j^3} \right) - \frac{e \vec{v}_e \times \vec{r}_j}{c r_j^3} \quad (3.6)$$

Using this expression and potential (3.5) in the (3.1), quantity analogical to the nuclear scattering length can be introduced [34]

$$b_j^M(\vec{Q}) \approx \vec{Q}_1 \times M_j(\vec{Q}) \times \vec{Q}_1 = \vec{M}_{j\perp}(\vec{Q}) \quad (3.7)$$

where  $\mathbf{Q}_1 = \mathbf{Q}/|\mathbf{Q}|$  is normalized vector in the direction of the momentum transfer and  $\mathbf{M}_{j\perp}(\mathbf{Q})$  is the component of the Fourier transform of the sample magnetization perpendicular to the scattering vector  $\mathbf{Q}$

$$\vec{M}_j(\mathbf{Q}) = \int \vec{M}_j(\vec{r}) e^{i\vec{Q}\cdot\vec{r}} d\vec{r} \quad (3.8)$$

The magnetic contribution to the cross-section can be then written in similar way

$$\left( \frac{d\sigma}{d\Omega} \right)_{\text{Coh.elast.,magn.}} = \frac{(2\pi)^3}{V_{\text{cell}}} \sum_{\vec{\tau}} \sum_{\vec{q}} |F_M(\vec{Q})|^2 \delta(\vec{Q} - \vec{\tau} - \vec{q}) \quad (3.9)$$

With the magnetic structure factor  $F_M(\mathbf{Q})$  and the propagation vector  $q$ . Diffraction condition is now modified to  $\mathbf{Q} = \boldsymbol{\tau} + \mathbf{q}$ , where the propagation vector  $\mathbf{q}$  bears the information about the periodicity of the magnetic structure. As a consequence of (3.7), only the component of the magnetization perpendicular to the scattering plane can be observed. This is particularly important for the single crystal diffraction experiments which have to be carefully planned in order to obtain the desired information about the magnetic structure of the sample. The nuclear and magnetic contributions can be very often hard to separate. Usual way is to compare the data taken in the paramagnetic region with the data recorded in the magnetically ordered state.

Experiments described in this thesis has been carried out on the D10 and VIVALDI (Very Intensive Vertical Axis Laue Diffractometer) instruments in the Institute Laue-Langevin, Grenoble. The D10 is a conventional four-circle

diffractometer. The VIVALDI instrument uses a cylindrical imaging plate detector covering the  $\pm 144^\circ$  in the  $2\theta$  and  $\pm 52^\circ$  in  $\nu$ , resulting in the 2D projection of the huge volume of the reciprocal space in single recorded Laue pattern. The geometry of the instrument allows to use the standard „Orange“ cryostat down to  $T \sim 1.5$  K. The use of the white neutron beam allows a fast measurement, however the data evaluation can be difficult. The wavelength of the given spot can not be easily identified and the Bragg's law can not be directly used to determine the distance of reflecting planes. Laue patterns taken at the ambient temperature have been indexed by the LAUEGEN program [35], using the structural information provided by the x-ray powder diffraction prior to the neutron experiment. Detailed description of the procedure used to index the magnetic reflections can be found in [36].

### 3.5 AC calorimetry

Simply speaking, the basic idea behind the AC calorimetry technique is observing the temperature oscillations of the sample subjected to periodic heating. Equation (3.9) describes the balance of heat supplied by the heater (left term) with the heat absorbed by the sample (first term on right side) and the heat dissipated into the surroundings (second term on the right side)

$$(p_0 + p \sin \omega t)\Delta t = mc\Delta T + P(T)\Delta t \quad (3.10)$$

Under the assumptions of small deviations from the base temperature and the linearity of the dissipation term

$$T = T_0 + \Theta, \Theta \ll T_0 \quad P(T) = P(T_0) + P'\Theta \quad (3.11)$$

the equation (3.9) can be rewritten in the following form

$$p_0 + p \sin \omega t = mc\dot{\Theta} + P(T_0) + P'\Theta \quad (3.12)$$

which can be easily solved, leading to the result

$$\begin{aligned} \Theta &= \Theta_0 \sin(\omega t - \Phi) \\ \Theta_0 &= (p / mc\omega) \sin \Phi \\ \tan \Phi &= mc\omega / P' \end{aligned} \quad (3.13)$$

Generally, both amplitude and phase of the resulting oscillations contain information about the specific heat of the sample. The amplitude  $\Theta$  is inversely proportional to the mass and specific heat of the sample and the frequency of oscillations and scales linearly with the supplied power, the phase shift carry the information about the dissipated heat. In special case, when  $mc\omega \gg P^c$  (i.e. „quasi“ adiabatic conditions), the equations (3.13) turns to a simpler form

$$\Phi \approx \pi/2 \quad \Theta_0 = p/mc\omega \quad . \quad (3.14)$$

The Sullivan and Siedel [37] went further in the analysis of the situation and taken into account the finite dimensions and thermal conductivity of the sample, finite heat capacity of the heater and thermometer and a links between the sample, heater, thermometer and the heat bath. Their detailed consideration of the experimental arrangement leads to two important conclusions. First, the equation for the amplitude of the oscillations is modified

$$\Theta_0 = \frac{P}{2\omega C} \left[ 1 + \frac{1}{\omega^2 \tau_1^2} + \omega^2 \tau_2^2 + \frac{2K_b}{3K_s} \right]^{-1/2} . \quad (3.15)$$

where  $\tau_1$  is the sample to bath relaxation time and the remaining time constants have been lumped into  $\tau_2$ . The basic characteristic is preserved, the amplitude keeps the same proportionality to the supplied power and the specific heat of the sample. Additional frequency dependent term simply identifies the limiting conditions for the experiment. In the very low frequencies, the energy supplied by the heater is immediately dissipated and no oscillations are observed, whereas in the high frequency limit, the oscillations are to fast considered the thermal links between all elements of the experimental assembly and the observer is unable to follow such a rapid changes. Frequency characteristic arising from this equation is illustrated in the Fig. 3.7. For the succes of the experiment, it is important to measure this dependence and choose the frequency for the measurement from the middle „plateau“, far from both limiting cases.

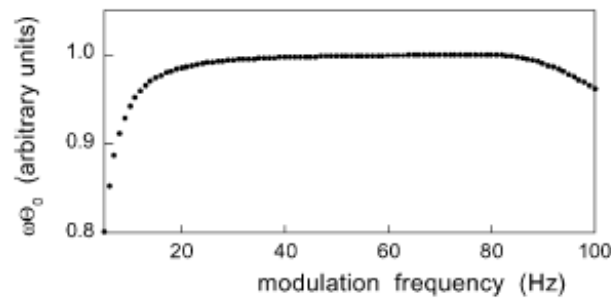


**Fig. 3.7.** Typical frequency characteristic of the experimental assembly, from [37].

Unlike most other calorimetric techniques, the AC calorimetry is suitable for the high pressure experiments since it inherently takes into account the dissipation of the heat from the sample to the surroundings, i.e. the direct contact of the sample with the pressure medium (heat bath). Moreover, the massive body of the pressure cell, which presence makes serious problems in other calorimetric methods is no longer an issue here. Besides the AC calorimetry for measuring the specific heat, analogous modulation techniques can be employed for measuring other quantities, i.e. thermal conductivity, dilatometry, electrical resistivity, thermopower, spectral absorbance, etc. Comprehensive overview of the wide variety of modulation measurement techniques together with detailed considerations for the experimental arrangements can be found in [38]. Beautiful example of the technique implemented for the high pressure experiments can be found e.g. in [39, 40]. Results of our realization of the experiment is presented in the Chapter 4.1.2.



## Chapter 4 Experimental results and Discussion

### 4.1 New high pressure experimental options in JLMS

#### 4.1.1 Introduction

As discussed before, the application of high pressure on the studied material is an interesting option for investigating the underlying physics of many interesting phenomena observed in condensed matter physics. It motivated us to dedicate our efforts to the advances in experimental methods available in the JLMS for studying material properties under high pressures. Although the high pressure instrumentation development in the High pressure laboratory of IoP has very long tradition and provided solid basis for our research over the years, the existing high pressure experimental options described in Chapter 3, were somewhat limiting in our current research objectives. In this section, we present new techniques implemented for existing pressure cells as well as the design of several new pressure devices, which both dramatically extended and improved the standards of obtainable information for the presently studied strongly correlated electron materials.

First subsection summarizes the AC susceptibility measurements under high hydrostatic pressures. The AC susceptibility experiments with the existing SQUID cell [26], described in Chapter 3, are possible but often provide only very rough data due to the parasitic signal from the pressure cell itself. Moreover, the maximum available pressure here is only 1.2 GPa. As the AC susceptibility measurement is one of basic magnetic characterization tools, our main ambition was to significantly improve the sensitivity of measurement and extend the range of available pressures. The work was also motivated by the recent developments in the scenario of physics of some  $R\text{Co}_2$  compounds studied on our department, which will be discussed in detail in the Chapter 4.2.

The second subsection deals with the implementation of the AC calorimetry technique for measuring the heat capacity under high pressures. Since the heat capacity is a quantity which to some extent reflects majority of processes in the condensed matter systems, it is highly desirable to master the heat capacity measurements of samples exerted to high pressures. For most of the widely used

calorimetric techniques the presence of the pressure cell introduces a substantial obstacle since the mass of the sample is typically three (or more) orders of magnitude lower than the mass of the pressure cell. Although some effort to miniaturize the pressure cells for the standard relaxation method measurements were made, reasonable results were only reported for limited choice of materials and environment conditions [41]. On the other hand the AC calorimetry, introduced in the Chapter 3.5, proved to be the only viable experimental option for measuring the heat capacity of large variety of samples in wide spectrum of sample environments. Despite the fact that AC calorimetry and the related modulation techniques are known for relatively long time [38], the experiment under high pressure presents several instrumental challenges and results reported in scientific literature are still quite rare.

The third subsection describes the experiments under uniaxial compression. This is particularly interesting experimental option for materials with pronounced anisotropy of magnetic exchange interactions. Unlike the hydrostatic pressure experiments, where the sample is compressed in all crystallographic directions and volume is reduced, here the sample is loaded only in one desired direction. Shrinking of the crystal lattice in this direction is compensated with expansion in the perpendicular plane, leaving none (or very small) volume change. Consequently, the combination of both, uniaxial and hydrostatic experiments with the magneto-elastic measurements can provide essential information about the relation of the crystal structure to the magnetic properties of studied samples. Design of several new uniaxial pressure cells and peculiarities of their operation are described in this section as well as details of experimental setup for the magnetization measurement in the SQUID magnetometer, electrical resistivity in PPMS and neutron diffraction experiments under uniaxial stress.

The last subsection of this chapter is devoted to the diamond anvill cell (DAC in further text) for direct magnetization measurements in the SQUID magnetometer under very high pressures, which has been recently developed in the High pressure laboratory of the Institute of Physics ASCR. An obvious motivation here was to significantly extend the available pressure range for our experiments. Compared to piston-cylinder vessels where pressures only up to few GPa can be generated, the DACs allows one to access much higher pressures (of order of few hundred GPa [42]). For the purposes of our research interests we decided that the first pressure cell

of this type should be the one for magnetization measurements using the commercial SQUID magnetometer. Limitations given by the available space within the magnetometer sample chamber (9 mm in diameter) caused serious problems with using the „traditional“ design of the cell [42] and presented a huge challenge to the whole high pressure community in recent years. Compared to other types of experiments (e.g. x-ray diffraction, optical experiments, electric transport properties), where DAC's are routinely used for a long time and commercially available, there have been only few groups which reported successful development of the DAC for measurements in the SQUID magnetometer [43 - 45]. Construction of our SQUID-DAC is thoroughly discussed within that paragraph. The results of the first functional tests, which demonstrate excellent capabilities of both, generating very high pressures and obtaining precise data, are presented as well.

Finally, we would like to outline the possible future development of the high pressure instrumentation in our laboratories. The recent acquisition of the new dilution refrigerator in the JLMS opens a possibility to get involved in several research topics, which are currently major concern for both scientific communities of high pressure physics and strongly correlated electronic systems. This will require to continue further with designing new pressure cells for various types of experiments and use methods already implemented in piston-cylinder cells (sections 4.1.2 – 4.1.3) in the diamond anvil cells as well. Feasible experimental improvements will be presented in this final paragraph.

#### **4.1.2 AC susceptibility measurement in piston-cylinder pressure cells**

First attempts to measure magnetization under pressure appeared in the late 60's, however, due to the limited sensitivity of then used magnetometers, results were quite unique, few works were reported e.g. by Vettier [46] and Kouvel [47]. On the other hand, AC susceptibility measurements were relatively common, mainly due to the reasonable sensitivity even with relatively simple experimental setup. Experimental arrangement usually consisted of few turns of wire wound directly around the sample serving as a detection coil with the excitation coil being placed outside the pressure cell or with a sample of the toroidal shape and a „transformer“ arrangement of the two coils around it, both inside the pressure apparatus [48]. Magnetic measurements under high pressures became more common only after the

advent of the commercially available SQUID magnetometers in the early 90's with the subsequent introduction of the first pressure cells designed for this purpose independently by T. Goto [49] and J. Kamarád [27]. The latter one has been described in detail in the Chapter 3.4. of this work. This pressure cell is made from the widely used CuBe alloy, which is diamagnetic at higher temperatures ( $> \sim 25$  K) and weakly paramagnetic at the low temperatures due to the small amount of impurities which are used for the precipitation hardening of the alloy. With the available sample space of few cubic millimeters and an intelligent design of the cell, the background signal in the DC measurement is usually negligible even in the case of weakly magnetic samples [26]. However, the CuBe is very good electric conductor and the eddy currents induced in the cell's body during the AC susceptibility measurement very effectively screen the signal of the sample. Considering the limitations of this pressure cell and taking the inspiration from the „historic“ techniques mentioned above, we decided to built a home-made detection coil set small enough to be placed inside the double layered clamped pressure cell (Chapter 3.4.2). The PPMS apparatus has been used to house the experiment. Besides the desired increase of the sensitivity of the measurement, this would also provide an extended range of accessible pressures up to  $\sim 3$  GPa.

The coil set consists of a pair of balanced detection coils with the opposite windings of wire and an excitation coil wound around them. A scheme of the assembly is shown in the Fig. 4.1. Detection coils are made of the  $50 \mu\text{m}$  copper wire and each of them contains roughly 100 – 300 loops. (The number is kept same for both coils, their size and hence the number of loops is adjusted to the size of available sample to get as high filling factor as possible). The use of a thinner wire was attempted to increase the number of turns and consequently the sensitivity, however, it turned out to be impossible not to break these thin wires as they need to be maintained tensioned during winding to control the shape and loop-count of the coils. The excitation coil consist of roughly 200 turns of  $80 - 120 \mu\text{m}$  copper wire wound around the detection coils. To utilize the careful balancing of the detection coils, the excitation coil is placed as symmetrically with respect to the center of the detection set as possible. The whole assembly is prepared on a piece of teflon tubing of appropriate size and is fixed with the GE Varnish, which is applied on top of each layer of wires during the preparation. Once the coil set is complete and the varnish is cured, the teflon tube is immersed in a liquid nitrogen to shrink ( $\sim 1$  min) and then

the coil set can be easily detached from it, leaving well finished „self - supporting“ structure. Resulting assembly is roughly 6 – 8 mm long with outer diameter of ~ 2 mm and inner diameter of ~ 1 mm. The newly prepared coil set is shown in the Fig. 4.2. The sample is placed inside one of the detection coils and fixed with small amount of the fast-acting cyanoacrylate glue (it is worth mentioning that GE varnish which keeps the coils together can be rather easily dissolved with the glues soluble in alcohol or acetone even after it has been properly dried, leading to its destruction). The whole assembly is then connected with the wires leading through the plug of the pressure cell. The magnanin manometer and Daphne 7373 pressure medium have been used as well as in all other experiments with this pressure cell use for this

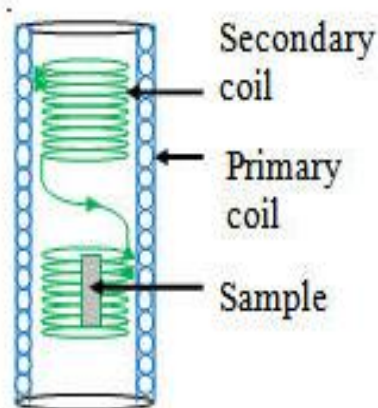


**Fig. 4.1:** Scheme of the detection coils.

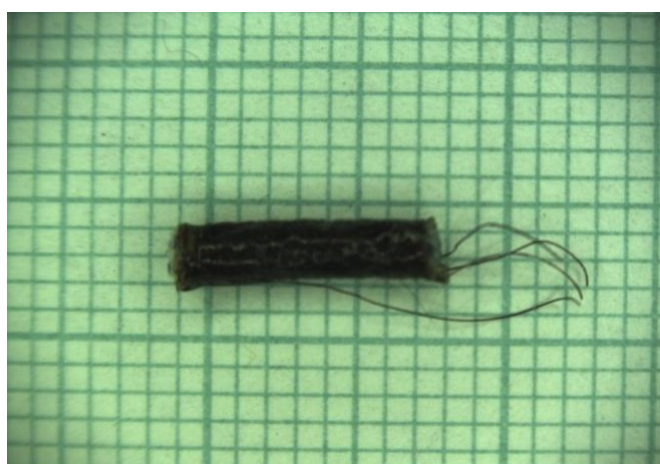


**Fig. 4.2:** Custom made detection coil set ready for the experiment.

In principle, the described setup could allow us to use either the AC Transport or ACMS options of the PPMS apparatus. Whereas the first one offers better control of the excitation signal (one can directly set the amplitude of electric current which is passing through the excitation coil, in the ACMS option the default coil set comes calibrated and the controlling software only allows to set the amplitude of already calibrated driving field), advantage of the latter one lies in the presence of preamplifier (20x gain) built-in directly on the connection wires. A loaded pressure cell is placed inside the apparatus instead of the default Quantum Design coil set which is normally used for the measurement at ambient pressure. The default detection set consist of two separate coils compared to our setup which is prepared using one wire and opposite winding in each coil. In order to get the correct

connection, our detection coil is connected with PPMS pins number 3 and 8 („+ and – poles“ of the respective default detection coils) and pins number 4 and 7 have to be short circuited. The driving coil is connected to the pins no. 11 and 12. The dewar is closed using the seal with the radiation shielding (used e.g. for resistivity measurements), however, the Multivu software which controls the PPMS requires the servo motor to be connected as usual in order to work properly, even despite the fact that it has no purpose in this experiment. Alternatively, if the external static magnetic field and lowest temperatures are not needed, experiment can be carried out using the close-cycle refrigerator instead of the PPMS. In this case use of the lock-in amplifier (Stanford Research, SR830) and pre-amplifier (Stanford Research, SR554) yields to comparable results.

The efficiency of the experimental arrangement can be nicely demonstrated on the measurements with the  $\text{ErCo}_2$  sample. One of the goals of this experiment was to observe the tiny anomaly in the AC susceptibility in the paramagnetic region ( $\text{ErCo}_2$  orders ferromagnetically with  $T_C \sim 33$  K) related to the proposed model of clustering of the cobalt moments [50-52], see Fig. 4.3 (taken from [53]). This anomaly is more pronounced in case of other members of the  $R\text{Co}_2$  family (e.g.  $\text{HoCo}_2$ ), however, in the case of  $\text{ErCo}_2$  it eluded the measurement with the piston-cylinder cell in the SQUID magnetometer. Fig. 4.4 shows the AC susceptibility data measured using the above described custom coils and Fig. 4.5 shows the detail of the curves around the temperature of the anomaly  $T_f \sim 95$  K before (left) and after (right) subtracting the Curie-Weiss susceptibility data for the Er moments from the original data. This fit clearly shows the pressure evolution of the anomaly and unambiguously verifies the high sensitivity of the developed experimental arrangement. Moreover, this relatively simple high pressure methodology of AC susceptibility measurements under high hydrostatic pressures allows to detect both, the pronounced as well as the very slight magnetic phenomena. Along with results of other measurements, the AC susceptibility experiment on the  $\text{ErCo}_2$  sample will be discussed in detail in the Chapter 4.2.

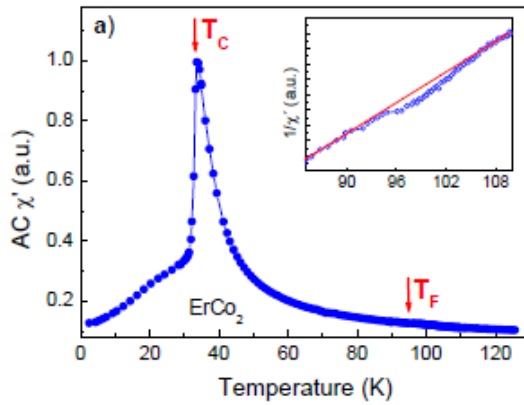


**Fig. 4.3:** AC susceptibility of  $\text{ErCo}_2$  at ambient pressure, data taken from [53]

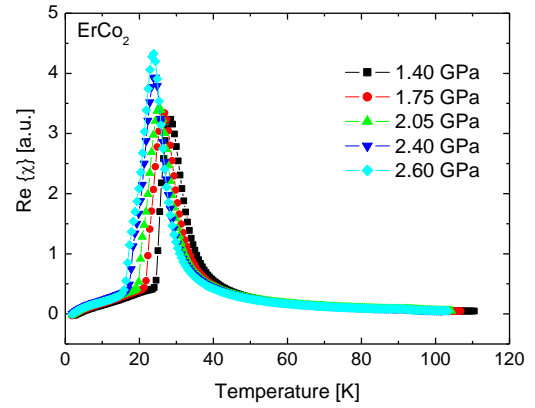


**Fig. 4.4:** AC susceptibility of  $\text{ErCo}_2$  under high pressures measured with the custom built detection coils.

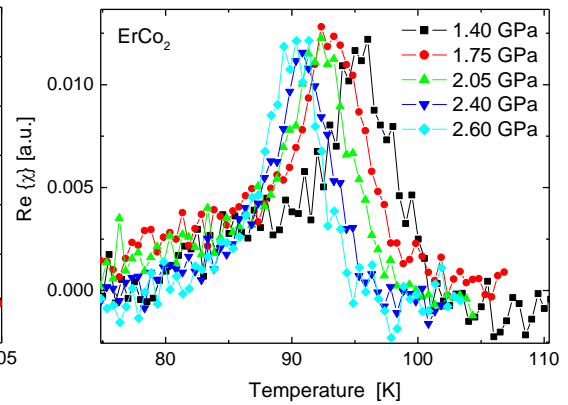
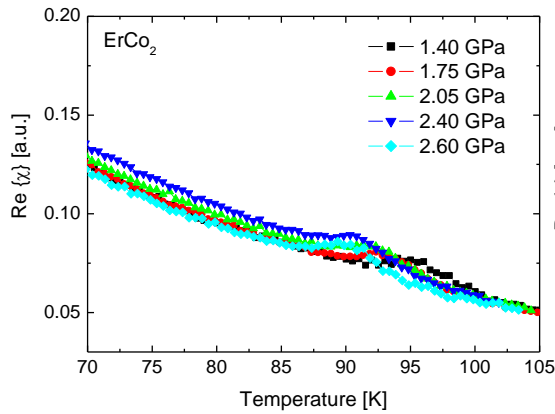


**Fig. 4.5:** Detail of the measured AC susceptibility of  $\text{ErCo}_2$  around the flipping temperature  $T_f$  (left), tiny peak-like anomaly at  $T_f$  after subtraction of the Curie-Weiss fit (right). The units on y-scales on Fig.4.4 and Fig. 4.5 are kept the same.

### 4.1.3 Heat capacity measurement in piston-cylinder pressure cells

Following text describes the implementation of the modulation calorimetry technique to measure the specific heat capacity under high pressures. Theoretical background of the method, necessary for further considerations of experimental setup, has been introduced in the Chapter 3.5. For practical reasons, we decided to use resistive heating and thermocouples to observe the temperature oscillations of the sample. Again, the double layered CuBe/NiCrAl piston-cylinder cell with the manganin manometer and a Daphne 7373 pressure medium was used to generate high pressures

and experiments were carried out using the Quantum Design's PPMS apparatus. During the preparation and first attempts of the experiment, numerous technical difficulties had to be overcome. They will be briefly mentioned where necessary, otherwise only the finalized experimental setup is described.

Resistive heating was realized by the commercially available strain gauges (Vishay precision group). The strain gauge consists of the small „grid“, roughly  $0.5 \times 1 \text{ mm}^2$  with resistivity  $\sim 120 \text{ } \Omega$  connected with leading wires of  $\sim 1 \text{ } \Omega$ , providing well localized heating. Besides having perfect shape for the calorimetry experiment the other intention was to measure simultaneously the thermo-elastic properties of the pressurized sample. For the purposes of the calorimetry, the sample must be much thinner than its characteristic thermal length, which is typically  $\sim 1 \text{ mm}$  for our samples and frequencies used in the experiments. On the other hand in the thermal expansion measurements, the strain gauge needs to be firmly attached to a „massive“ piece of sample. Despite all our effort, we have been unable to satisfy both conditions and we abandoned the thermal expansion measurement and focused solely on the heat capacity experiment. As the first test revealed, the thinner the sample is the higher quality data are obtained (in terms of much higher amplitude of observed oscillations and consequently less background noise). In further work, all samples have been brushed as thin as possible, typically down to a thickness  $\sim 40 - 50 \text{ } \mu\text{m}$ .

For several reasons the K-type thermocouple (chromel-alumel) has been chosen for measuring the temperature changes of the sample. First of all, as reported by only few existing publications dealing with effects of high pressure on the thermometric devices, the output of K-type thermocouple is almost unaffected by pressure, at least in considered pressure range  $0 - 3 \text{ GPa}$  [54]. Despite the fact that it is usually used in higher temperatures, with sensitive electronics it can be successfully used in all temperature range within PPMS ( $1.8 - 380 \text{ K}$ ) and it is unaffected by the magnetic field unless the Curie point of chromel ( $T_C \sim 620 \text{ K}$ ) is crossed.

It is available commercially in the form of very thin wires. This is not only of practical importance since the thermocouple needs to be as small as possible. In the first test we used ready thermocouple made with a  $25 \text{ } \mu\text{m}$  wires prepared by Anbetherm company [55], however the obtained results were not very satisfying. In the finalized version, bare wires have been used to create the two thermocouple

junctions in the differential connection. One joint is in direct contact with the sample and it's position is fixed with a small amount of glue. The point of differential connection is to have well defined reference point, therefore the second joint has been placed as far as possible from the sample assembly, it has been embedded in the stycast epoxy which is used to seal the wires in the plug of the pressure cell. This arrangement resulted in a much better sensitivity of measurement. Entire assembly has been mounted inside the CuBe/NiCrAl clamped pressure sell (Chapter 3.4). Prepared assembly installed on the plug of the pressure cell is showed in the Fig. 4.6.

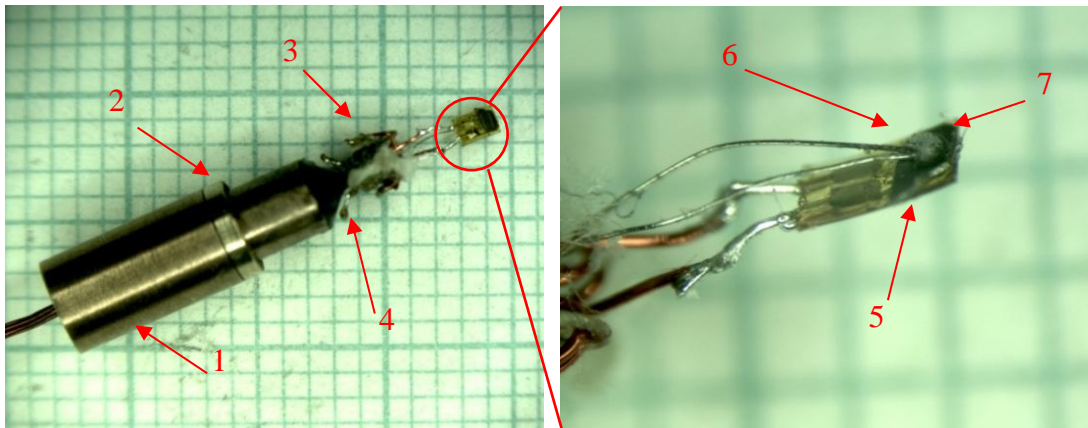


**Fig. 4.6:** Details of the sample assembly for the heat capacity measurements under high hydrostatic pressures : 1. Plug of the pressure cell, 2. sealing ring, 3. manganin manometer, 4. position of the reference thermocouple, 5. strain gauge used as heater, 6. thermocouple measuring the temperature oscillations of the sample, 7. Sample.

The modulation calorimetry technique in principle needs very small thermal excitations (see Chapter 3.5. for details) and consequently, the voltage induced on the thermocouple is very small as well. In our arrangement we have been looking for signals, typically, of order of few nanovolts. Moreover, when the current of frequency  $\omega$  is used for the heating, the generated temperature oscillations have frequency  $2\omega$ , so one technically needs to measure the 2<sup>nd</sup> harmonic component of the signal. Despite the comfort that PPMS apparatus offers to the user in controlling the experiment, above mentioned conditions are simply not easily suitable for standard electronics supplied by the Quantum Design with the machine. Therefore, the close-cycle refrigerator has been used to house the initial tests of the method with a lock-in amplifier (Stanford Research SR830) and pair of pre-amplifiers (Stanford

Research SR554), each giving 500x gain. Unfortunately, with such small signals the experimental setup is extremely sensitive to any mechanical manipulation of electrical wiring and as it turned out, it is sensitive to such an extent that close-cycle refrigerator cannot be used due to the vibrations induced by the helium compressor. These technical difficulties lead us to reconsider the situation and take rather drastic measures of cutting the PPMS connection wires and interfacing the machine with above mentioned external electronics, combining the benefits of both of them.

Given the nature of the experimental setup, none of the standard PPMS's measurement options could be used. For such a situation, recent versions of the MultiVu software have been upgraded with a additional option to control the experiment using the Visual Basic Scripting with a library of functions provided within the software. This option is accessible from the top menu bar (menu → sequence → advanced → edit macro). For some reason the standard PPMS manual does not contain any information about this option, however, an illustrative sequence file with all needed measurement commands is provided within the software. Additional information can be found on the Quantum Design's website [24].

Fig. 4.7 (left) shows inverse voltage as measured in the PPMS on the  $\text{ErCo}_2$  sample. This should be proportional to the specific heat of the sample (see section 3.5 for details), however, it does not take into account the temperature dependence of the output of the thermocouple (Fig. 4.7 (right), taken from [56]). Data corrected for this effect are shown in the Fig. 4.8 (left). Fig. 4.8 (right) displays the specific heat of  $\text{ErCo}_2$  sample at ambient pressure measured with the standard relaxation method for comparison. Further analysis and discussion of the data is presented in the section 4.2.2.

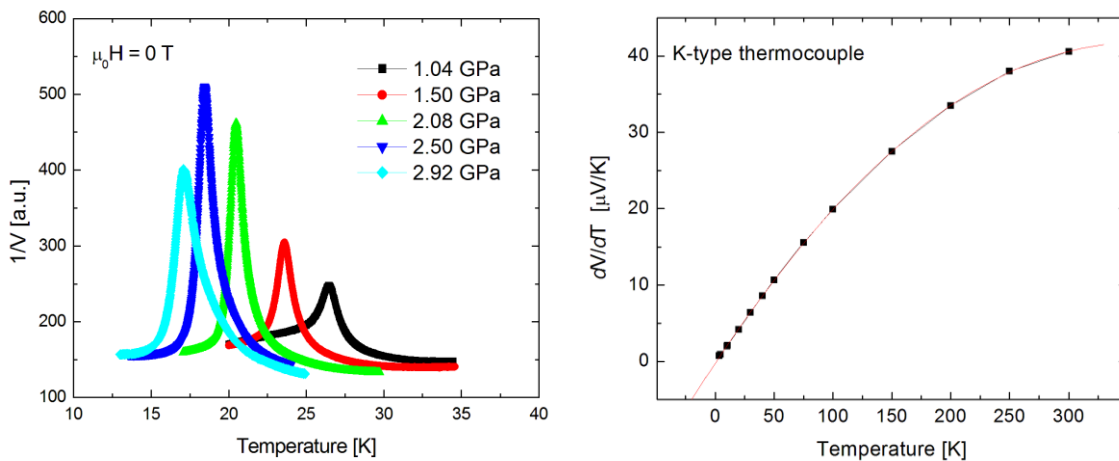


**Fig. 4.7:** Inverse voltage of the thermocouple measured on the  $\text{ErCo}_2$  sample under high pressures (left), temperature dependence of the output of the K-type thermocouple (right).

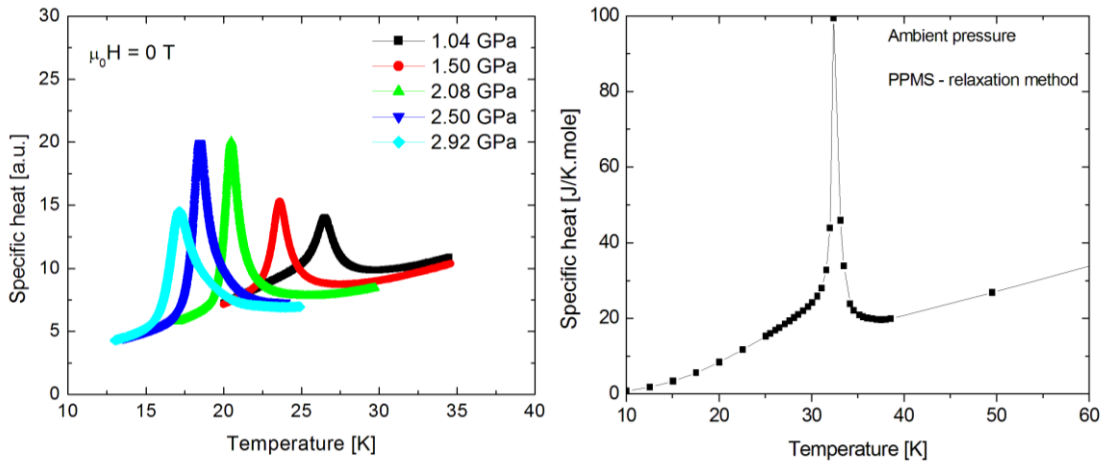


**Fig. 4.8:** Specific heat of the ErCo<sub>2</sub> under high pressures after corrections for the temperature dependence of the thermocouple output (left), specific heat of ErCo<sub>2</sub> at ambient pressure measured by standard relaxation method (right).

#### 4.1.4 Diamond anvil cell for magnetization measurement in SQUID magnetometer under very high pressures

##### Introduction

In the case of the piston-cylinder pressure cells for the SQUID magnetometer some minor adjustments and miniaturizations were required, but the design came more or less straightforward from the other cells of this type used in the past. However, with the diamond anvil cell being considered for this measurement, simple miniaturization is no longer possible. First of all, typical available sample space within the DAC is much smaller than in the case of piston-cylinder cells (typically  $\sim 10^{-4}$ -  $10^{-3}$  mm<sup>3</sup> vs 1-10 mm<sup>3</sup>) and consequently the parasitic signal caused by the cell is not negligible. The need to handle the background signal has to be considered prior to the cell design. The other major concern comes from the space limitations given by the sample chamber of the SQUID magnetometer – 9 mm in diameter. Together with limited choice of available nonmagnetic alloys, this seriously complicates the use of standard components for controlling the anvil alignment, which plays the crucial role in the successful loading of the pressure cell. The group of M. Mito [43] built a cell from CuBe with the usual anvil alignment control consisting of the xy-plane

adjustment of the lower anvil and a hemispherical cradle for tilt adjustment of the upper anvil. However, pressures only up to  $\sim 5$  GPa were reported so far, which is far below the potential of diamond anvil cells. Later on, the Easylab company produced a similar cell, claiming generation of pressures above 10 GPa. However, no published results using this cell can be found in available databases and information provided by the company only shows successful measurement of superconducting lead standard up to  $\sim 2.5$  GPa [2].

Recently, advances in the construction of the cell were reported by teams of G. G. Lonzarich and K. V. Kamenev [44, 45]. Both of them abandoned the usual anvil alignment techniques and adopted the procedure proposed by M. Erements [57], which relies on the extremely precise machining of both, diamond anvils and their supporting seats, with the possibility of fine alignment achieved by rotating the opposing anvil seats to a position where the mismatch in the tilt of the anvils is eliminated and maintain this position during the experiment. Apart from this fact, the design of these cells is completely different and represent the only two feasible options for effective handling of the background signal. Since our work was inspired by some aspects of both these designs in terms of both, construction details and a approach to eliminate the background, this will be further elaborated in the corresponding sections of the following text. Due to various problems we came across during the initial tests, the construction design had to be modified several times and few compromises slightly complicating the practicality of use had to be made. All relevant aspects of the design of the pressure cell will be discussed thoroughly.

### **General remarks on the construction of the cell**

In the magnetization measurement in the MPMS SQUID magnetometer, the sample is pulled through the set of superconducting coils separated by a distance of 4 cm and the change in flux passing through the detection coils is recorded. Under the assumption of a reasonably small sample, the resulting scan profile is then treated as originating from the point-like source with macroscopic dipole moment, example of the typical curve can be found in [26]. The data processing within the MPMS's software can be only successful when the collected SQUID response has this expected form, otherwise the fitting procedure fails and obtained value of

magnetization is nonsensical. While considering the shape of the pressure cell in general, there are the only two possibilities. First one is to miniaturize the cell to dimensions comparable with the usual sample size for ambient pressure measurements. The „Turnbuckle“ cell [45] has a dimension of 6 x 6 x 7 mm and approximate mass of 2 g, which very well meets above mentioned conditions. As a result of this approach, proper centering to the correct position is really easy since the pressure cell acts as an ordinary sample and obtained SQUID response has the expected form. Consequently, the fitting procedure works properly and the only thing one needs to do is to measure the same sequences for the empty cell and the cell loaded with the sample and then simply subtract the measured curves afterwards to get data corresponding to the sample. The price for this ease of use is that the background caused by the cell is rather high and measurement of weakly magnetic samples can be problematic.

Other way to deal with the background is having the cell as long and symmetric as possible. In the ideal case of an infinite homogeneous cylinder, the squid response would be identically equal to zero due to the symmetry reasons. In reality, the space limitations and the need of the functional parts of specific materials and shape prevents us from strictly keeping this symmetry. Despite the fact that the resulting SQUID response has no longer the expected shape, the amplitude of the background signal is much lower. Instead of direct subtraction of curves measured with and without the sample as in the previous case, the profiles of each measured point are subtracted and resulting scan is fitted in usual way. Recent versions of the MultiVu software has this procedure already implemented (Automatic Background Subtraction, [26]). The pressure cell designed by G.G. Lonzarich partially uses the concept mentioned above, however, in their case the suppression of the background was achieved mostly by using their own construction material of desired properties rather than perfected optimization of the cell's shape [45]. They prepared a high-purity Cu-Ti alloy solely for this purpose, which proved to be an excellent improvement, since the usually used commercial CuBe alloys contains some amount of additional elements (0.2% Pb, 0.5-1% Co), which are added to improve their mechanical properties. Nevertheless, as it will be shown later, with the correct optimization of the pressure cell's shape and using the Automated Background Subtraction procedure, the CuBe alloy can be used as well to obtain the results with the same precision.

Diamond anvil cell developed in the High pressure laboratory of IoP is shown in Fig. 4.9. Diamonds with 1.1 mm culetts (1.3 mm with beveled part) and approximate diameter 4 mm and height 2.3 mm from Almax Industries [58] has been used. All metallic parts were machined from nonmagnetic CuBe alloy supplied by the Berylco company [30]. The design of the cell follows the idea of a long symmetric body discussed above and it is made in the way to use all available space within the MPMS's sample chamber and still allow the full scan length during the measurement. The body of the cell is 100 mm long with 8.5 mm outer diameter and 5.5 mm inner diameter. The full length of the assembled cell is ~ 135 mm. Outer diameter of internal parts (diamond seats and springs) is 5.46 mm. These dimensions were chosen to allow certain freedom of movement (taking into account the change in diameter with loading) and yet provide best possible parallel arrangement of the culetts of the diamonds. The inner parts are hollow tubes to allow the visual control of the gasket with the sample area and the pressure determination by measurement of the fluorescence lines of ruby.

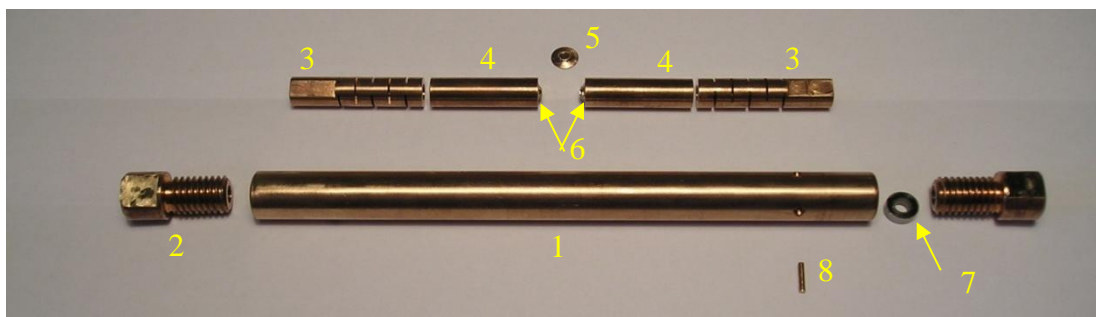


**Fig. 4.9:** Disassembled DAC for magnetization measurement, designed in the High pressure laboratory, IoP. 1. the body of the cell, 2. outer screws, 3. springs, 4. seats for diamond anvils, 5.gasket, 6. diamond anvils, 7. zirconia ceramic ring, 8. stick for fixation of the position of the spring.

Due to the 60 mm distance from the sample to the endings of the pressure cell, the openings must be as wide as possible for the optical access. On the other hand there are limitation for springs to have sufficient stiffness (proportional to their cross section) and for the area of the seats which needs to support the diamonds. The springs have the cylindrical hole with 3 mm diameter, the diamond seat has a conical

hole with 1 mm diameter on the diamond side and 3 mm diameter on the opposite end, matching the shape of the spring to prevent any abrupt changes in geometry that might result in the additional increase of the background signal. It is a known fact that the machining tools can leave the surface contaminated with iron and its oxides. The previously mentioned works [44, 45] used electropolishing to clean the newly prepared parts for the pressure cell. In our design, the precise guidance of the internal parts within the cell's body is essential to keep the alignment of the anvils. To satisfy both demands, we have produced the internal parts with dimensions slightly exceeding the target values and brushed them down to the desired diameter using the finest available sandpaper and diamond paste has been used for final polishing.

The construction of the cell assumes tightening of the outer screws as a way of applying the force on the anvils and set of springs to allow a larger sensitivity in the transfer of load from the tightened screw on the diamonds. Unfortunately, few difficulties emerged during the first experiments. First, the tube spring failed at the load of  $\sim 250$  kg (pressure inside the cell was  $\sim 6$  GPa), the

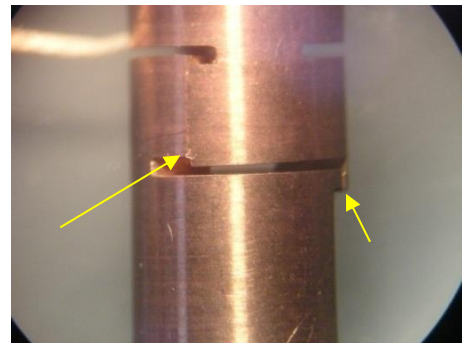


**Fig. 4.10:** Failure of the spring, arrows indicate the fractures.

fractured spring is shown in the Fig. 4.10. Since we don't have the capabilities for numerical modeling, the springs were originally designed using some approximative semi-empiric formulas based on the simple model situation of the long girder supported at the ends and a force applied horizontally on its middle section [42], (the slits cut into the cylinder creates a structure of „ribs“ that can be considered as a set of such girders stacked upon each other). As rough as this description seems at first sight, it worked surprisingly well in the case of the springs we prepared for other experiments in the past, however, those didn't have such demands for very high loads in very restricted space as in this case. Increasing the cross-section of the ribs as a way to achieve higher stiffness does not lead to intended result because the approximation the individual „ribs“ of the spring as a long girders here obviously fails. Since we could not find any better solution (neither ours nor reported by someone else) how to design the springs of such low diameter which would be able to mediate such high loads, the springs were replaced by the solid CuBe tubes in further experiments. In principle, there is no fundamental difference in the operation,

since the parts are only considered to be deformed elastically, however, the stiffness of the solid tube is much larger compared to the original tube spring. This makes the pressurizing little more delicate, since the angle of the screw adjustment required to produce given load is significantly smaller. In the case of solid tubes, the slight tightening of the screw ( $< 5^\circ$ ) typically leads to pressure increase 0.5 – 1 GPa. With the springs in the lower pressure region, the screw had to be turned roughly 30-40° to induce the same pressure increase. The option to use these springs was kept for situations, where fine pressure adjustment in low pressure region is desirable. For experiments requiring higher pressures, the solid tubes are used instead.

Another difficulty came from the fact that as the screw is adjusted, some of the internal parts have to rotate accordingly. First tests confirmed the logical guess that the lowest friction is between smooth surfaces of the diamond tips and the metallic gasket. This would not only lead to damaging the gasket and failure of pressurizing the cell but probably caused the breaking of the diamond anvils. To solve this problem, the flat surfaces have been milled on the outer part of the springs. Small holes in the outer part of the body of the cell were drilled and a position of the spring is being fixed by the small CuBe stick put inside the hole and matching the milled flat surface on the spring (see Fig. 4.9) As it turned out, the forces between the sticks and the springs are excessive and both parts are plastically deformed with attempts of loading of the cell. Therefore a ring of highly polished zirconia ceramics was added between the spring and the screw on one end of the cell. In addition, small amount of dry lubricant ( $\text{MoS}_2$ ) was used on the surfaces of the ceramic ring. Although not relieved completely, this precaution lowered significantly the stress the position-lock CuBe sticks are exposed to. After the pressurizing to  $\sim 15$  GPa in one of the tests there has been still some local damage and the durability of the springs and the fixation CuBe sticks will be limited, however, the cell could be smoothly assembled, pressurized and disassembled without any significant problems.

### **Assembling and loading of the cell**

First step in the experiment is to set the diamond anvils in the correct position on the seats and align them. Our solution is based on one of the works discussed above [45], where the diamond anvils and the gasket are completely free, only kept in the desired position during assembling by a small amount of low temperature grease. Once the

diamonds are seated and the gasket with the sample and pressure medium is placed on one of the anvils, the three pieces (cell's body + screws with seated diamonds) are then placed horizontally, carefully tightened up and the whole process can be observed under microscope by the small access windows in the body of the cell [45]. Contrary to this, more parts of the cell need to be moved and then fixed in the proper position in the case of our pressure cell and such a delicate manipulation would be near to impossible. The most viable approach is to assemble the cell in vertical position by gradually stacking prepared parts from bottom to top (see further text for details) and to be able to do that, the diamond anvils need to be attached to their seats in little more stable fashion. The hollow part of the seat is cut to a little smaller diameter so the diamond would not fit easily. Diamonds are gently pushed half-way inside the hollow part and manipulated into a roughly parallel alignment. Subsequently, the seats are put inside the cell, gently brought together to touch the diamonds and the parallelity is checked by observing the fringe patterns, created by wedge between touching culetts. If the tilt is too large, they need to be removed, repositioned and checked again. Once the optimal positioning is reached, a small metallic plate is placed between the diamonds and then squeezed together, pushing the diamonds on the flat bottom of the hollow part of the seats. The mismatch in diameters of the diamonds and the seats should not be too large to create an impassable obstacle, in which case the diamonds would rather indent the metallic plate than slip inside the seats. This would be probably accompanied with uncontrollable change in their alignment and possible damage. In our experience,  $\sim 20 \mu\text{m}$  mismatch on diameter is just enough to allow pushing them inside the seat smoothly, keeping them well positioned during mounting the cell and still be able to remove them

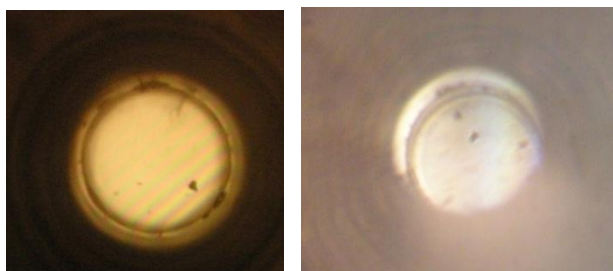


**Fig. 4.11:** Example of interference patterns corresponding to misaligned (left) and properly aligned (right) anvils.

easily after the experiment is finished. With this approach, the alignment will never be perfect, but reasonable working conditions can be achieved. Two photographs of fringe patterns comparing the bad alignment to the acceptable one is shown in Fig. 4.11. With 1-2 observed interference stripes the height of the air gap is of order  $\sim 1 \mu\text{m}$  across the 1.1 mm anvil culetts. The gasket is prepared from CuBe as well.

The 5 mm diameter disc is punched from the sheet of alloy of starting thickness 250  $\mu\text{m}$ . It is then indented with aligned diamonds inside the cell to a thickness 110 – 130  $\mu\text{m}$ . The sample hole, 200 – 250  $\mu\text{m}$  in diameter, is drilled in the gasket using the mechanical microdrill with a long focal length surgical telescope to assure the proper centering of the hole, example of indentation and drilling is shown in Fig. 4.12. Prepared gasket is attached on the anvil with the small amount of Apiezon low-temperature grease [59]. The sample and ruby chip are placed inside the sample area and a droplet of pressure medium (Daphne 7373) is placed in the end.

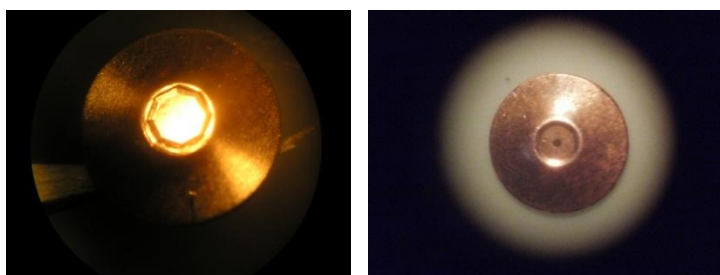


**Fig. 4.12:** Left: Indented gasket, Right: Properly centered hole drilled in the indented gasket.

The lower screw is tightened and a position lock of the lower spring is set in place. An auxiliary rod is then used to lift the lower spring vertically in the body of the cell to position, where prepared anvil seat with gasket and sample assembly can be safely transferred by tweezers. The spring together with the anvil seat is then returned to the bottom position onto already tightened lower screw. Next, the upper anvil needs to be placed inside the cell. Due to the minimal allowance between the internal parts and body of the cell and no other openings (if the diamonds are in place) the air inside can't be forced out fast and rather than falling down freely, the upper anvil slowly sinks inside the cell. Finally, the upper spring is inserted and locked in correct position, zirconia ring is placed on top of the spring and upper screw is gently tightened in hand. One cannot generate manually enough force through the screw to pressurize the cell. If the assembling was successful, only a small shift is experienced and further tightening by hand is impossible. Further manual tightening can only be possible when the gasket was misplaced during the mounting or the leak of the pressure medium occurred. In either case, one has to stop, open the cell and start again. Visual control of the sample space in the end will confirm the successful

assembling. Consequently, the cell is placed in the clamp and pressure is generated by adjusting the upper screw with the wrench.

### **1. test: Automatic Background Subtraction procedure and the quality of the signal**

First thing that needed to be tested is the quality of the signal and the way of handling the background caused by the pressure cell. The automatic background procedure (ABS), implemented within the MPMS's MultiVu software, works in the following way. Each measured point ( $M = M(T,B)$ ) is measured with the empty pressure cell and later with the sample. The obtained scan profiles are subtracted and the resulting profile is fitted in the usual way. The software offers two options. The data from the measurement with sample can be matched point by point ( $B,T$ ) with the data from background file or interpolated. How the interpolating of the profile scans actually work is not clear and in our experience very often does not lead to reasonable results. Therefore, one has to carefully consider the measurement sequence for the investigated sample prior to the experiment, run the identical sequences with and without the sample and use the point by point option for correct matching of background and sample data.

For the experiment, the cell (or any other „sample holder“ of interest) has to be in exactly the same centered position during background recording as in the measurement with the sample. To do that, the surrogate (strongly magnetic) sample is used to find the correct centering and this position of the motor has to be kept during the following experiment. Then the surrogate sample is removed, cell is reassembled in the completely same shape and the background is recorded. After that, the cell is opened, the gasket, sample, ruby and the pressure medium are placed inside and the cell is sealed, again with the same shape (the screws allow some freedom in positioning of the internal setup with respect to the body of the cell, it has to be assembled the same way in both runs in order to procedure to be successful). Next, the experiment with the loaded cell with the sample is executed. The procedure directly asks for the file containing the background data and the results already corrected for the background signal are displayed. The raw data file (.raw, option for

recording the profile scans compared to a standard datafile, where only the fitted magnetization values are present) in this case contain profiles of both, background and sample measurement together with corrected scans corresponding only to the sample and its fit, allowing further inspection of results.

In presented work, a small piece of  $\text{Fe}_{36}\text{Ni}_{64}$  invar alloy has been chosen for the first test as both, the surrogate sample for centering the position and a sample for testing the quality of obtained data. It is a ferromagnet with  $T_C = 508$  K [60]. The position of the pressure cell has been centered at room temperature, the differences caused by shrinking of the sample rod with temperature are successfully handled by the software (autotracking option within the MultiVu software [26]). The results demonstrating the capabilities of the procedure are shown in the Fig. 4.13.

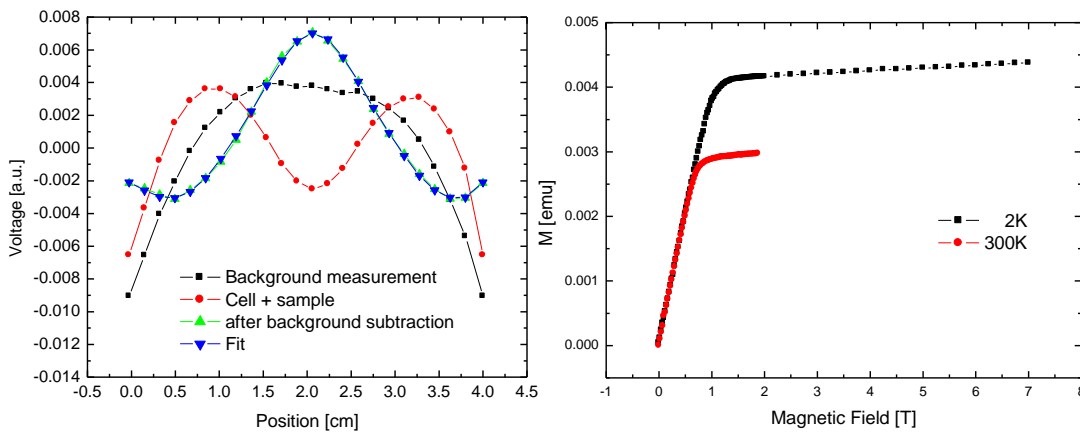


**Fig. 4.13:** SQUID-response corresponding to empty cell, cell with the sample, their difference and it's fit (left), DC magnetization of  $\text{Fe}_{36}\text{Ni}_{64}$  sample within the DAC pressure cell obtained using the ABS procedure (right).

## 2. test: Superconducting transition of Pb

Lead is a commonly used pressure sensor owing to facts, that the shift of the superconducting transition with pressure is well documented for a long time [31], the change in magnetization with entering the superconducting state is large and usually well observable effect and the transition is very sharp, allowing precise pressure determination even with relatively small pressure induced shift  $dT_C/dp \sim -0.4$  K/GPa [31]. The results of measurements of the superconducting transition of Pb under pressure are presented in Fig. 4.14. It would be convenient to compare the pressure

determined by lead at low temperatures to the pressure determined at room temperatures by ruby and this experiment will be done in future, however, at the time of this test we did not have the option to measure the ruby fluorescence lines, so only the low temperature Pb data are shown. The experimental setup for this measurement used the tube springs originally proposed in the cell design, where the failure of the spring, described in previous section of the text, occurred at a pressure of  $\sim 6$  GPa. Further tests were executed with the modified design and the results showing the achievement of higher pressures are presented in the following paragraph.

Apart from the fact that this test confirmed successful construction of the cell, the loading procedure and data acquisition, one more important conclusion can be made. The data, showing the usual shape of the transition, are of order  $10^{-6}$  emu, which is bordering the resolution of the MPMS apparatus itself,  $10^{-7}$  emu as claimed by its manufacturer [25]. Given the extremely small samples that can be used in the experiment and presence of the massive body of the pressure cell, this is the sensitivity beyond expectations.

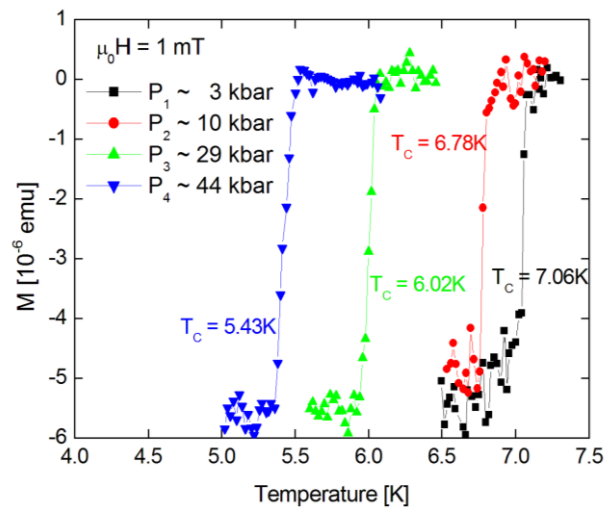


**Fig. 4.14:** DC magnetization measurement of the superconducting transition of the lead sample under high pressures.

### 3. test: Different pressure media

Pressure media used in the experiment can have significant effect on the shape of the measured curves since there is tendency to loose ideal hydrostatic conditions above certain pressure in all possible substances. In principle all, gases, liquids and soft solids can be used to mediate the pressure in the sample area. Whereas easy handling is the main advantage of solids (most commonly used is steatite), they offer the worst conditions in terms of hydrostaticity. On the other hand, gases can provide excellent hydrostatic conditions but their handling can be delicate since the energy stored in compressed gas is enormous ( $\Delta E \sim p\Delta V$ ). In addition, diamond anvil cells do not

provide enough space to accommodate for such a volume change and gaseous media are mainly used only in piston-cylinder cells [42]. Nevertheless, some works reported using the gases in DAC's with the gas being loaded under pressure of several kbar in another larger pressure apparatus enclosing the diamond cell [45]. The compromise in simple handling and hydrostaticity can be presented by liquid media, which are frequently used in both, piston-cylinder and diamond anvil cells. In the most commonly used liquids, Fluorinert fc-70 and Daphne 7373, the solidification through the glass transition occurs at the pressures  $\sim 1.2$  GPa [61] and  $\sim 2.5$  GPa [62], respectively. Above this pressure, the conditions are no longer hydrostatic and to our best knowledge, the pressure gradient across the sample space can be as large as 10 – 15 % of the nominal value. Significant improvement of conditions inside the DAC's came with the loading of liquefied gases. Cryogenic liquids are now widely used and they can provide good hydrostatic conditions to very high pressure, in case of helium up to the pressures  $\sim 30$  GPa [29].

With our diamond anvil cell, the fact that neither the anvils nor the gasket is permanently fixed in required position, represents a serious technical difficulty for loading of the cryogenic liquids. The use of Daphne oil as a pressure medium in the first test showed typical broadening of the phase transitions due to the pressure gradient in the sample chamber and alternative options for a pressure medium has been searched. We tried to use the methanol-ethanol-water mixtures, which has been frequently used in the past before the widespread use of the cryogenic liquids. For some compositions, the hydrostatic pressures were reported even above 10 GPa. The mixture with composition 16:3:1 for which the highest hydrostatic pressure ( $\sim 16$  GPa) has been reported [29], was used in our experiment. Compared to experiments with Daphne oil, assembling the cell was little more difficult, since the alcohols evaporates rapidly, moving and sometimes flushing away the sample and the mixture does not soak inside the sample space so easily as the oil and have tendency to form air bubbles. However, with some patience, the cell can be sealed and pressurized the same way as described earlier. Fig. 4.15 shows the ruby fluorescence spectra measured under pressures up to 15 GPa, clearly demonstrating significant improvement with the methanol - ethanol - water mixture over the Daphne oil. Despite the fact, that perfect hydrostatic conditions were not observed up to the pressures claiming by [29], excellent conditions were demonstrated roughly up

to 9 GPa compared to 2.5 GPa in the case of Daphne oil, where the onset of broadening of the fluorescence peaks is already witnessed.

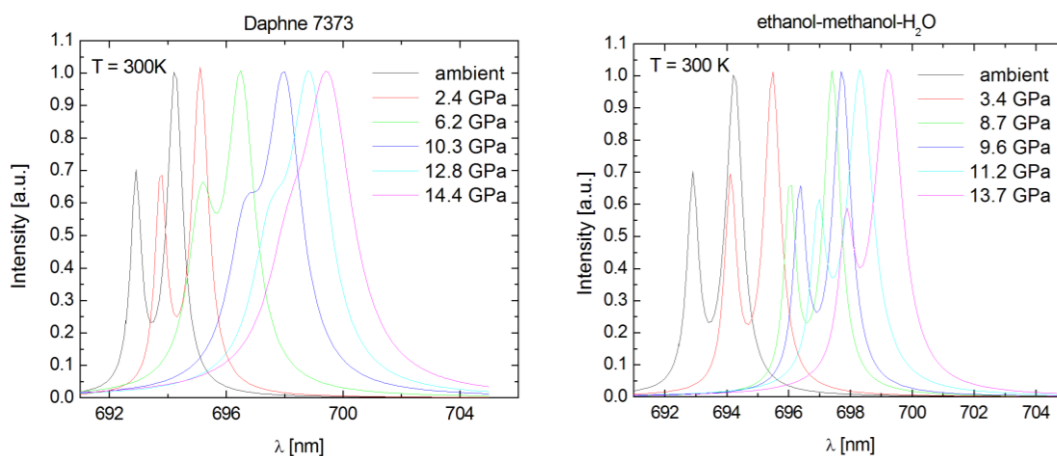


**Fig. 4.15:** Ruby fluorescence spectra measured with two different pressure media under pressures up to 15 GPa.

#### 4.1.5 Uniaxial pressure cells

##### Introduction

While studying the influence of high hydrostatic pressures has been rapidly growing in popularity across most fields of material research over the last decades, there still exist only few hundred published papers concerning the material properties under elastic uniaxial stress, most of them published in last few years. Experiments on single crystals subjected to uniaxial compression along the different crystallographic directions is particularly interesting option for the materials with pronounced anisotropy of physical properties. Recently, huge influence of the uniaxial compression, qualitatively very different from the hydrostatic pressures, have been reported in various condensed matter systems [63 - 65].

This section presents two new uniaxial pressure cells (magnetization measurements in the SQUID magnetometer and neutron diffraction experiments), recently designed in the IoP and the modification of hydrostatic pressure cell 3.4.2 for resistivity measurements under uniaxial stress. Comprehensive overview of the

results obtained by all these measurements on the UNiGa single crystal is presented in the section 4.3.

### Sample preparation

While the design and operation of the uniaxial cells is relatively simple, precise sample preparation plays the crucial role in the success of the experiment. Nature of the experiment does not allow the homogeneous stress distribution, as the sample has finite dimensions. There are several requirements for the sample shape that have to

be respected in order to assure the loading to be successful and pressure inhomogeneities minimized. First of all, sample bases have to be perfectly parallel and highly polished to prevent any excessive pressure built-up on some point of the sample, which would lead to its destruction with the attempts of loading. Sides of the sample have to be perpendicular to the bases so they both have same area. Ideally, sample bases should have circular shape,

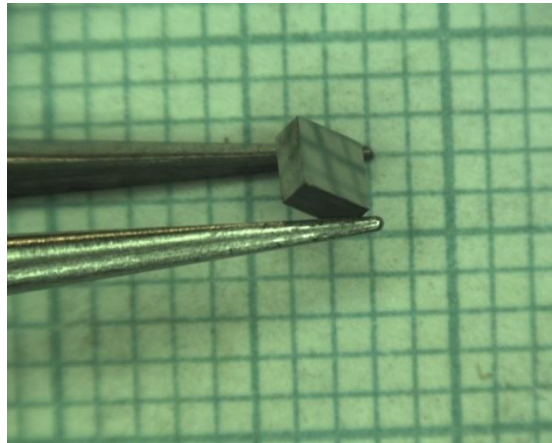


**Fig. 4.16:** UNiGa sample, properly shaped and polished for the uniaxial pressure experiments.

however, preparing the sides perpendicular (i.e. sample in the cylindrical shape) can be very difficult. For practical reasons, it is best to prepare the sample in the cuboid shape and still satisfy both above-mentioned conditions. Thickness of the sample should be lower than the length of the edges of the bases. In addition to the easier control of the parallelity of the sample bases during preparation, the main reason for this is better „confinement“ of the slipping planes (whatever is their angle in the given structure) by the supported bases and subsequently avoiding the plastic deformation of the crystal. The main disadvantage of this shape is rather large demagnetizing factor, that has to be considered during data processing. As mentioned in the beginning, inhomogeneity of the stress distribution can't be avoided and it gives rise to another technical difficulty. If we observe some quantity depending on the applied load, all the effects that one might be looking for in the experiment, are

„smeared“ as all parts of sample under different compression contribute to the signal. Despite these problems, it can be clearly seen if there is any systematic change by comparing the data taken at different pressures. Sample is prepared in desired shape in the following way: First it is oriented on the goniometer using the Laue diffraction patterns. The first of the bases is either cut with the fine wire saw or brushed on the polishing machine with a sand paper (when the shape of the crystal does not allow precise cutting, e.g. when the direction of intended pressurization does not coincide with the axis of the crystal pulled from the melt) with the crystal still being placed on the goniometer. Next, the other base is cut (or brushed down) in parallel and both surfaces are polished with a diamond paste. Last, the perpendicular sides are cut in the rectangular shape for easy determination of the area and later the pressure of the loaded sample. Example of well shaped and polished sample is given in the Fig. 4.16.

### **Uniaxial cell for the magnetization measurements**

The uniaxial pressure cell for magnetization measurements in the SQUID magnetometer is shown in Fig. 4.17. The construction is based on the hydrostatic pressure cell, which has been introduced in section 3.3. The CuBe body has the outer diameter of 8.5 mm and has essentially same shape on outside as the hydrostatic cell. Internal part was modified with a setup for applying the force directly on the sample instead of compressing the pressure medium to create the hydrostatic conditions. Since the loads that need to be supported by the body of the cell and the screws are in this case much lower, the internal diameter of the cell was widened from 2.5 mm to 4.5 mm to provide more space for accommodating larger samples. Sample is placed between a pair of highly polished parallel zirconia blocks within a CuBe guiding tube. The CuBe „tube“ springs are used to mediate the force applied by tightening of the screws. Springs are calibrated outside the pressure cell on a hydraulic press. Pressure of sample is then determined from known area of the sample surfaces and a shortening of a calibrated spring given by the shift of the tightened screw. This way the load is applied along the axis of the cylindrical body of the cell. Alternative internal setup with a 45° prisms instead of flat blocks has been made to apply the stress perpendicular to the cell axis (Fig. 4.18). Under the reasonable assumption of minimal friction between metallic and polished zirconia parts, the pressure on the

sample is determined in the same way as in the case of the flat ceramic parts in the axial arrangement with only difference of dividing the applied force by the cosine of the angle of the prisms:  $1/\sqrt{2}$ .



**Fig. 4.17:** Uniaxial pressure cell for the magnetization measurements in the SQUID magnetometer.

#### **Uniaxial cell for the neutron diffraction experiments**

The uniaxial pressure cell for the neutron diffraction experiments has basically the same design as the the one for the magnetization measurements, including the options for either axial or perpendicular orientation of stress applied to the sample with respect to the axis of the cell. Only considerable difference is in the use of the material for the metallic parts. Instead of the CuBe, this cell is made of  $\text{TiAlV}_6$  compound. This material does not have sufficient strength for supporting the loads required in the hydrostatic cells, however, its mechanical properties are satisfying for much lower loads needed in the uniaxial cells. Serious advantage is significantly smaller neutron absorption. This allows considerable reduction for the time needed to collect reasonable statistic ansamble of data. The cell is shown in Fig. 4.18.

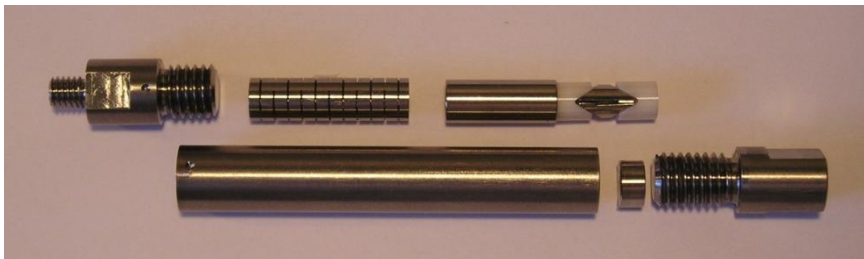


**Fig. 4.18:** Disassembled  $\text{TiAlV}_6$  uniaxial cell for the neutron diffraction experiments, showing the internal setup for pressure applied perpendicular to the axis of the cell.

### Resistivity measurements under uniaxial pressure

To avoid the construction of another pressure cell for the transport measurements, the insert for the hydrostatic pressure cell for the PPMS apparatus (introduced in 3.4.2) has been modified to house this experiment. Sample is again placed between the discs of zirconia ceramics, tube spring is used directly instead of the piston. Fig. 4.19 shows the sample contacted for the standard four-probe resistivity measurement.



**Fig. 4.19:** Sample assembly for the resistivity measurement under uniaxial pressure.

#### 4.1.6 Conclusions

We implemented the methods for sensitive measurements of the magnetic AC susceptibility and specific heat under high hydrostatic pressures up to 3 GPa in the wide range of temperatures (1.8 – 380 K) and magnetic fields (up to 14 T) using the double layered CuBe/NiCrAl piston-cylinder pressure cell within the PPMS apparatus. Series of uniaxial pressure cells for measuring DC magnetization, AC susceptibility, electrical resistivity and neutron diffraction experiments has been built and successfully tested. Two types of interchangeable internal setups allow to apply the pressure along the axis of the cell and perpendicular to it, respectively. This allows a versatile combination of the directions of applied stress and magnetic field (and/or the diffraction plane).

Diamond anvil pressure cell for precise magnetization measurements under very high pressures in the commercial SQUID magnetometer has been built. Despite several construction compromises to usual design and the miniature available sample space, excellent efficiency of both, the sensitivity of measurement and capability to achieve very high pressures has been demonstrated. To our best knowledge, only one other laboratory in the world [44] owns such a pressure cell.

#### 4.1.7 Plans for future development in JLMS

Given the current interest in various phenomena that are usually restricted to very high pressures and very low temperatures, the most urging need is for construction of the diamond anvil cell for the new He<sup>3</sup>/He<sup>4</sup> dilution refrigerator. Considering the available space (35 mm diameter) the cell will use the „classical“ design incorporating the diamond alignment components, which should allow us to achieve considerably higher pressures compared to the cell designed for the magnetization measurement in the SQUID magnetometer (see section 4.1.4). Easiest experiment to do will be the electrical resistivity measurement, the DAC's are used for this purpose routinely. The machine for spot-welding of the contacts (25 μm golden wires) on small samples was recently built and successfully tested in the JLMS. With the small adjustments of the sample assembly, we assume the use of the methods described in the 4.1.2 and 4.1.3 for measuring the AC susceptibility and specific heat of the sample in this conditions as well. Such an experiments are already reported in the literature [66 and 39, respectively] and one successful AC susceptibility experiment with a similar DAC was prepared by the author during his study stay in the Centre for Science at Extreme Conditions, The University of Edinburgh (CSEC) in October 2010. With the detection coil fitted inside the gasket of the DAC, one can start considering other experimental options, that could made significant contribution to this research area. Namely, successful experiments of nuclear magnetic resonance [67] and the de Haas-van Alphen effect [68] under high pressures have been reported recently and accommodating them in the JLMS is highly desired as well.

## 4.2 Magnetism in $R(\text{Co}_{1-x}\text{Si}_x)_2$ compounds under hydrostatic pressure

### 4.2.1 Introduction

$\text{ErCo}_2$  and  $\text{HoCo}_2$  belongs to the large group of  $RT_2$  ( $R$  – rare earth element,  $T$  – transition metal element) compounds crystallizing in the cubic Laves phase structure ( $\text{MgCu}_2$  – type, space group  $\text{Fd-}3\text{m}$ ). The  $R\text{Co}_2$  compounds represent a particularly interesting part of this group due to the magnetic instabilities in the Co sublattice.

The exceptionality can be illustrated by the comparison with the  $R\text{Fe}_2$  and  $R\text{Ni}_2$  compounds. In the  $R\text{Fe}_2$  compounds, the Fe – sublattice satisfies the Stoner criterion [69], so the Fe moments exist practically irrespective whether the rare earth ions bear the magnetic moment or not. On the other hand, in the  $R\text{Ni}_2$  compounds, the Ni sublattice bears no (or negligible) magnetic moment even in the compounds with the magnetic rare-earth ions [69, 70]. Contrary, the magnetic moments on the Co sites in the heavy ( $R$  beyond Tb)  $R\text{Co}_2$  series strongly depend on the existence of the moment on the rare-earth sites. Since the Co 3d – band states appear near the critical conditions for the magnetic moment formation, the  $R\text{Co}_2$  compounds offer a great opportunity to study various aspects of itinerant electron magnetism.

The  $R\text{Co}_2$  compounds with nonmagnetic  $R$  (Y, Lu) are strongly exchange-enhanced Pauli paramagnets that undergo a metamagnetic transition at low temperatures by applying the magnetic field larger than  $\sim 70$  T [71, 72]. When the  $R$  elements are magnetic, the Co metamagnetic state can be achieved in zero external fields due to the large internal exchange fields created by the ferromagnetically ordered 4f moments at the transition temperature  $T_C$ . In the compounds containing the light rare earth ions the  $R$  and Co magnetic moments are parallel, while in the compounds with the heavy rare-earths the Co moments order antiparallel to the  $R$  moments. In case of  $R = \text{Dy}, \text{Ho}, \text{Er}$ , the first-order magnetic phase transition is observed at  $T_C$ .

At ambient pressure, the  $\text{ErCo}_2$  compound orders ferrimagnetically at  $T_C = 33$  K [71] with the Er moments  $\mu_{\text{Er}} = 8.84 \mu_B$  aligned along the [111] direction of the crystal structure and induced moments on the cobalt sites,  $\mu_{\text{Co}} = 0.95 \mu_B$ , aligned antiparallel to the erbium ones [72]. Pronounced first order magnetic phase

transition (FOMPT) is reflected in the shape of the various bulk properties and a temperature hysteresis effects. The magnetic ordering is accompanied with the rhombohedral distortion of the cubic lattice. Previous high pressure works observed gradual decrease of the ordering temperature  $T_C$  with the tendency to saturation at pressure  $\sim 4$  GPa with no further development at higher pressures and concluded the suppression of the induced magnetic moment in the Co sublattice [73, 74].

The changes in the 3d band structure within the series controlled by the variation of the lattice parameter (due to the lanthanide contraction) have been found to be the reason for the first-order transition [75, 76] and should change to the second-order transition either by diluting the magnetic  $R$  atom (i.e. by nonmagnetic Y, [72]) or by applying the pressure [77]. Furthermore, recent theoretical work [78] suggested that the ordering of the Er and Co sublattices should separate under high pressures in similar way as observed in the samples substituted by the yttrium for the erbium atoms.

In the case of the  $\text{HoCo}_2$  compound, the ferrimagnetic ordering through the FOMPT happens at  $T_C = 79$  K [79]. In addition, one more magnetic phase transitions at  $T_R = 16.5$  K is observed, where the easy magnetization axis changes from the [100] to [110] direction [80]. Generally, similar behavior with the applied pressures as in the case of the  $\text{ErCo}_2$ , i.e. the decrease of the ordering temperature and eventual suppression of the Co magnetism has been concluded by the authors of the previously published works as well [81].

Interesting turn of events in the picture of physics of the  $\text{RCo}_2$  compounds occurred when Herrero-Albillos et al. [50 - 52] started investigating the magnetic properties of  $\text{ErCo}_2$  by means of the microscopic methods. X-ray magnetic circular dichroism (XMCD) clearly demonstrated the existence of a net magnetic moment in the cobalt sublattice well above the ferrimagnetic ordering temperature  $T_C = 33$  K. Moreover, it has been observed that at  $T_f = 100$  K (further called flipping temperature) the Co spins change their orientation with respect to the erbium moments and this phenomenon has been named parimagnetism. By analysis of the balance of the Er-Co and Co-Co interactions and the influence of the external magnetic field, they concluded that the flipping of the Co spins have to be realized in a collective fashion rather than by flipping of the individual spins. This idea was corroborated by the experiments of small angle neutron scattering, which concluded a presence of the short-range ordering of the Co moments in the paramagnetic regime

of  $\text{ErCo}_2$  with a characteristic length  $\sim 7 - 8 \text{ \AA}$  [52], corresponding to  $\sim 60 - 100$  Co atoms participating in the ordered clusters. A virtually spurious bump at the flipping temperature  $T_f$  in the AC susceptibility data has been identified with the findings obtained from the XMCD and SANS measurements [50].

Given the above-mentioned facts, most of the efforts in this work have been devoted to investigating the properties of the parent  $\text{ErCo}_2$  compound and will be handled separately in the first of the following paragraphs. However, Herrero-Albillos et al. in their original work suggested [50], and only lately proved that the same effect is present in the compounds based on other rare-earth atoms, Dy, Ho and Tb, as well [82]. Recently, we started investigating the Dy- and Ho- based compounds and the partial results of the ongoing work will be presented in the following paragraphs.

Due to the remarkable effect of even slight substitutions of p-elements into the cobalt sublattice on the magnetic properties of  $R\text{Co}_2$  compounds, known from the previous works [83 and references therein], we decided to prepare a comparative study of samples containing 2.5% Si for every studied “pure” compound. The results obtained on the substituted samples are presented and discussed within the frame of their parent compounds in their respective sections.

## 4.2.2 Results and Discussion

### 4.2.2.1 $\text{ErCo}_2$ and $\text{Er}(\text{Co}_{0.975}\text{Si}_{0.025})_2$

#### **$\text{ErCo}_2$ – magnetization behavior under pressure**

To investigate the development of the Co magnetic moments, the DC magnetization measurements were performed under pressures up to  $\sim 1$  GPa using the hydrostatic cell, described in 3.4.1 and a SQUID magnetometer.

The temperature dependence of magnetization has been measured in the temperature range  $2 - 60$  K in the applied magnetic field  $\mu_0 H = 0.1$  T. The results, displayed in the Fig. 4.2 a), show a linear decrease of the ordering temperature with applied pressure at a rate  $dT_C/dp \sim -6.85$  K/GPa. The magnetization curves, taken at the temperature  $T = 2$  K, are shown in the Fig. 4.20 b). A linear increase of the

saturated magnetization in the high fields has been observed. Due to the localized nature of the 4f-states of the rare-earths, it is reasonable to assume that pressure induced variation of the atomic distances is insufficient to have any considerable effect on the Er moments in this pressure range. Consequently, the observed change of the magnetization of ErCo<sub>2</sub> can be attributed solely to the change of the Co moment with the applied pressure. Given the antiparallel alignment of Er and Co moment, the increase of the saturated magnetization of ErCo<sub>2</sub> with pressure means that the value of the Co moment decreases. Observed data allow the conclusion of the pressure induced change  $d\mu_{\text{Co}}/dp \sim -0.126 \mu_{\text{B}}/\text{GPa}$ .

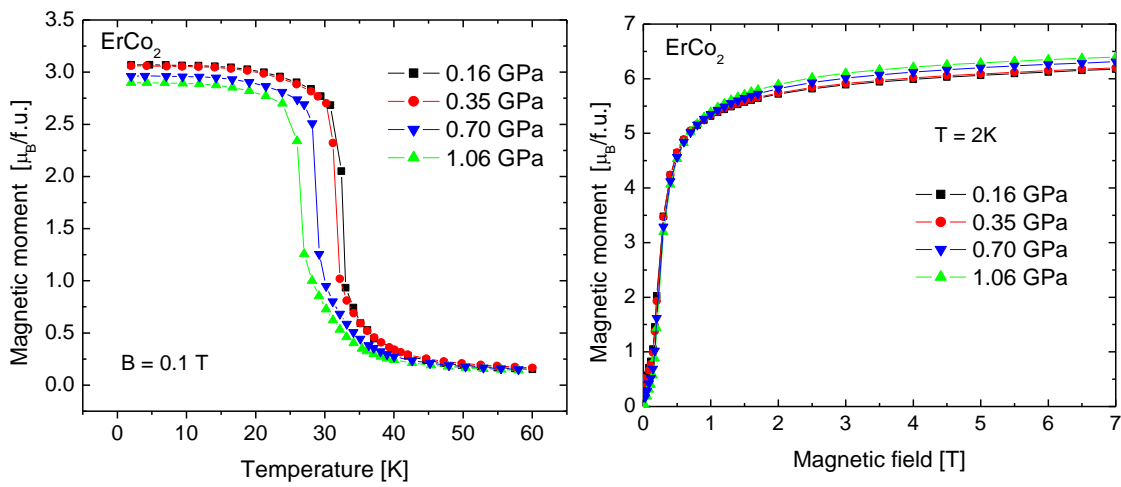


**Fig. 4.20** a) Field cooled temperature dependence of magnetization of ErCo<sub>2</sub> under pressure, b) virgin magnetization curves of ErCo<sub>2</sub> measured at  $T = 2 \text{ K}$ .

### ErCo<sub>2</sub> - Electrical resistivity and specific heat under pressure

To investigate the properties of ErCo<sub>2</sub> in pressures exceeding the 1.2 GPa range of the hydrostatic SQUID cell, the measurements of electrical resistivity and specific heat under pressures up to 3 GPa were performed using the double layered CuBe/NiCrAl piston-cylinder cell within the PPMS apparatus (see section 3.4.2 for details). Resistivity measurements used the standard four probe method (section 3.2.3) on a bar-shaped piece of polycrystalline sample of approximate dimensions  $1 \times 1 \times 5 \text{ mm}$ , AC calorimetry technique and the setup for the

measurement of the specific heat was introduced and discussed in detail in sections 3.5 and 4.1.3, respectively. Results of these experiments are shown in Fig. 4.21 a) and Fig. 4.21 b), respectively.

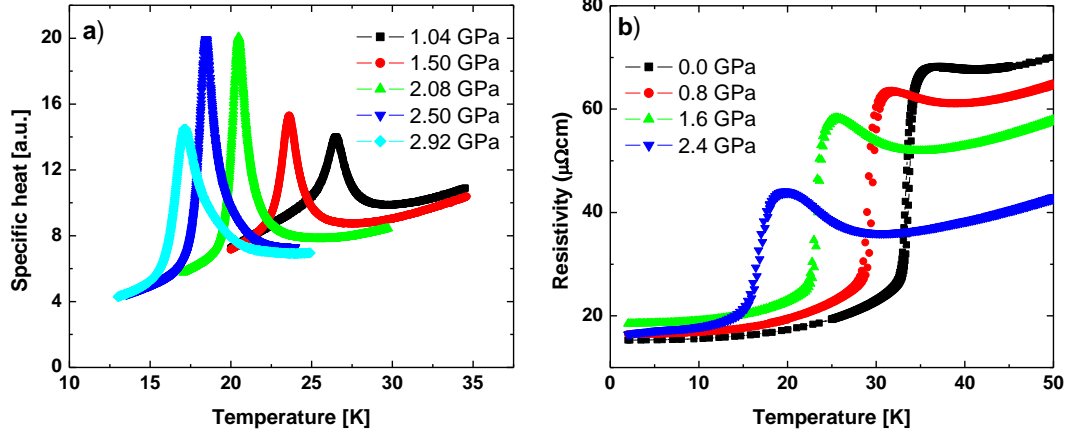


**Fig. 4.21** a) Specific heat of ErCo<sub>2</sub> under high pressures, b) Electrical resistivity of ErCo<sub>2</sub> under high pressures.

Both sets of measurements have shown the decrease of Curie temperature  $dT_C/dp \sim -6.85$  K/GPa up to the pressure  $\sim 2.5$  GPa well agreeable with the previously reported studies [74, 84] and consistent with our magnetization measurements (Fig. 4.20).

Apart from the pressure induced shift of the transition temperature  $T_C$ , the resistivity data have shown qualitative change with the applied pressures. At ambient pressure, the pronounced first-order transition has been approved by the huge step-like transition at the  $T_C$ , arising from the formation of cobalt 3d-moment and by observed temperature hysteresis. A characteristic feature is the shape of the measured curves, which exhibit increase of the resistivity in the vicinity of  $T_C$  when approached from higher temperatures. Previous works attributed this feature to the critical conduction-electron scattering on the spin fluctuations in the  $d$ -band [85]. As the pressure is increased, the size of the resistivity drop at  $T_C$  is gradually reduced and the anomalous upturn above the  $T_C$  becomes more pronounced. Closer inspection of the resistivity data also revealed the gradual suppression of the hysteresis of the transition at  $T_C$  from the value  $\Delta T_C \sim 0.5$  K at ambient pressure to the  $\Delta T_C \sim 0.12$  K at the pressure  $p = 2.4$  GPa. All these facts confirm the change of the order of the transition from 1<sup>st</sup> to 2<sup>nd</sup> order under applied pressure, which has been proposed in

literature [77, 78]. By extrapolating the above-mentioned hysteresis data, we can roughly estimate the critical pressure for this change as a  $p_c \sim 3.2$  GPa.

### ErCo<sub>2</sub> - AC susceptibility under pressure

The AC susceptibility of the ErCo<sub>2</sub> sample has been measured under pressures up to  $\sim 3$  GPa using the home-made detection coil setup, described in section 4.1.2. Data measured in zero external magnetic fields in the temperature range 10 – 110 K are displayed in Fig. 4.22. In our work we focused on two main topics, the influence of pressure on the ferrimagnetic ordering and the onset of paramagnetism. As discussed in 4.2.2, the experimental arrangement proved itself to be very efficient in spotting the signs of the later one, which is essentially very tiny bump in the AC data around flipping temperature  $T_f$ . For the sake of clarity, both effects are displayed in separate graphs.

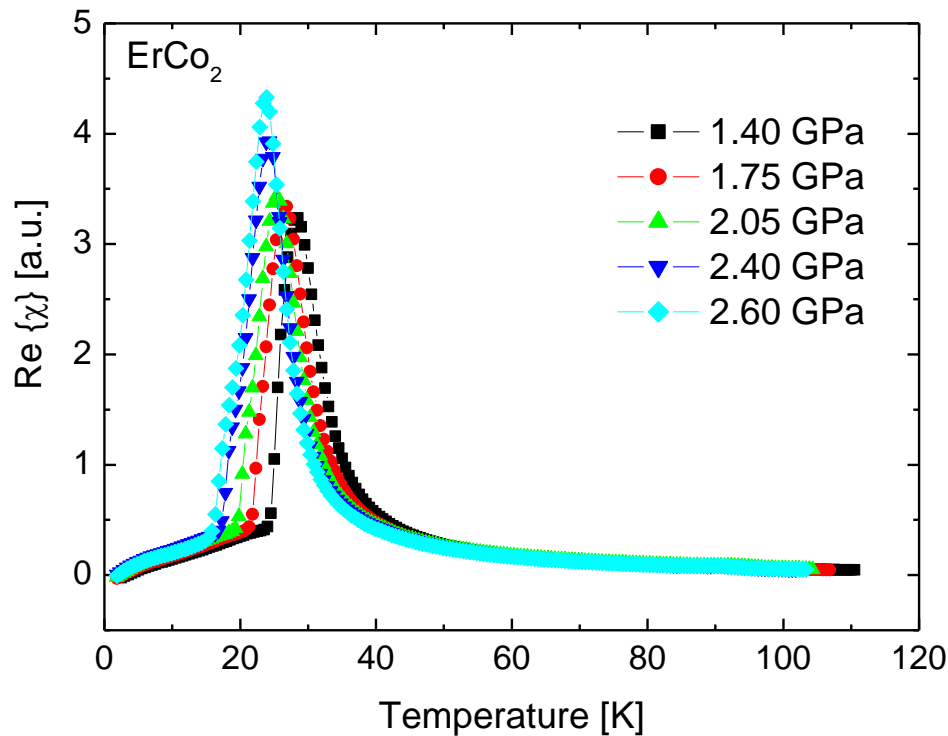


**Fig. 4.22:** Temperature dependence of AC susceptibility of the ErCo<sub>2</sub> under high pressures.

## Situation at $T_C$

Detail of the measured AC susceptibility in the vicinity of transition temperature  $T_C$  is shown in the Fig. 4.23 a). An interesting feature of the measured curves is the qualitative change of the shape of the susceptibility peak at  $T_C$  with applied pressure. At higher pressures, the peak appears to be broadened and showing the onset of splitting. To corroborate the previously proposed scenario of decoupling of the ordering of Er and Co sublattices [78], data were analyzed under the assumption that measured curves are convolution of the contributions of the individual sublattices. Indeed, data can be fairly successfully deconvoluted into the two Gaussian peaks, as it is demonstrated in the Fig. 4.23 b) for the curve measured at 2.6 GPa.

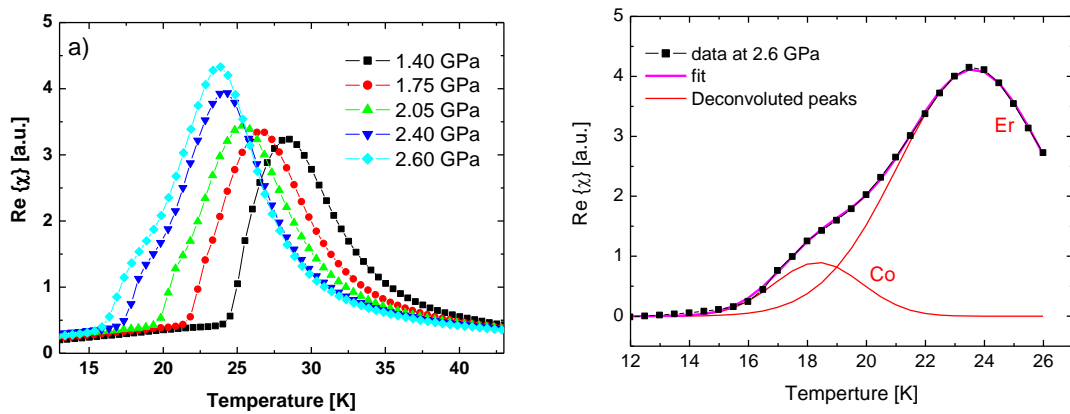


**Fig.4.23** a) Detail of the AC susceptibility data of  $\text{ErCo}_2$  in the vicinity of  $T_C$ , b) Curve measured at 2.6 GPa, deconvoluted for the contributions of Co and Er sublattices.

First sign of this splitting is visible by the naked eye already on the curve measured under pressure of 1.75 GPa. Up to that pressure the rate of decrease of the  $T_C$  is roughly the same as in the case of resistivity and specific heat measurements. Above the 1.75 GPa, the lower of the splitted peaks follows the original slope, whereas the upper peak deviates from this trend and follows a linear dependence under a different rate of change with the applied pressure:  $dT/dp \sim -3$  K/GPa. Despite the fact that the different experiments were not run at precisely same pressures, the positions of the deconvoluted peaks in the AC susceptibility data roughly coincide with the inflex points of the anomalous shape of the resistivity

curves. A tentative  $p$ - $T$  phase diagram comprising all measured physical quantities is shown in Fig. 4.24.

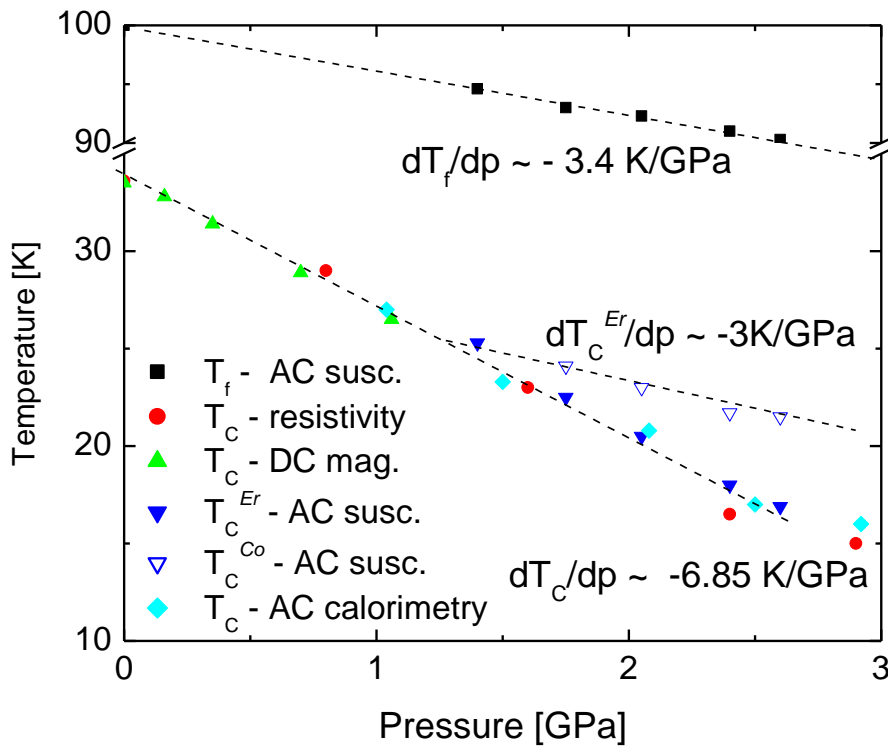


**Fig. 4.24:** Tentative  $p$ - $T$  phase diagram of the ErCo<sub>2</sub> compound based on the results of all types of measurements in this work.

### „Parimagnetism“

Fig. 4.25 a) shows the detail of measured AC susceptibility data of ErCo<sub>2</sub> sample in the paramagnetic region in the vicinity of the flipping temperature  $T_f$ . For further analysis of the anomaly at  $T_f$  as a function of applied pressure, Currie-Weiss fit of the data measured above  $T_C$  has been subtracted from the original data. The resulting data after the subtraction, Fig. 4.25 b), clearly show the peak-like anomaly at  $T_f$  and reveal a linear decrease of the flipping temperature  $dT_f/dp \sim -3.4$  K/GPa.

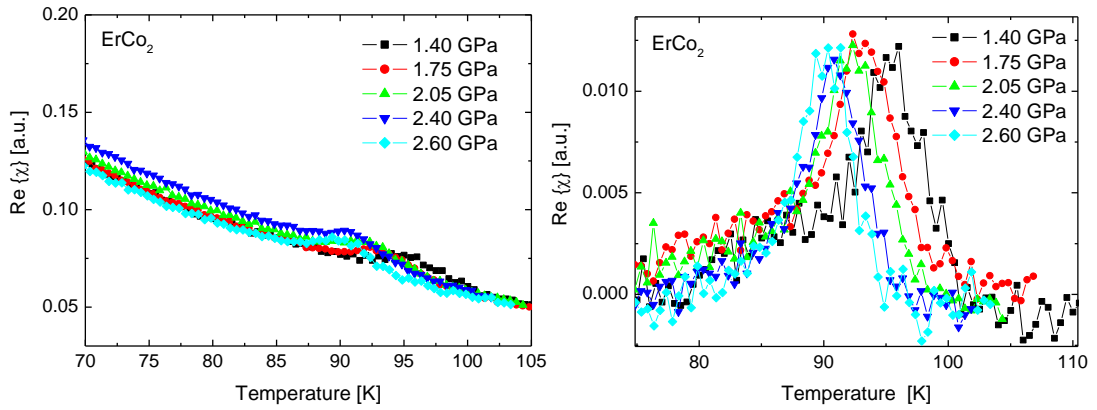


**Fig. 4.25** a) AC susceptibility of  $\text{ErCo}_2$  under high pressures, in the vicinity of flipping temperature  $T_f$ , b) Same data after subtraction of Curie-Weiss fit, showing the pressure evolution of the anomaly at  $T_f$ .

### **$\text{ErCo}_2$ – Magnetization behavior under very high pressures**

To investigate the properties of  $\text{ErCo}_2$  compound at higher pressures above  $p_c$  (the pressure at which the Co moment is supposed to be suppressed), we prepared the magnetization measurements in the MPMS7 SQUID magnetometer using the “turnbuckle” diamond anvil cell [45] designed in the CSEC. Due to the very small sample size that can be used in DAC’s, precise determination of its mass (typically  $\sim 1 - 10 \mu\text{g}$ ) and consequently, direct evaluation of absolute values of measured magnetization, is not possible. Data obtained at low pressures with the DAC were compared to those measured using the piston-cylinder pressure cell (and much larger sample) and all data measured at higher pressures were renormalized accordingly.

Fig. 4.26 a) shows the magnetization isotherms measured at the temperature  $T = 5 \text{ K}$  and a zero-field-cooled temperature scan in the magnetic field of  $0.1 \text{ T}$  is shown in the Fig. 4.26 b). Broadening of the transition at the  $T_C$  caused by the considerable pressure inhomogeneity in the sample area in pressures above  $\sim 2 \text{ GPa}$  (freezing of the Daphne 7373 pressure medium) makes the data evaluation somewhat difficult, however, slight increase of ordering temperature  $dT_C/dp \sim + 0.65 \text{ K/GPa}$  above the pressure of  $3 \text{ GPa}$  is clearly observable. Increase of the saturated magnetization in the low pressure region, obtained by comparing first two pressure

points measured at 0.6 GPa and 3 GPa, roughly agrees with the results of the previous measurements with the piston-cylinder cell. Above the 3 GPa, a slight linear decrease of saturated magnetization  $dM_S/dp \sim -0.03 (\mu_B/f.u.)/GPa$  is observed.

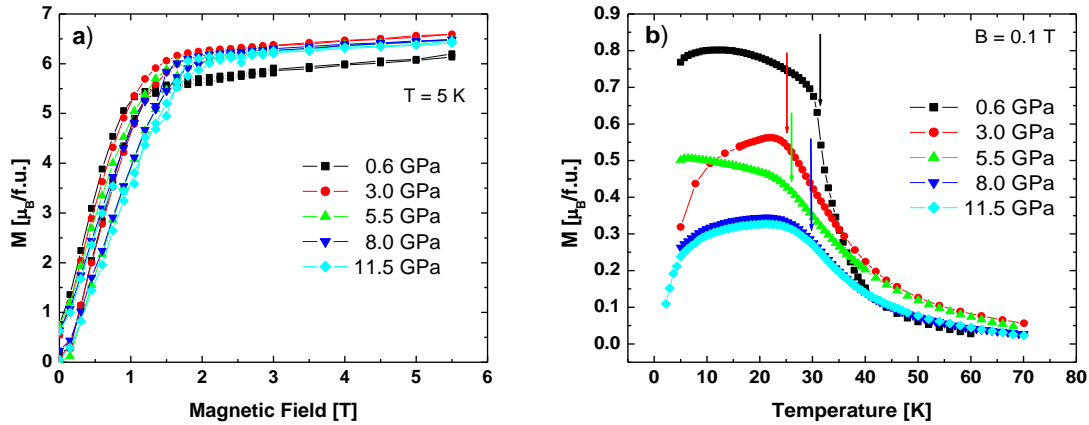


**Fig. 4.26** a) Magnetization curves of  $ErCo_2$  measured at  $T = 5$  K, b) ZFC temperature dependence of magnetization of  $ErCo_2$  measured in the field 0.1 T.

### Influence of the silicon substitution for cobalt

The magnetization, electrical resistivity and AC susceptibility of the polycrystalline  $Er(Co_{0.975}Si_{0.025})_2$  sample have been measured under high hydrostatic pressures, using the same experimental arrangements and environment conditions as in the case of the experiments with the „parent“  $ErCo_2$  sample. Striking changes of properties with the substitution of 2.5% of Si for Co can be observed already at the ambient pressure. First, the increase of the ferrimagnetic ordering temperature  $T_C$  from 33 K to 43 K has been observed in all types of measurements. Contrary to that, the value of the flipping temperature  $T_f$  has decreased from  $\sim 98$  K to  $\sim 74$  K.

The results of magnetization measurements are displayed in Fig. 4.27. Applied pressure yields the same tendency of shifting the transition to lower temperatures, with little higher rate  $dT_C/dp \sim -10$  K/GPa. The value of the saturated magnetization tends to increase under pressure as well, however, the pressure dependence is considerably smaller and non-linear. Comparing the measurements at ambient pressure and 1 GPa, the saturation magnetization increased by  $0.1 \mu_B$ , which is roughly half of the value observed in the  $ErCo_2$  sample.

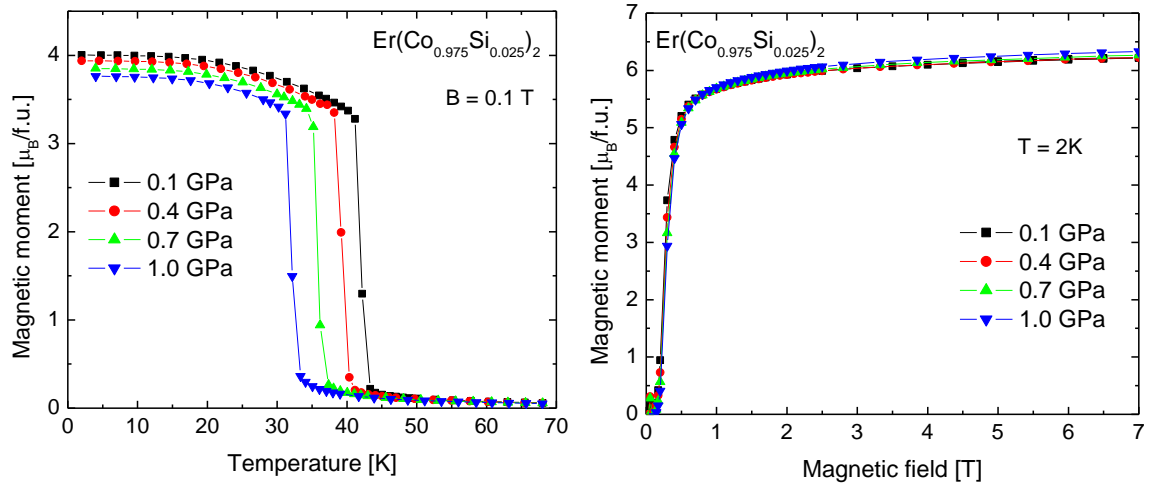


**Fig. 4.27** a) Temperature dependence of magnetization of  $\text{Er}(\text{Co}_{0.975}\text{Si}_{0.025})_2$  under pressure, b) Magnetization curves of  $\text{Er}(\text{Co}_{0.975}\text{Si}_{0.025})_2$  measured at  $T = 2$  K.

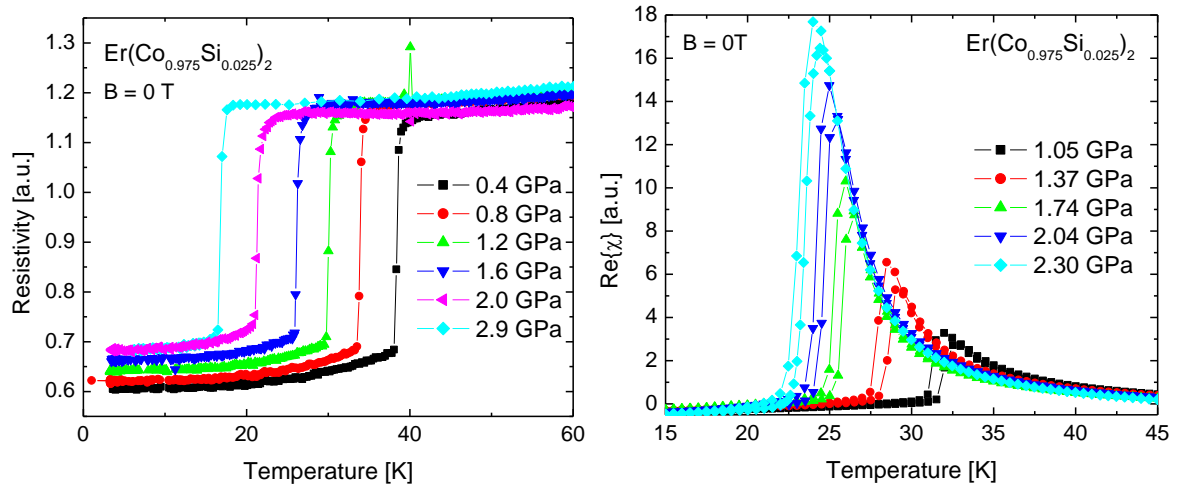


**Fig. 4.28** a) The resistivity of  $\text{Er}(\text{Co}_{0.975}\text{Si}_{0.025})_2$  under high pressures, b) The AC susceptibility data of  $\text{Er}(\text{Co}_{0.975}\text{Si}_{0.025})_2$  under high pressures.

Some minor qualitative differences can be observed as well. Compared to the parent compound, the  $\text{Er}(\text{Co}_{0.975}\text{Si}_{0.025})_2$  sample shows a tendency of much faster saturation of the low-temperature magnetization curves and a sharper step-like transition at  $T_C$  observed in the temperature dependence of the magnetization. Qualitatively different behavior, with respect to  $\text{ErCo}_2$ , with the applied pressure has been observed in the AC susceptibility and the electrical resistivity measurements as well. Measured data are shown in Fig. 4.28. Compared to the results obtained on  $\text{ErCo}_2$ , the resistivity curves lack the anomalous upturn just above the  $T_C$ . Moreover, the character of the

measured curves remains identical under highest applied pressure unlike in the  $\text{ErCo}_2$  case. Together with the shape of the magnetization data, this can be attributed to the diminished role of the spin fluctuations in the system and a stabilization of the magnetism of the cobalt sublattice. In accordance, no apparent splitting of the AC susceptibility peak with the pressure has been observed. As can be seen in the Fig. 4.29, the pressure dependence of the value of ordering temperature  $T_C$  is also modified. In the lower pressures, the decrease  $dT_C/dp \sim -10$  K/GPa is consistent with the magnetization data. However, above the  $p \sim 1.7$  GPa, the slope changes roughly to  $\sim -3.2$  K/GPa.

The anomaly in the AC susceptibility data at the flipping temperature  $T_f$  has been observed as well. However, the small peak-like structure is much more subtle at higher pressures compared to the measurements on the  $\text{ErCo}_2$ , which hampered a little the data evaluation. The evolution of  $T_f$  under pressure is presented in Fig. 4.29. A nonlinear decrease of the  $T_f$  has been observed. To allow at least some rough comparison with the parent  $\text{ErCo}_2$  compound, the values from the measurement at ambient an highest applied pressure can be compared, leading to a pressure induced shift  $dT_f/dp \sim -5.4$  K/GPa.

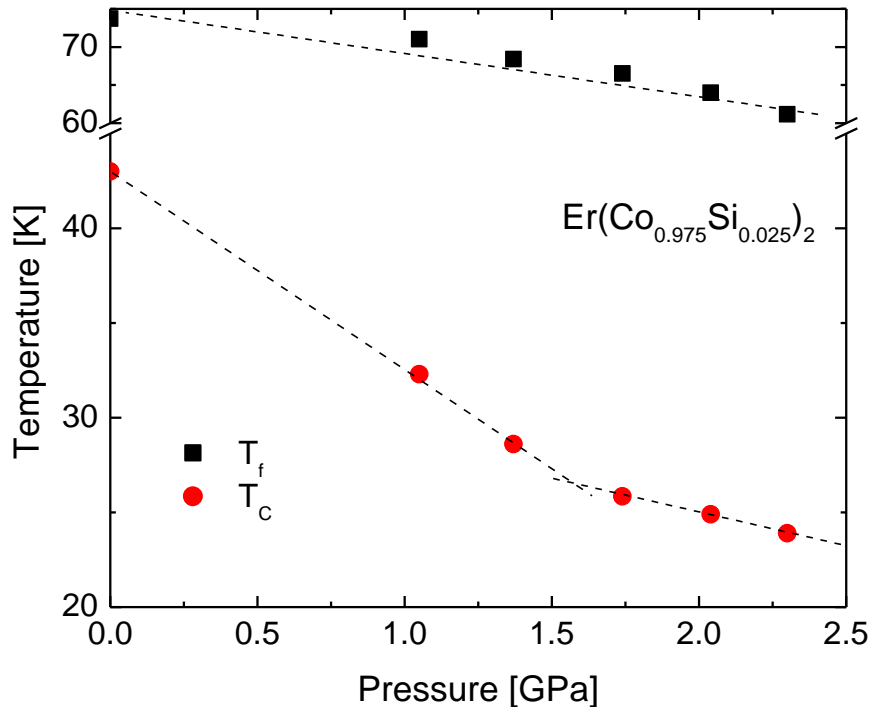


**Fig. 4.29:**  $p$ - $T$  phase diagram of  $\text{Er}(\text{Co}_{0.975}\text{Si}_{0.025})_2$ .

#### 4.2.2.2 HoCo<sub>2</sub> and Ho(Co<sub>0.975</sub>Si<sub>0.025</sub>)<sub>2</sub>

##### HoCo<sub>2</sub>

Due to the impending question of the nature and origin of the paramagnetic phenomenon and the effects observed on the ErCo<sub>2</sub> system, most of the efforts of our high pressure study of the HoCo<sub>2</sub> compound have been devoted to the AC susceptibility and resistivity measurements. Obtained results show several characteristics resembling the behavior of ErCo<sub>2</sub>. First, the applied pressure leads to the decrease of the temperature of ferrimagnetic ordering  $dT_C/dp \sim -12.3$  K/GPa. Similar tendency of the splitting the AC susceptibility peak at  $T_C$  can be clearly seen as well. However, due to the complicated shape of the peak, the data cannot be easily deconvoluted as in the case of ErCo<sub>2</sub>. The flipping temperature decreases with applied pressure as well, with the rate  $dT_f/dp \sim -11.2$  K/GPa. In addition pressure induced increase of the spin reorientation temperature  $dT_R/dp \sim +4.1$  K/GPa has been found. Fig. 4.30 shows the details of the AC susceptibility measurements on HoCo<sub>2</sub>, all results are summarized in the phase diagram, Fig. 4.31.

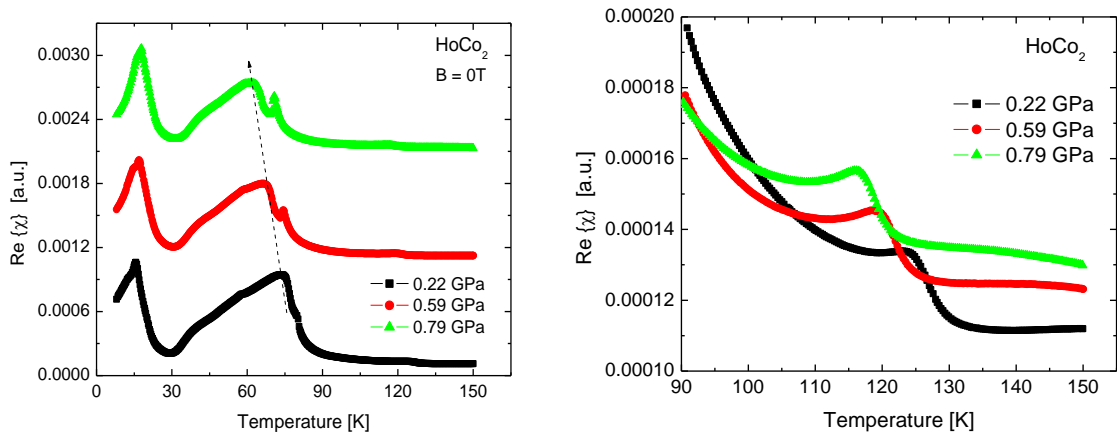


**Fig. 4.30:** AC susceptibility data of HoCo<sub>2</sub> under high pressures (left) and the detail showing the pressure evolution of the anomaly at  $T_f$  (right).

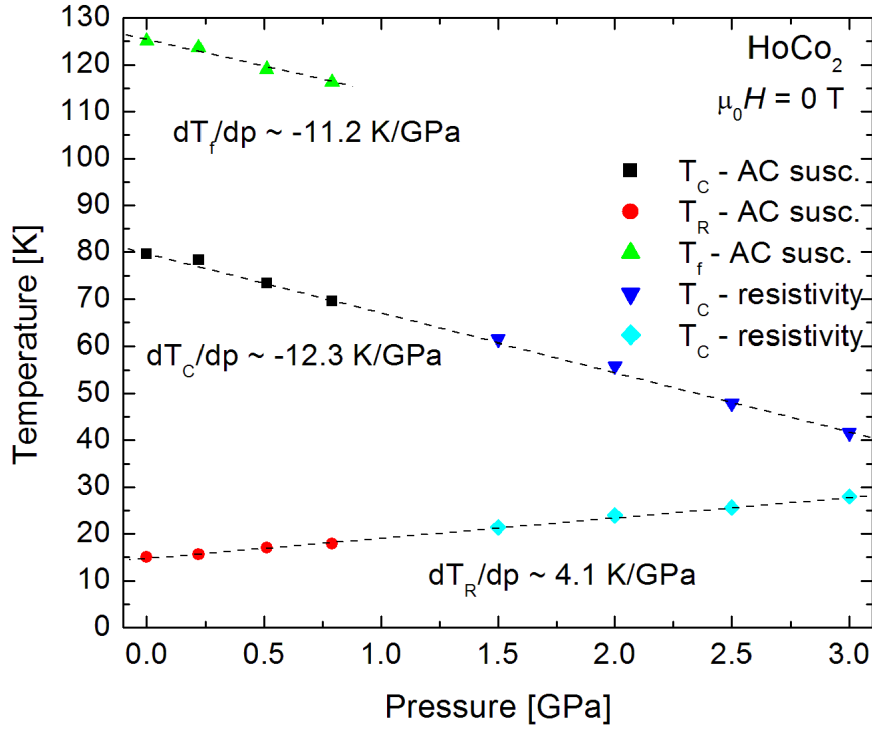


**Fig. 4.31:** Tentative  $p$ - $T$  phase diagram of the  $\text{HoCo}_2$  compound.

### $\text{Ho}(\text{Co}_{0.975}\text{Si}_{0.025})_2$

The substitution of silicon into the cobalt sublattice demonstrates some resemblance with the Er-based counterparts as well. The substitution of 2.5 % of Si leads to the increase of ordering temperature from 79.6 K to 90.6 K, the flipping temperature decreases from  $\sim 125$  K to  $\sim 117$  K (both at ambient pressure). In addition, one more similar feature has been identified in the susceptibility data at the temperature  $\sim 148$  K, here denoted as  $T_{f2}$ . As for the pressure induced changes, the substituted sample exhibits the higher rates of change of  $T_C$  and  $T_f$  compared to the parent  $\text{HoCo}_2$  compound.

The spin reorientation temperature decreased with 2.5 % substitution from 16.5 K to  $\sim 9.1$  K, however, the evolution with pressure remains almost the same as for the non-substituted sample,  $dT_R/dp \sim 4$  K/GPa

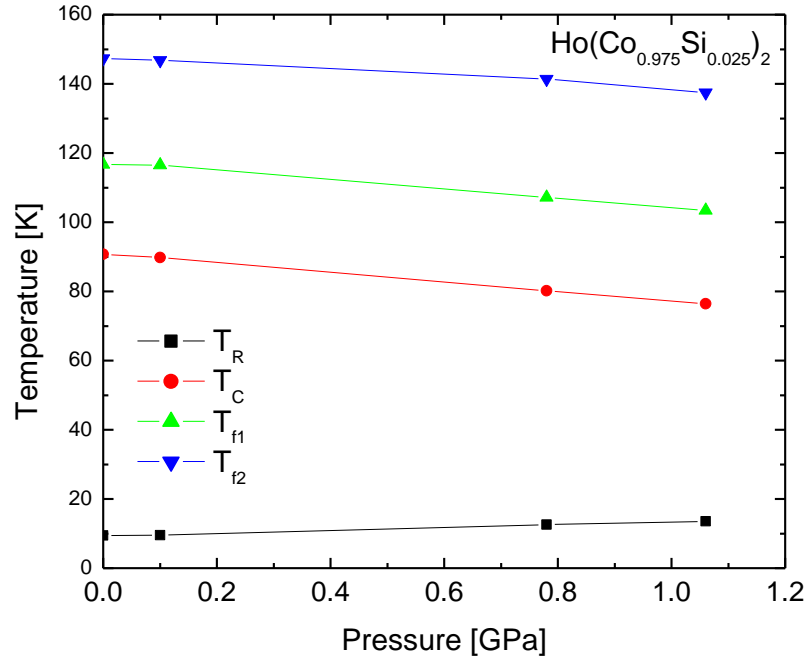


**Fig. 4.32:** Tentative  $p$ - $T$  phase diagram of the  $\text{Ho}(\text{Co}_{0.975}\text{Si}_{0.025})_2$  compound.

### 4.2.3 Conclusions

We have thoroughly studied the influence of external high hydrostatic pressures on the properties of the  $\text{ErCo}_2$  compound. All types of experiments have consistently revealed the decrease of the temperature of ferimagnetic ordering  $dT_C/dp \sim -6.85$  K/GPa in the pressures up to  $\sim 1.7$  GPa. Above this pressure, situation becomes more complex. The splitting of the AC susceptibility peak at  $T_C$  has been observed, corroborating the previously proposed scenario of decoupling of the magnetic ordering of Er and Co sublattices [78]. The loss of temperature hysteresis confirms the change of the order of the transition from 1<sup>st</sup> to 2<sup>nd</sup> type, which has been predicted as well. The anomaly in the AC susceptibility data in the paramagnetic region of  $\text{ErCo}_2$ , related to the onset of „parimagnetism“ [50-52] has been observed.

Our results clearly demonstrated that even very small substitution of Si for Co has a dramatic effect on magnetic properties of the  $\text{ErCo}_2$  compound.  $T_C$  increased from 33.5 K to 43 K by a substitution of 2.5 % of Si, whereas  $T_f$  dropped from the 98 K to 74 K.

The sharp transition of the  $M(T)$  curves at  $T_C$ , much faster saturation of the low temperature  $M(H)$  curves with applied field and a shape of the resistivity curves missing the anomalous upturn above the  $T_C$  suggest much weaker role of spin fluctuations. Furthermore, most of the measured properties lack the significant qualitative changes with the applied pressure, which has been observed in the parent  $\text{ErCo}_2$  compound. The obtained results clearly point to a conclusion that magnetism of the cobalt sublattice is stabilized with the silicon substitution. This is most evident from the character of the resistivity curves which remains intact by pressure and a fact that no apparent splitting of the AC susceptibility data at  $T_C$  has been observed.

In the  $\text{HoCo}_2$  and  $\text{Ho}(\text{Co}_{0.0975}\text{Si}_{0.025})_2$  samples, the decrease of the ordering temperature has been observed, with the rates  $dT_C/dp = -12.3$  K/GPa and  $dT_C/dp = -12.8$  K/GPa, respectively, well fitting the previously published results [80]. The anomalous bump at the AC susceptibility data, reflecting the cobalt clustering and the onset of paramagnetism has been observed at  $T_f = 125$  K and  $T_f = 117$  K. In addition, one more transition at  $T_{f2} = 148$  K has been observed in the  $\text{Ho}(\text{Co}_{0.975}\text{Si}_{0.025})_2$  sample. Recent paper of Herrero-Albillos et. al. [82] reported this effect by means of the XMCD experiments in the parent  $\text{HoCo}_2$  compound as well. Their measurements were performed in the applied field of 1 T. Assuming the similarly strong dependence of  $T_f$  on the applied magnetic field as in the case of  $\text{ErCo}_2$  [51], it is highly likely that the effect eluded our measurements just due to the limited temperature range of the measurements and further experiments are in the preparation.

In addition to the ferimagnetic ordering at  $T_C$  and paramagnetism phenomenon around the  $T_f$ , the spin reorientation from the [100] to [110] easy direction of magnetization occurs in the case of the  $\text{HoCo}_2$  compound (at  $T_R = 16.5$  K at ambient pressure [79]). This effect is reflected in both, AC susceptibility and the resistivity measurements which has been studied in this work. With the 2.5 % silicon substitution, the spin reorientation temperature  $T_R$  shifts to lower temperatures, from 16.5 K to  $\sim 9.1$  K. Preliminary measurements of the sample with higher content of the silicon (7.5 %) have shown further decrease of the  $T_R$  ( $\sim 5$  K), suggesting the complete suppression of the spin reorientation effect for concentrations  $\sim 20$  %. On the other hand, the pressure induced change of the  $T_R$  remains almost identical for the parent and the 2.5% substituted sample,  $dT_R/dp \sim +4$  K/GPa in both cases.

### 4.3 Magnetism in UNiGa under uniaxial and hydrostatic pressure

#### 4.3.1 Introduction and previous results

Magnetic properties of uranium, as one of actinides, originate in the partially occupied 5f-electron shell. Contrary to the strongly localized 4f states of the rare earths, the 5f states of uranium are considerably more extended in space. The 5f-wavefunctions of neighboring ions may strongly overlap (5f-5f overlap), the probability of intersite electron hopping increase, the 5f-electrons become delocalized and the 5f-wavefunctions lose the original atomic character with necessary consequences to magnetic moment formation. The 5f-5f overlap and consequently the degree of the 5f-electron delocalization critically depend on the intersite distance of the nearest uranium ion neighbors ( $d_{U-U}$ ). Using this simple concept, H. Hill has classified U compounds within the diagram with  $d_{U-U}$  on the horizontal axis and the magnetic ordering and superconducting temperature on the vertical axis. The Hill limit ( $d_{U-U} \sim 3.5 \text{ \AA}$ ) roughly divides the Hill plot in two parts where for lower  $d_{U-U}$  superconductors appear by rule whereas the magnetically ordered materials are mostly characterized by higher  $d_{U-U}$  values. Similar to transition metals ( $T$ ) characterized by the overlap of 3d (4d or 5d)-wavefunctions of neighboring  $T$  ions the 5f-5f overlap in U compounds brings two mutually competing effects in magnetism: i) washing out and reducing local U magnetic moments, ii) facilitating direct exchange interaction between the U magnetic moments. In compounds the extended U states easily hybridize with valence electron states of ligands. The degree and character of the 5f-ligand hybridization critically depends on the ligand species, the geometry U ion neighborhood and U-ligand intersite spacing. Also the 5f-ligand hybridization delivers two competing mechanisms to uranium magnetism: i) perturbation/reduction of the 5f-electron magnetic moments ii) mediation of indirect exchange interaction between pairs of the U magnetic moments surrounding the ligand.

The strong spin orbit coupling in actinides provides a mechanism for significant orbital polarization in the 5f band systems with consequent coupling of the 5f magnetic moments to the crystal structure, which is most evidently demonstrated by huge magnetocrystalline anisotropy. Besides the single ion anisotropy characteristic for rare-earth compounds the two-ion mechanism caused by the hybridization

induced exchange interaction becomes important in majority of U compounds [86]. As a consequence the hard magnetization axis appears by rule perpendicular to the U-U nearest neighbor planes (chains) leading to the easy axis (easy plane) anisotropy. The specific character of the 5f-electron magnetism in uranium compounds appearing between localized and itinerant due to various 5f-5f overlap and 5f-ligand hybridization implies the sensitivity of magnetic properties to the variation of the external parameters like magnetic field, pressure or alloying with other elements.

UNiGa is one of the most thoroughly studied materials in the UTX group of compounds ( $T$  = transition metal,  $X$  = p-metal) crystallizing in the hexagonal ZrNiAl – type crystal structure (space group P-62m) [16]. The structure is built of layers of the U- $T$  (U-Ni) and  $T$ - $X$  (Ni-Ga) basal planes, respectively, alternating along the  $c$ -axis, Fig. 4.33.

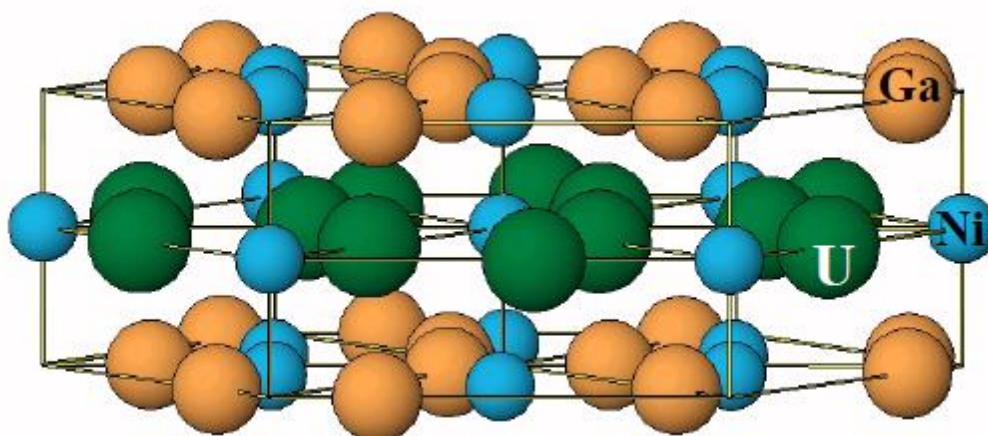


**Fig. 4.33:** Crystal structure of the UNiGa compound.

The closest distance of uranium ions,  $d_{U-U} = 3.46 \text{ \AA}$ , appears within the basal plane (lattice parameter  $a = 6.73 \text{ \AA}$ ). Along the  $c$ -axis, the distance between uranium sheets separated by one Ni-Ga layer is  $4.02 \text{ \AA}$  ( $= c$ ) [16]. Within the Hill concept, UNiGa appears just at the Hill limit. One should be, however, aware that the nearest U-U ions are locked exclusively within the basal plane which gives to UNiGa magnetism low-dimensional character. The sensitivity of the compound to the subtle changes of external variables has been documented by previous investigations. Namely the

deviations of the composition from the ideal stoichiometry were most probably responsible for the conflicting results in the early stages of the research, where the UNiGa has been claimed to order antiferromagnetically [87, 88], ferromagnetically [89] or classified as a spin glass [90]. As a result of the distribution of the U ions in the crystal structure, strong ferromagnetic coupling of the uranium moments within the basal planes is observed and huge magnetocrystalline anisotropy locks the uranium magnetic moments along the crystallographic c-axis which is the easy magnetization axis. Magnetic fields as high as 35 T applied perpendicular to the c-axis does not change the magnetic state of the compound and find only a very weak paramagnetic response in the corresponding magnetization curve [91]. The magnetic phase transitions discussed below are observed only in magnetic fields applied along the c-axis. Therefore all the results presented in this chapter are exclusively referring to this field direction. UNiGa orders antiferromagnetically through the second order magnetic phase transition with  $T_N \sim 39$  K. With the temperature further decreasing, three order-to-order transitions between different AF phases were observed in zero external magnetic field in the temperature range  $\sim 34 - 39$  K [16]. All these phases are characterized by collinear magnetic structures with uranium moments locked along the c-axis. Previous neutron diffraction experiments revealed absence of any magnetic moment on Ni and Ga sites [92]. The recent polarized neutron and resonant x-ray scattering experiments, however, concluded the existence of a small, non-zero in-plane component of magnetization which could not be attributed to the 5f uranium moments [93].

Given the strong coupling of uranium moments within the basal planes and weak inter-plane coupling, all these magnetic structures are built of basal-plane sheets of ferromagnetically coupled U moments, distinguished from each other just by different “stacking” of the + and – polarized ferromagnetic layers along the c-axis. Fig. 4.34 shows the complex magnetic phase diagram of UNiGa for ambient pressure and for hydrostatic pressure of 0.9 GPa (taken from [94]).

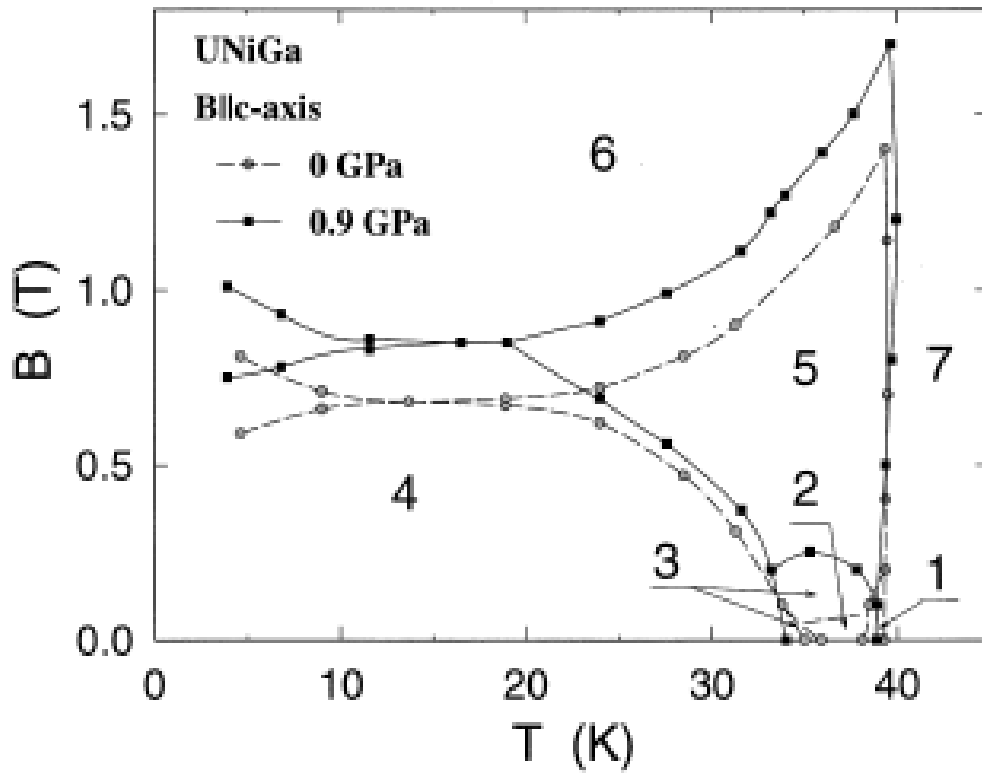


**Fig. 4.34:** Magnetic phase diagram of UNiGa under ambient and hydrostatic pressure (taken from [92]), phases 1 – 7 are described in detail in the text.

The ground state of UNiGa is characterized by the  $++-+-$  coupling (where + and – denote the orientation of the moments in the given layer) with the ordered uranium magnetic moments  $\mu_U \sim 1.4 \mu_B$  [92]. With application of the external magnetic field along the c-axis the transition to the field induced ferromagnetic structure (directly at temperatures below 10 K or via the  $++-$  uncompensated AF structure (denoted as „5“ in the Fig 4.36) at higher temperatures) are observed. The transition below 10 K exhibits the field hysteresis, which is increasing with decreasing temperature. The AF phases in the temperature region 35 K – 39 K (denoted in the Fig 4.36. as „1“, „2“ and „3“, respectively) are characterized in the following way: (1) incommensurate structure with propagation vector  $q = \pm (0, 0, 0.36)$ , (2) commensurate sine-wave modulated „ $+ - 0$ “ structure with  $q = (0, 0, 1/3)$ , (3) commensurate square modulated structure with „ $++-+-$ “ stacking and  $q = (0, 0, 1/8)$  [92].

The magnetic phase transitions in UNiGa are associated with considerable anomalies in the electrical resistivity and magnetoresistance [16, 95] reflecting the dramatic changes of the Fermi surface due to various differences between the magnetic and crystallographic periodicity. We studied the evolution of the magnetic phase diagram

of UNiGa in pressures up to 2.88 GPa by resistivity measurements which are technically easier to realize under high hydrostatic pressures than the magnetization measurements. The magnetization measurements were performed under lower pressures only.

The effect of hydrostatic pressure on the magnetic phase diagram was previously studied by means of magnetostriction, neutron diffraction and thermal expansion and electrical resistivity measurements. The previous works concluded the suppression of several AF phases and simplification of the phase diagram and the tendency of stabilizing the antiferromagnetic ground state, i.e. shifting the critical field of metamagnetic transition to higher values.

Since the magnetism of the UNiGa compound is governed by the hierarchy of the exchange interactions along the crystallographic c-axis, varying the c-axis lattice parameter alone instead of the hydrostatic compression is highly desirable experimental option. Keeping in mind the results of the thermal expansion measurements and the previous hydrostatic pressure experiments, the opposite trend, i.e. destabilization of the antiferromagnetic order and formation of the ferromagnetic ground state, can be expected.

Detailed investigation of the influence of the uniaxial pressure on the magnetic phase diagram of the UNiGa compound has been carried out mostly by direct magnetization measurements with the SQUID magnetometer and by the neutron diffraction experiments. This work required design and construction of several new uniaxial pressure cells as well as some minor modifications of the existing ones. Details of the instrumental part of this work can be found in section 4.1. Given the known sensitivity of properties of UNiGa to impurities and slight deviations of the ideally stoichiometric composition, the reference experiments at ambient pressure and under the hydrostatic conditions have been performed as well. Due to the different requirements for sample size and shape, the two different experiments could not be performed on an identical sample; the studied samples have been cut from the same part of the newly prepared single crystal. XRPD and EDX analysis revealed no difference between them.

## 4.3.2 Results and discussion

### 4.3.2.1 Sample preparation and characterization

New single crystal of the UNiGa has been grown using the modified Czochralski method in the triarc furnace (Chapter 3). Sample structure and composition have been checked by the EDX microprobe analysis and the x-ray powder diffraction (Fig. 4.35). Laue diffraction patterns (Figs. 4.36 and 4.37) have been used to check the quality of the single crystal and orient the samples.

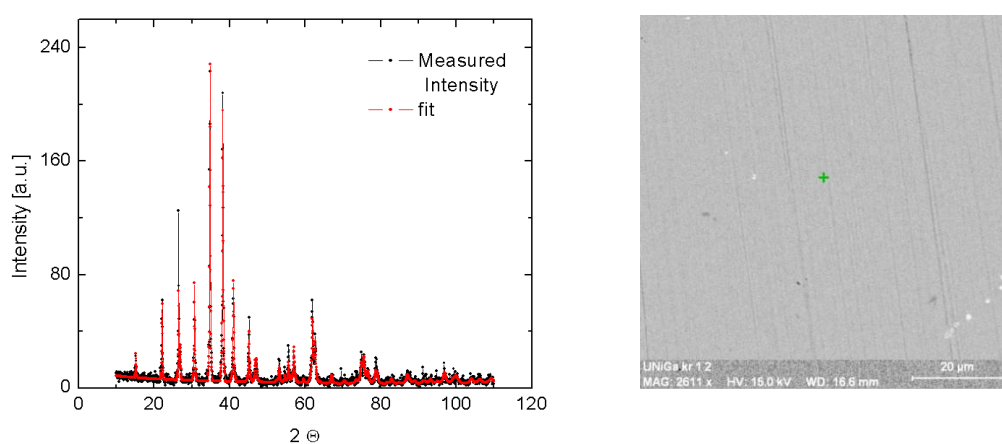


**Fig. 4.35:** X-ray powder diffraction (left) and EDX microprobe image (right) of the UNiGa crystal.

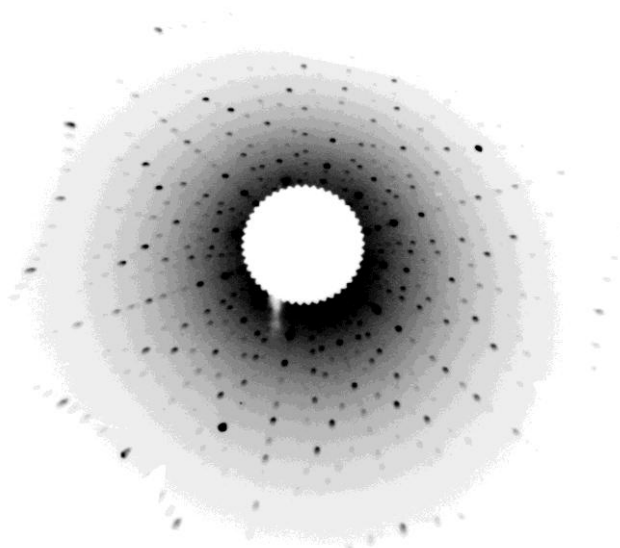


**Fig. 4.36:** X-ray Laue diffraction pattern of the oriented UNiGa single crystal.

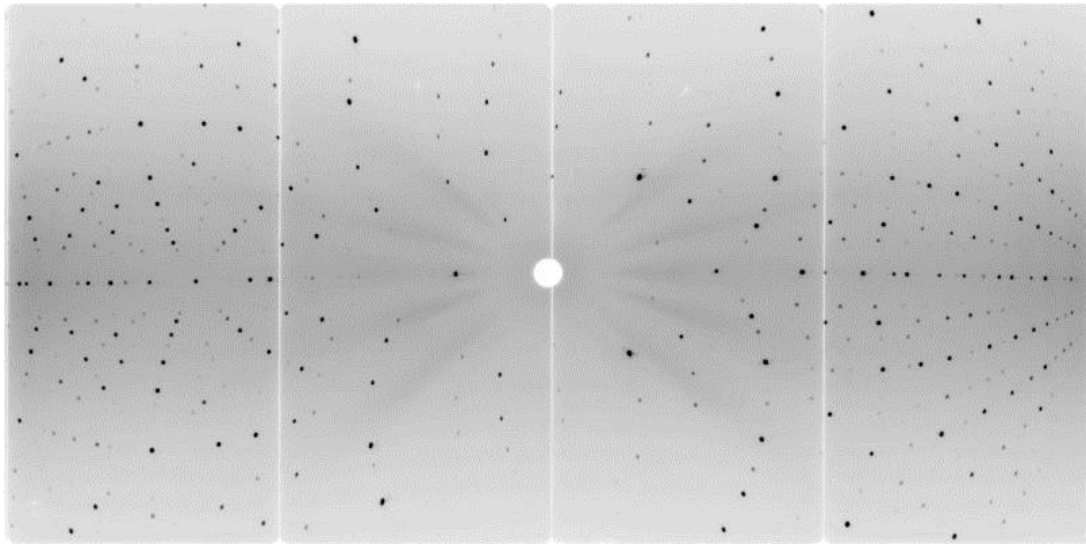


**Fig. 4.37:** Full neutron diffraction pattern of UNiGa taken at  $T = 50$  K (paramagnetic range), obtained with the VIVALDI instrument, ILL, Grenoble.

#### 4.3.2.2 Experiments under hydrostatic pressures

The magnetization measurements on the UNiGa single crystal have been carried out within the commercial SQUID magnetometer (Quantum Design) with the magnetic field oriented parallel to the  $c$ -axis of the hexagonal structure. All measurements started from the zero field cooled state (ZFC), i.e. between two subsequent measurements the sample has been heated well above the Néel temperature  $T_N$  and cooled in zero magnetic field.

Magnetization curves measured at selected temperatures under hydrostatic pressures are shown in Fig. 4.38. Note that the kink in low fields for the curves measured at low temperatures ( $\mu_0 H \sim 50 - 100$  mT,  $T = 2$  K, 5 K, top left and middle left graphs in Fig. 4.38) arises from the lead manometer and is not related to the properties of the UNiGa sample.

Judging from the unaltered value of the saturated magnetization and assumption of no significant magnetic moment on Ni and Ga sites, the value of the uranium moments is unaffected by the applied hydrostatic pressures. The ordering temperature  $T_N$  shows a mild decrease with pressure,  $dT_N/dp \sim -0.3$  K/GPa. The critical magnetic field for the transition to the field-induced ferromagnetic state

increases with the applied pressure over the entire temperature range (2 K to  $T_N$ ) and the antiferromagnetic ground state is stabilized.

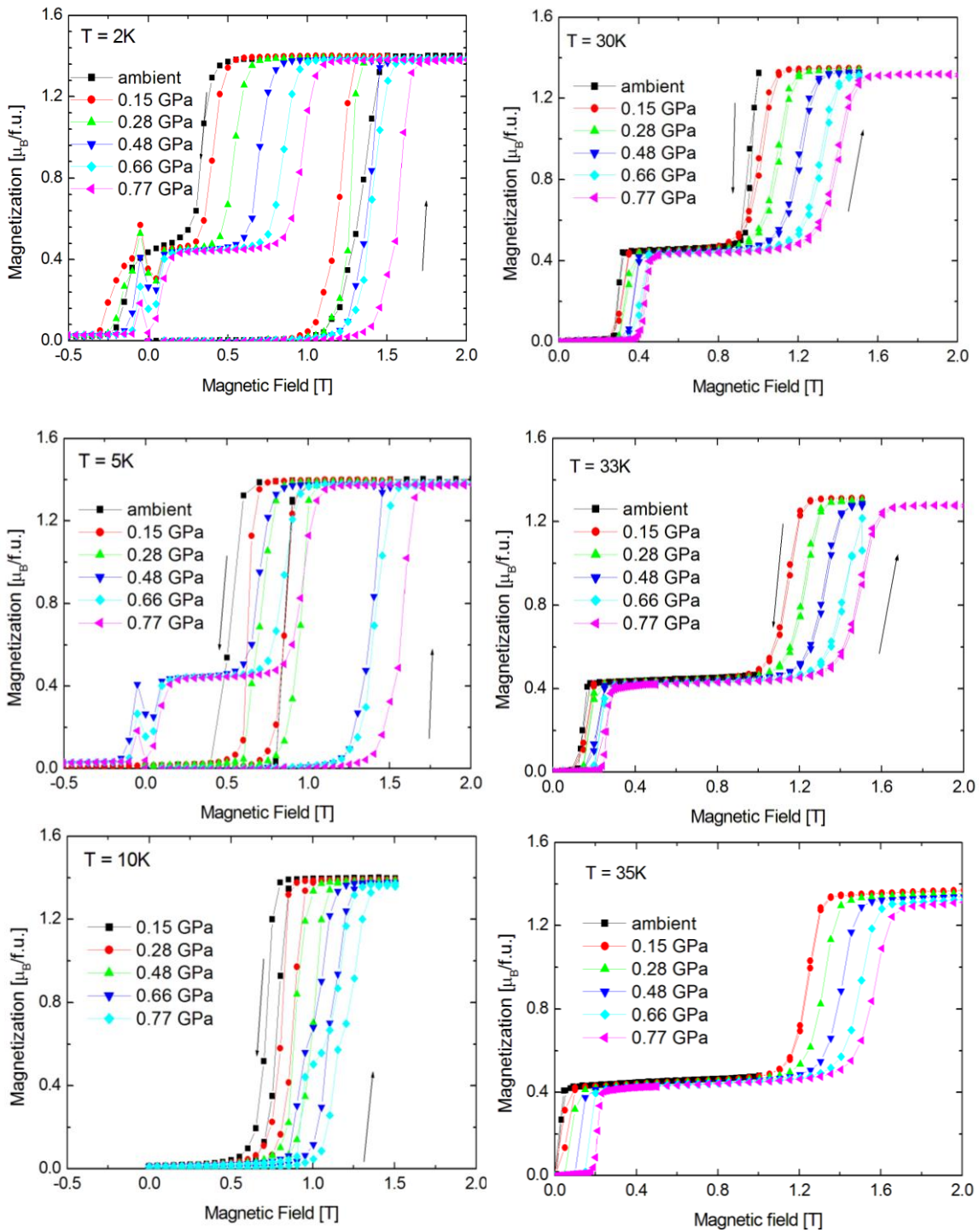


**Fig. 4.38:** Magnetization curves of UNiGa under hydrostatic pressures, magnetic field was applied along the crystallographic c-axis.

The obtained results qualitatively agree with the previous high pressure experiments [94, 96], although, one significant quantitative difference has been found. In the present experiment, the rate of change of the critical field with applied pressure  $dB_c/dp \sim 0.7$  T/GPa is roughly 2.5 times larger compared to data found in literature. Application of high pressure also affects the sequence of the different AF phases in the temperature region 35 K - 39 K. Shrinking of the temperature range, where phases 1 and 3 exist, has been observed. Results obtained from the magnetization measurement under hydrostatic pressure are summarized in the magnetic phase diagram, Fig. 4.39. Data from [94] have been included to demonstrate the quantitative differences observed in our work.

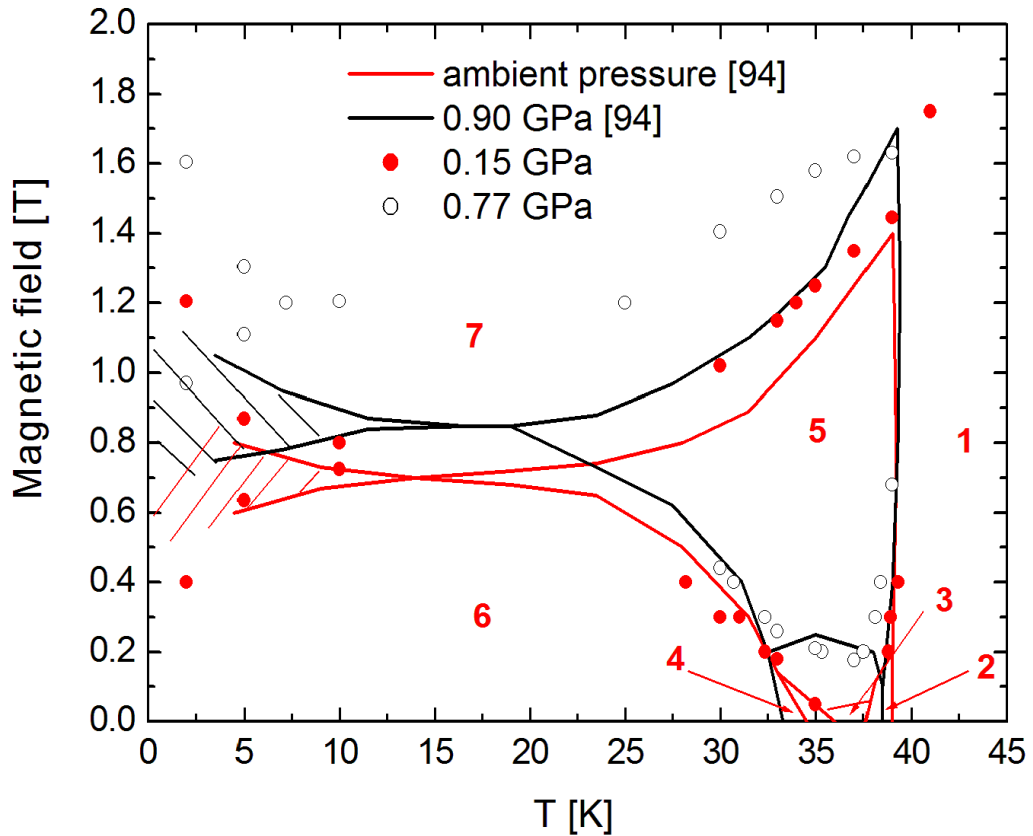


**Fig. 4.39:** Influence of hydrostatic pressures on the magnetic phase diagram of the UNiGa single crystal with the magnetic field applied along the crystallographic  $c$ -axis. Triangles represent the results obtained in this work, lines indicate the results reported previously [94], magnetic phases are labeled same way as in Fig. 4.36. Shaded area below  $T \sim 15$  K stands for the hysteresis behavior observed in the low-temperature  $M(T)$  curves.

We also measured temperature and magnetic field (applied along the c-axis) dependences of electrical resistivity (for electrical current along the c-axis) in order to probe the evolution of magnetism in UNiGa in pressures higher than reported previously (up to 1 GPa [94, 96]) and higher than pressures accessible with the magnetization measurements presented in the previous paragraph. A similar set of temperature and field dependencies of resistivity has been chosen to get the comparable „sampling“ of the phase diagram as in the case of the lower pressures.

Selected results of the hydrostatic experiments are shown in Figs 4.40 and Fig 4.41. All results are summarized in the phase diagram for the highest achieved pressure  $p = 2.88$  GPa, Fig 4.42. The resistivity data collected on UNiGa under hydrostatic pressures have shown the results consistent with the magnetization measurements in the lower pressure region – the critical field of the metamagnetic transition increased further up to  $B \sim 2.5$  T for the curve measured at  $T = 2$  K under pressure  $p = 2.88$  GPa. Phases characterized with the  $q = (0, 0, 0.36)$  and  $q = (0, 0, 1/8)$  are completely suppressed at this pressure and the lower phase boundary is shifted from the  $T \sim 35$  K at ambient pressure to  $T \sim 22.5$  K. A significant qualitative difference occurs in the low-temperature magnetoresistance curves, where the transition to the field-induced metamagnetic state is observed in two steps with both, applying and removing the magnetic field.

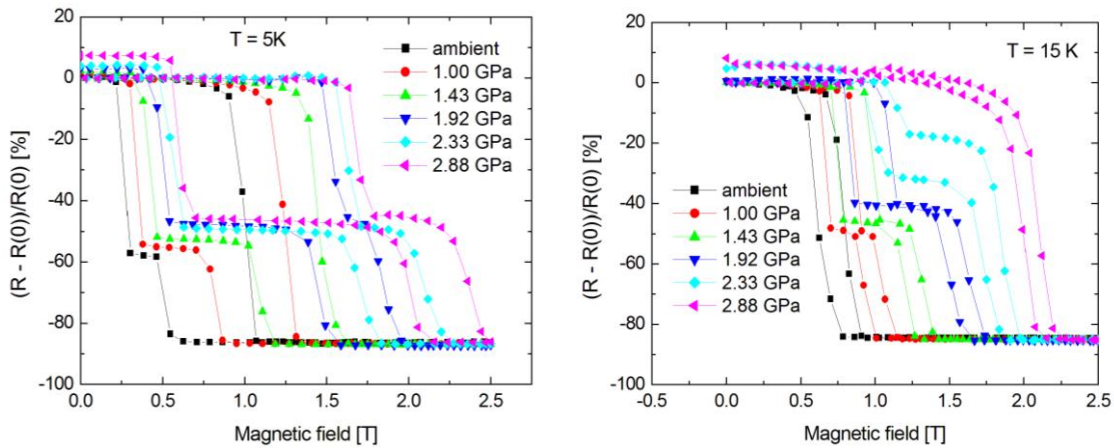


**Fig. 4.40:** Low-temperature magnetoresistance curves of UNiGa under hydrostatic pressures.

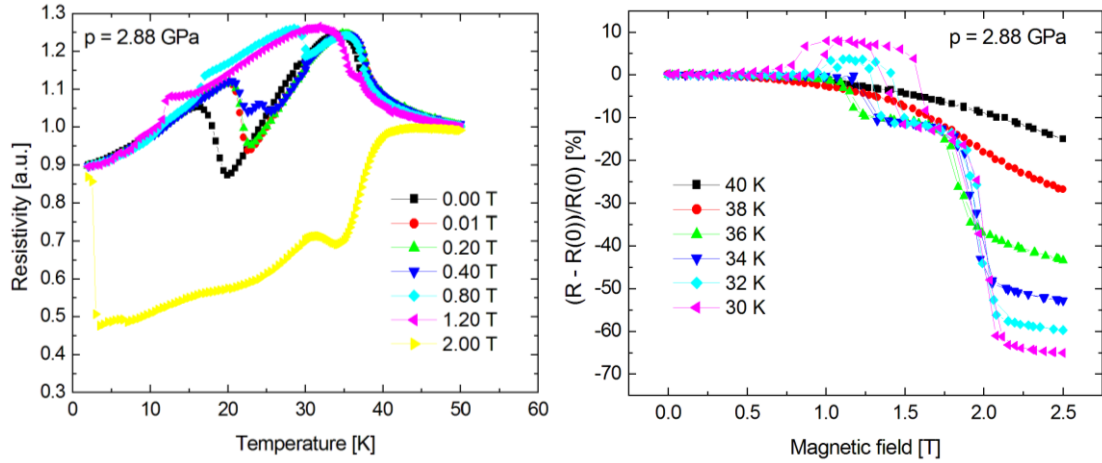


**Fig. 4.41:** Temperature dependencies of resistivity in various magnetic fields (left) and the magnetoresistance curves (right) of UNiGa under the hydrostatic pressure  $p = 2.88$  GPa.

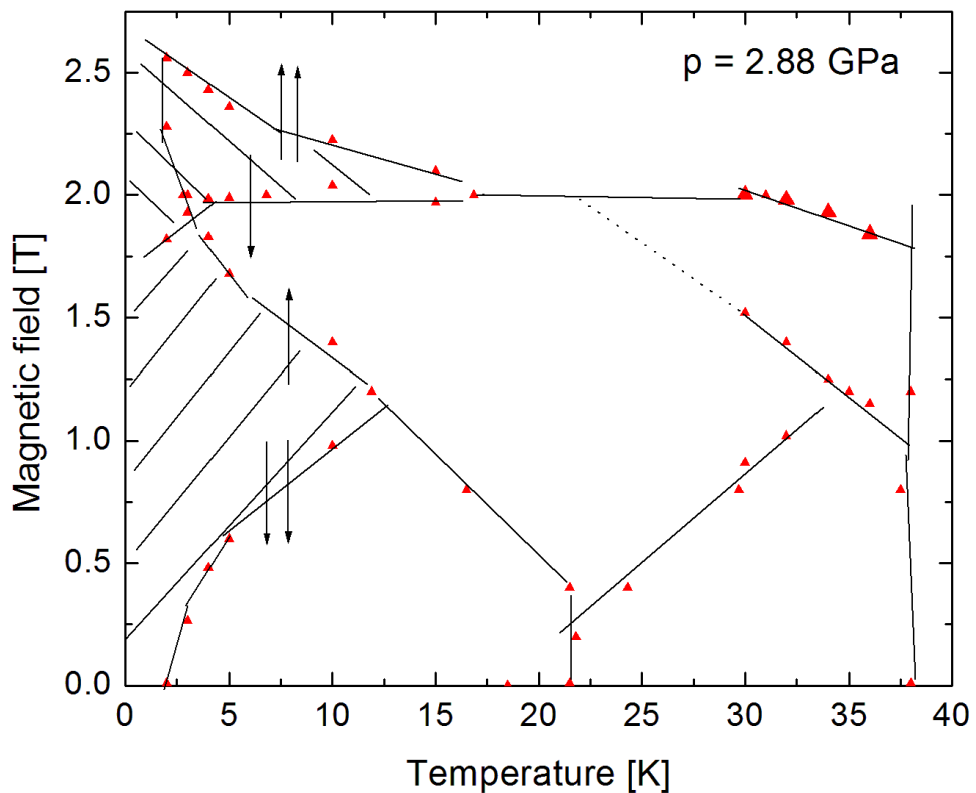


**Fig. 4.42:** Magnetic phase diagram of UNiGa under hydrostatic pressure  $p = 2.88$  GPa. Shaded area in the low-temperature region denotes the hysteresis observed in the magnetoresistance curves, arrows indicate the sequence of the „steps“ in the data ( up and down for increasing/removing the field, 1 or 2 arrows for first and second step in given field change direction, respectively).

### 4.3.2.3 Experiments under uniaxial pressures

The same set of  $M(T)$  and  $M(H)$  curves, as in the case of hydrostatic pressures, have been measured under uniaxial compression up to  $p \sim 120$  MPa along the  $c$ -axis. Results are displayed in the Figs. 4.43 and 4.44. Data measured under the uniaxial compression partially reflects inhomogeneous pressure distribution in the sample (see section 4.1.5). Due to the inherited imperfection of the method, the magnetization curves are smeared around the field induced transition. Nevertheless, the overall tendency to shift the critical fields to lower values is clearly demonstrated. Magnetization curves measured at  $T = 2$  K unambiguously display the remanent magnetization of the sample after removal of the magnetic field, corroborating the proposed scenario of forming the ferromagnetic ground state with the compression along the  $c$ -axis. Example of measured  $M(T)$  curves measured under uniaxial compression is displayed in the Fig. 4.44 together with their hydrostatic counterparts, illustrating the qualitative differences between the two types of pressure conditions. Fig. 4.45 shows selected magnetoresistance curves measured under uniaxial stress. Results of the uniaxial pressure experiments are summarized in Fig. 4.46.

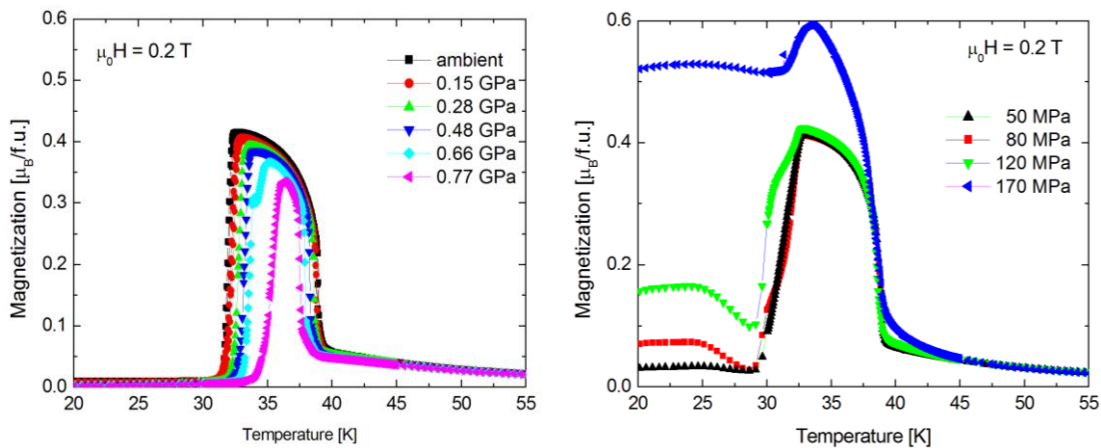


**Fig. 4.43:** Temperature dependence of the magnetization of the UNiGa single crystal with the magnetic field applied along the  $c$ -axis measured under hydrostatic pressures (left) and under uniaxial pressure (right).

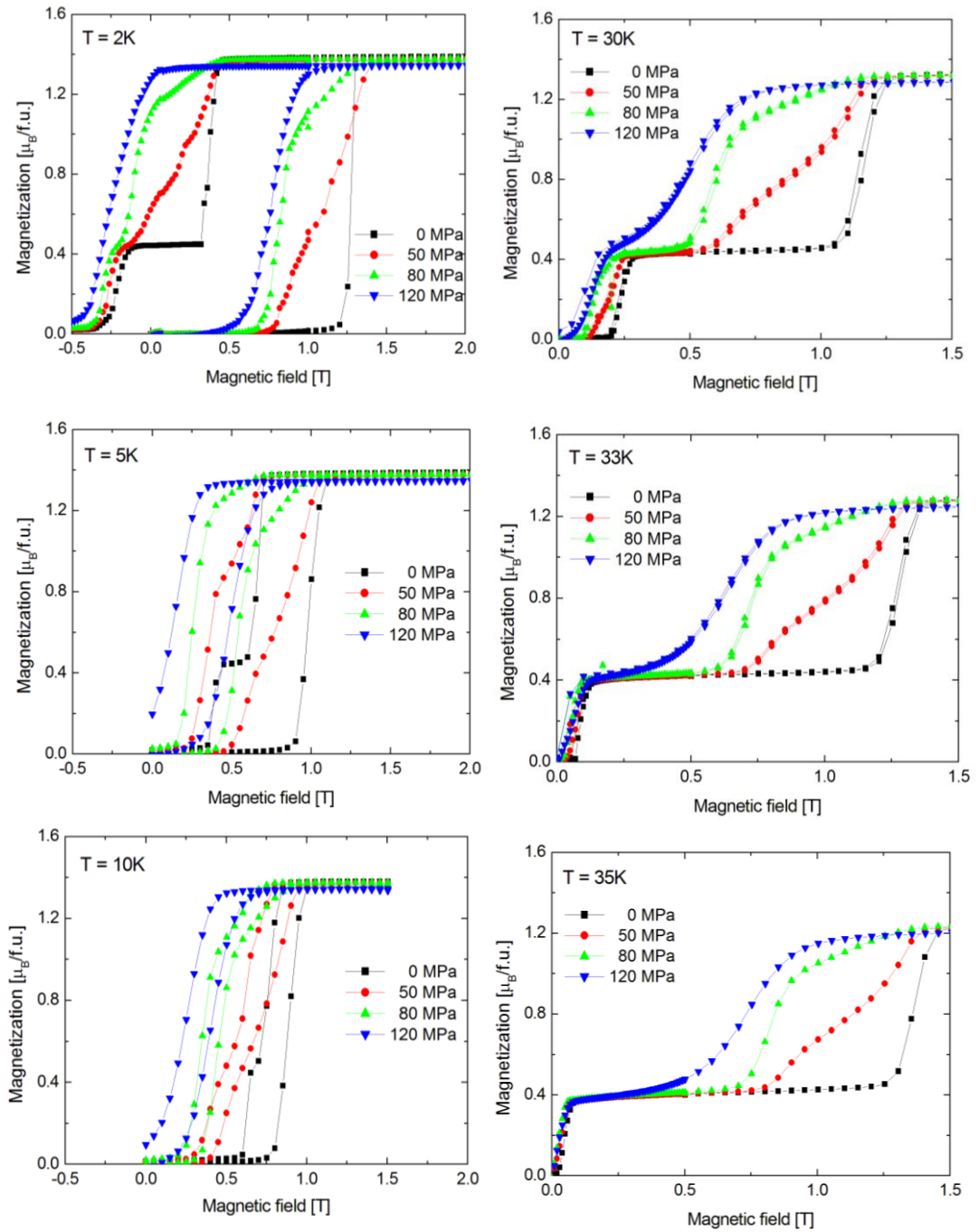


**Fig. 4.44:** Magnetization curves of UNiGa under uniaxial compression along the c-axis, magnetic field was applied along the crystallographic c-axis.

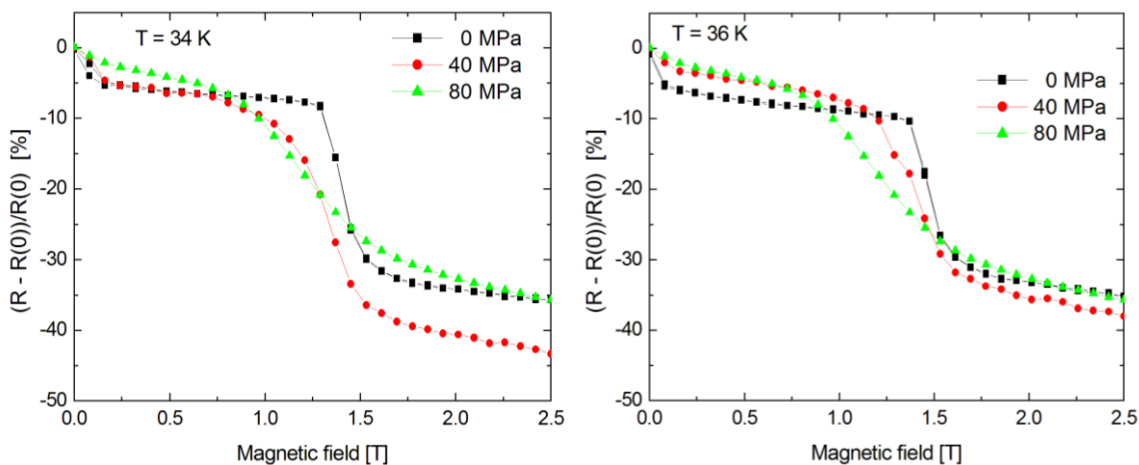


**Fig. 4.45:** Selected magnetoresistance curves of UNiGa measured under the uniaxial compression along the c-axis.

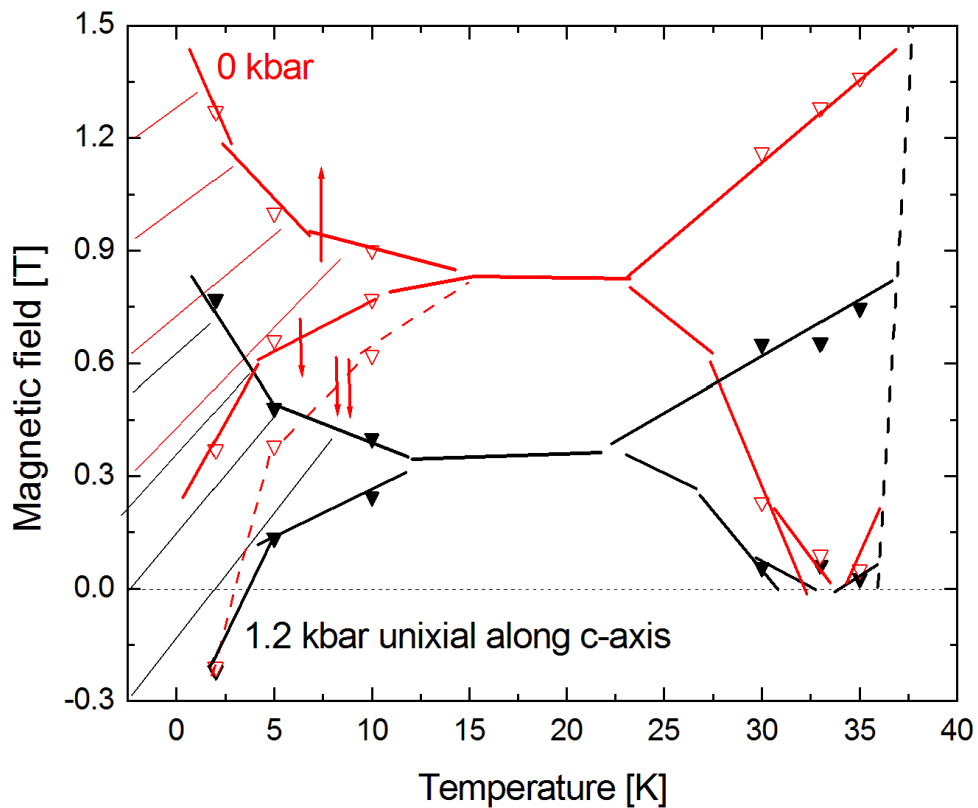
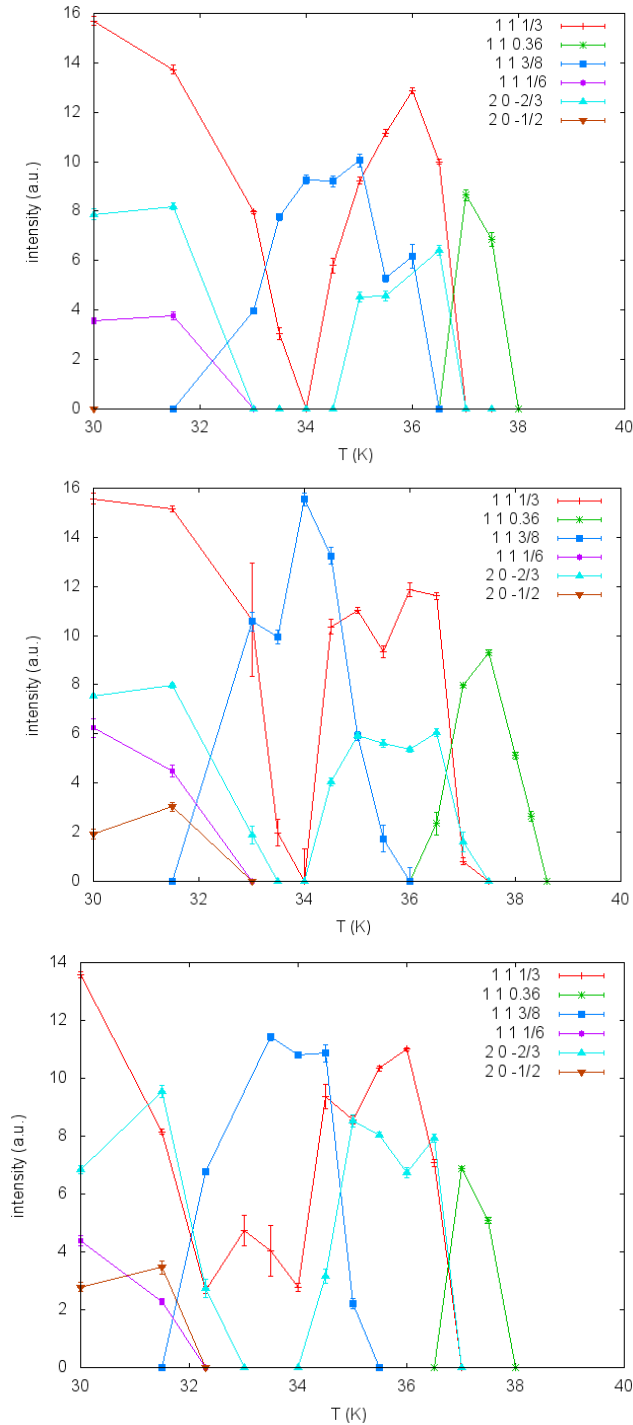


**Fig. 4.46:** Influence of uniaxial compression along the c-axis on the magnetic phase diagram of UNiGa, with the magnetic field applied along the crystallographic c-axis as well. Shaded area denotes the field hysteresis, the red dashed line indicates the second step in the magnetization data, observed only in lower pressures with the removal of the field.

In order to clarify the evolution of the magnetism at the microscopic level the low-temperature neutron single-crystal diffraction experiments at ILL (D10, VIVALDI)



were proposed and performed. Unfortunately, due to unforeseen technical difficulties the important field dependent studies were not performed on the D10 diffractometer and VIVALDI does not have the possibility of magnetic field application. For the neutron

diffractometer experiment, the uniaxial pressure cell described in 4.1.4 has been used. For the experiment on four-circle diffractometer D10, the sample was successfully oriented in the pressure cell. At low temperature only few magnetic satellites were found (due to low signal to noise

ratio), nevertheless at least one magnetic reflection per expected propagation vector was observed. These magnetic reflections were tracked as a function of temperature for all applied pressures and their integrated intensities are depicted in Fig. 4.47.

**Fig. 4.47:** Depiction of the temperature evolution of integrated intensities of observed magnetic reflections at ambient pressure (top), 50 MPa (middle) and 90 MPa (bottom) obtained at the D10 instrument in ILL, Grenoble.

Due to the existence of different propagation vectors and their complex temperature evolution and low intensities, the search of the reciprocal space became unexpectedly time consuming. Nevertheless, some conclusions can be made from the obtained limited data set. Firstly, no new propagation vectors emerge; the evolution of the magnetic phase diagram is smooth, similarly to results in hydrostatic pressures. Secondly, contrary to the hydrostatic case, the presence of the phase characterized by the  $(0,0,1/3)$  propagation vector is extended to a wider temperature interval increasing the separation between the neighboring phases.

In order to get better overall view and exclude emergence of any new phase, the experiment on the VIVALDI diffractometer was performed. The measurements were done using the same pressure cell, the uniaxial pressures up to 100 MPa were applied ( $p_u=0, 10, 50, 90$  MPa). Similarly to the D10 experiment, the application of pressure higher than 100 MPa led to sample destruction (sample breaks to few larger pieces and several smaller grains, preventing the evaluation of obtained data). The evaluation of satellites position revealed that all of them can be described by the previously discussed set of propagation vectors. The detailed investigation of the incommensurate magnetic structure (using methods described in [36]) revealed no change in the propagation vector with application of uniaxial pressure. For the purpose of easier data presentation a cut from the Laue pattern (reciprocal space, respectively) was done, a line going through  $(1-20)$  reflection in the  $(001)$  direction was selected, as all propagation vectors reflect themselves as magnetic satellites in the selected segment (see Fig 4.48).

The results from the VIVALDI experiment are visualized in the same way in the Figs. 4.49 a) – c). At all applied pressures, the observed magnetic satellites were indexed and no new magnetic phase has been observed. In agreement with conclusions from the D10 experiment, the presence of the  $(0,0,1/3)$ -magnetic phase is extended and there are indications of narrowing the interval of the incommensurate phase.

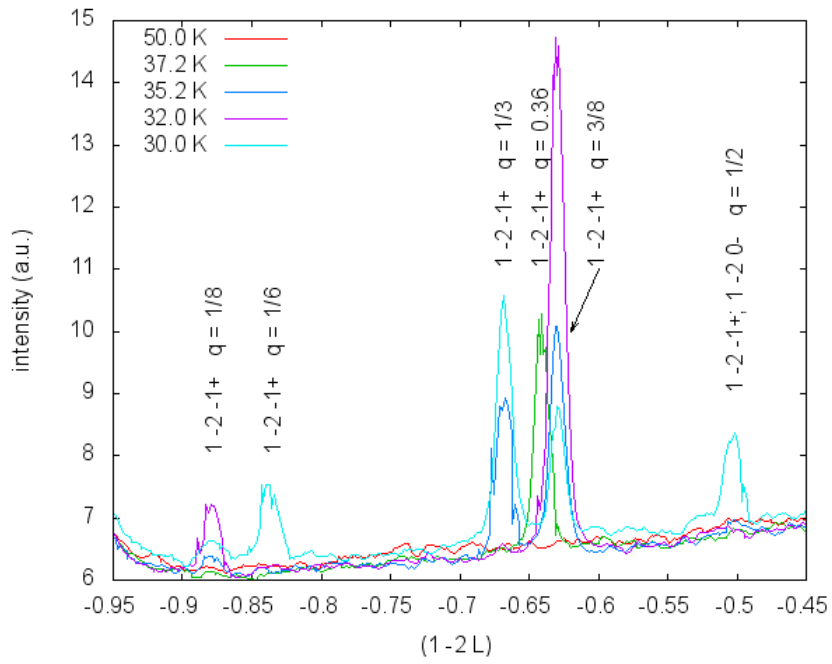


**Fig. 4.48:** The illustrative cut from the VIVALDI patterns at different temperatures along the 00L direction in the reciprocal space with indexation of magnetic satellites,  $q$  denotes the  $L$ -component of the propagation vector  $(0,0,q)$ .

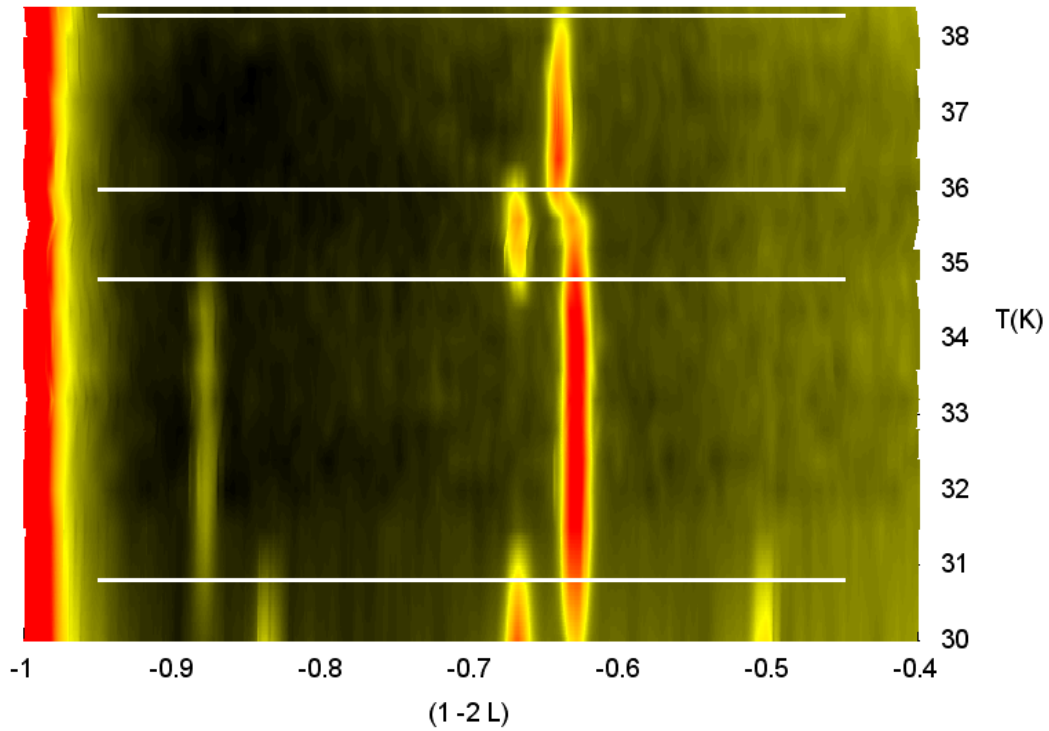


**Fig. 4.49 a)** The temperature dependencies of the selected cut from the VIVALDI diffraction patterns at ambient pressure

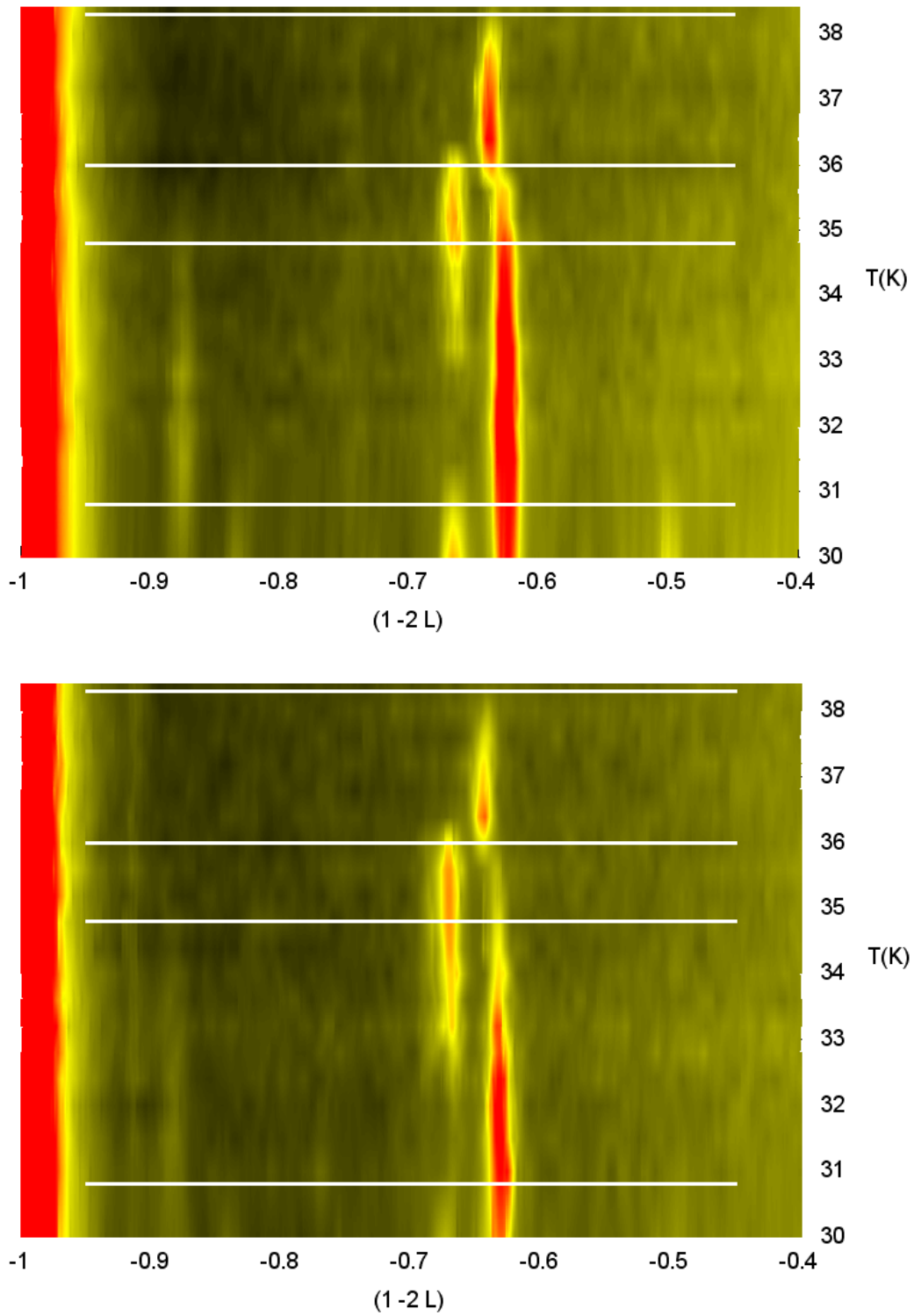


**Fig. 4.49 b)** The temperature dependencies of the selected cut from the VIVALDI diffraction patterns at applied uniaxial pressures 50 MPa (up) and 90 MPa (down). The white horizontal lines serve as a guide for eyes and indicate the transition temperatures at ambient pressure.

### 4.3.3. Conclusions

New single crystal of the UNiGa compound has been grown by the Czochralski method. The quality of the crystal has been checked by the powder x-ray diffraction and the microprobe analysis. Within the accuracy of these techniques, no impurity phases and deviations of ideal 1:1:1 stoichiometry has been detected. The high quality of the single crystal has been confirmed during the neutron diffraction experiments.

Basic characterization of bulk properties at ambient pressure performed on a new UNiGa single crystal well corresponded to data already existing in the literature [16], the antiferromagnetic ordering through the second-order phase transition has been observed at  $T_N \sim 39.5$  K with uranium moments  $\mu \sim 1.4 \mu_B$ . Complicated phase diagram and anomalies in measured properties related to transitions between different AF structures also very well fits the previous results.

First set of experiments under hydrostatic conditions revealed qualitatively similar effects on the magnetic properties of UNiGa as observed in previous works [94, 96]. The ordering temperature  $T_N$  slowly decreases with the applied pressure,  $dT_N/dp \sim -0.3$  K/GPa. As evidenced from the virtually same values of low-temperature saturated magnetization, the value of uranium moments is almost unaffected by pressure. Phases „1“ (incommensurate,  $q = \pm 0, 0, 0.36$ ) and „2“ ( $+ - 0, q = 0, 0, 1/3$ ) are destabilized with the increasing hydrostatic pressure, completely vanishing at  $\sim 0.65$  GPa. The boundary between phase „3“ ( $+ + - + - - + -, q = 0, 0, 1/8$ ) and the „+ + - + - -“ ground state is shifted to lower temperatures, dropping from the ambient pressure value  $\sim 35$  K down to  $\sim 23$  K at  $p = 2.88$  GPa. Judging from the thoroughly explored magnetic phase diagram, the hydrostatic compression clearly promotes the antiferromagnetic coupling of uranium layers, as evidenced mostly by the transition towards the field-induced ferromagnetic state occurring at higher critical fields. Only significant quantitative difference, compared to the previously published results [94], is the much faster pressure-induced shift of the metamagnetic transition  $dB_c/dp \sim +0.7$  T/GPa, which can be ascribed to the high quality of new single crystal.

At high hydrostatic pressures ( $p > 1$  GPa) the remarkable extension of the uncompensated ,+ + - ‘ phase to lower temperature is observed in the  $B$ - $T$  phase

diagram, connected with the suppression of the phase boundary between ‘+ + - + - -’ ground state and the field-forced ferromagnetic state. The behavior on this transition is different in comparison with low pressure one as huge hysteresis is observed, contrary to the low pressure region, where the direct transition between ground and field-induced ferromagnetic states occurs.

DC magnetization, electrical resistivity and the neutron diffraction experiments have been carried out under the uniaxial compression of the UNiGa single crystal along the crystallographic *c*-axis up to  $p = 170$  MPa. Whereas the similarly weak influence on the ordering temperature  $T_N$  and value of uranium magnetic moments has been observed as well, the influence on the magnetic phase diagram revealed fundamental differences, compared to the case of measurements under high hydrostatic pressures. Transition to the field induced ferromagnetic state decreases across the whole temperature range from 2 K to  $T_N$  at a rate  $dB_c/dp \sim -3.8$  T/GPa, regardless of the nature of the (low-field) AF phase at a given temperature. Destabilization of the antiferromagnetic structures and a tendency to form a ferromagnetic ground state is corroborated by the observed hysteresis loops at the lowest temperatures, clearly leaving the remanent magnetization with the removal of the magnetic field.

The differences in observed behavior under hydrostatic and uniaxial pressures can be understood in the context of the magnetostriction measurements at ambient pressure and the previous high pressure study of thermal expansion coefficient. The opposite effect on the value of the critical field and overall evolution of the magnetic phase diagram is in agreement with reported contraction of the lattice in the *c*-axis direction connected with the metamagnetic transition at  $B_c$ . The remarkable difference in the rate of change of the critical field arises from the anisotropy of lattice expansion with varying the temperature and the nature of the hydrostatic and uniaxial conditions. Whereas the first of the above leads to contraction in both, in-plane and *c*-axis directions and reduction of volume, in the case of the later one, the shrinkage along the *c*-axis is accompanied with a small expansion in the perpendicular direction, leaving no (or very small) volume change. From this point of view, the stronger sensitivity to the uniaxial pressure than to the hydrostatic ones is in agreement with the observed shrinkage of the *a*-axis and expansion of the *c*-axis with decreasing the temperature below the  $\sim 70$  K at ambient pressure [96], which

almost cancels out, leaving negligible volume change in the magnetically ordered state.

Data obtained by the neutron diffraction provided in more detail the qualitatively different effect of the uniaxial compression along the c-axis, however, due to the time and technical limitations encountered during the experiments at ILL, the presence of the ferromagnetic ground state under uniaxial compression could not be verified.

This work required the development of several new pressure cells, resp. modification of the existing ones. Our results clearly show successful utilization of various experimental techniques for studying the samples under uniaxial pressure in the broad range of temperatures and magnetic fields.

#### **4.4 Ce<sub>2</sub>PtIn<sub>8</sub> and CeRh<sub>0.75</sub>Pd<sub>0.25</sub>In<sub>5</sub>**

Besides the samples discussed above, which were studied in detail in this work, there were several other samples studied as a part of the broader cooperation. Two of the samples are especially worth mentioning within the context of this thesis. With the introduction of the dilution refrigerator in JLMS, the new and exciting phenomena became accessible. Particularly, the investigation of the possible quantum critical behavior within the novel cerium based heavy fermion systems has been started. Namely, the availability of new single crystals from the Ce<sub>m</sub>T<sub>n</sub>In<sub>3m+2n</sub> group allowed the study of the unconventional superconductivity in the vicinity of the antiferromagnetic quantum critical point, with the high pressure as a driving parameter for the transition.

First of the samples, CeRh<sub>0.75</sub>Pd<sub>0.25</sub>In<sub>5</sub> [97] has been briefly studied as a part of the dilution refrigerator start-up. The goal of the experiment was to elucidate the evolution of the superconducting transition via the resistivity measurement at pressures up to ~ 2.5 GPa in order to get the better overview of the phase diagram. The extended phase diagram, deduced from our experiment is presented in the Fig. 4.50.

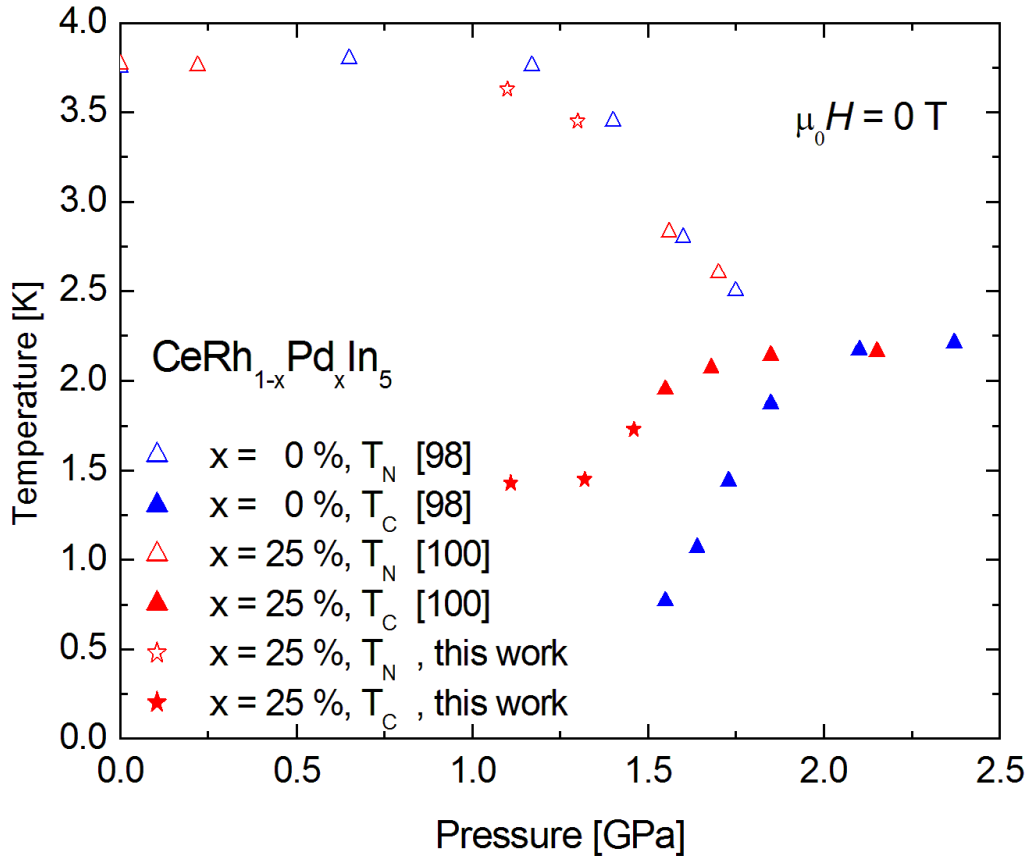


**Fig. 4.50:** Phase diagram of  $\text{CeRh}_{1-x}\text{Pd}_x\text{In}_5$ ,  $x = 0 \%$  and  $25 \%$ .

The second sample, studied in more detail, was the novel member of the  $\text{Ce}_2\text{TIn}_8$  family, the  $\text{Ce}_2\text{PtIn}_8$  compound. The ambient pressure experiments [98, 99] showed the magnetic ordering at  $T_N \sim 1.8 \text{ K}$ , followed by the order to order transition at  $T \sim 1.7 \text{ K}$ , with no signs of superconductivity down to  $T \sim 0.4 \text{ K}$ . The intended result of our pressure study was to confirm the existence of expected [100] superconductivity dome at (relatively) low pressures. In order to obtain the maximum possible information with the available instrumental options, the setup for the simultaneous measurement of the resistivity and AC susceptibility has been prepared. Thin golden wires ( $25 \mu\text{m}$ ) have been spot-welded on the sample for the resistivity measurement. AC susceptibility used the home-built detection coil set, introduced in 4.1.1. Only modification for the low-temperature experiment was the use of superconducting NbTi wire for the primary coil instead of the copper. This allowed us to use higher amplitudes of the AC excitation field (and subsequently

better sensitivity) without generating any excessive heating in the sample area. Sample has been oriented and fixed inside the detection coil-set with the applied magnetic field along the crystallographic  $c$ -axis, which is the easy magnetization direction of the  $\text{Ce}_2\text{PtIn}_8$ .

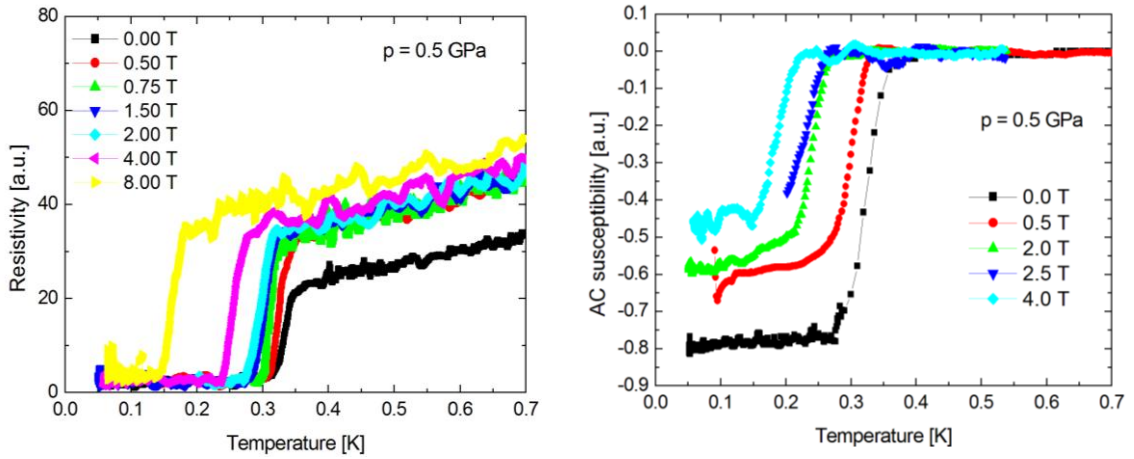


**Fig. 4.51:** Resistivity (left) and AC susceptibility (right) of  $\text{Ce}_2\text{PtIn}_8$  under the pressure 0.5 GPa.

The AC susceptibility and electrical resistivity of the  $\text{Ce}_2\text{PtIn}_8$  sample has been measured simultaneously down to  $T \sim 40$  mK with the magnetic fields up to  $\mu_0 H = 9$  T. The results are very recent and their evaluation is still ongoing. Nevertheless, the superconducting transition was clearly visible on both measured quantities and the presence of the dome has been confirmed. Examples of the measured resistivity and AC susceptibility curves are displayed in Fig. 4.51. The obtained magnetic phase diagram is shown in the Fig. 4.52, indicating the critical field of the superconducting transition of the order of several tesla. The magnetic transitions seem to be strongly suppressed, no visible features on the measured data, indicating the magnetic ordering, has been observed even at the lowest (non ambient) pressure. In order to clarify the evolution of the magnetic transition phase boundary and shed some light on the possible presence of the quantum criticality, a new pressure experiment is currently under preparation.



## Chapter 5 Conclusions

This work has been focused on the experimental study of magnetic and thermodynamic properties of selected intermetallic compounds of 4f (lanthanides) and 5f (uranium) elements, subjected to the combination of low-temperatures, high magnetic fields and most importantly the high pressures. The results presented in this thesis can be divided into two main categories. First major subject lies in the advances in high pressure instrumentation. This area can be divided into three main goals:

- (1) Extension of the existing experimental options with pressure cells already available in the JLMS in the „moderate range“ of high hydrostatic pressures 1 – 3 GPa.
- (2) Extension of achievable pressures to very high (above 10 GPa) by means of constructing new diamond anvil-type pressure devices.
- (3) Creating the experimental options for studying the properties of materials under uniaxial stress along selected direction instead of the hydrostatic compression.

Most of the outlined instrumentation goals have been successfully achieved, obtained results can be covered in the following way:

- (1) We implemented the techniques for measuring the AC susceptibility and specific heat capacity under pressures up to  $\sim 3$  GPa in wide range of temperatures (1.8 K – 350 K) and high magnetic fields up to  $B = 14$  T. Both methods were exploited in the research of the pressure influence on the magnetic properties of several samples from the  $\text{RCO}_2$  group of compounds (obtained results are discussed further in the text). These experiments demonstrated excellent performance of both of them. Namely, in the case of AC susceptibility measurements, the arrangement with the detection coilset fitted inside the pressure cell lead to the very high filling factor and

consequently excellent sensitivity of measurement. Compared to usual approach of fitting entire pressure cell inside a commercial magnetometer, the background signal originating from the body of the pressure cell is no longer an issue. It is, however, fair to note that due to their one-off usability, the calibration of the coils is not possible and we can at this point obtain only relative values of measured susceptibility.

(2) We designed and built the diamond anvil cell for the magnetization measurements in the commercial SQUID magnetometer (Quantum Design). Despite the substantial geometrical restrictions presented by dimensions of sample chamber of the magnetometer and limited choice of materials, we managed to create fully functional pressure cell. Performance of the new cell has been demonstrated on two of the most usual pressure standards – the pressure induced shifts of the superconducting transition of pure lead and a luminescence lines of ruby. The tests on these pressure standards and first experiments with sample of the ferromagnetic invar alloy  $\text{Fe}_{64}\text{Ni}_{36}$  proved excellent efficiency of new pressure cell in terms of both, capability of achieving very high pressures and the sensitivity and precision of obtained magnetization data. Achieved pressures 14 – 15 GPa exceeded the targeted maximum pressure and a clear signal from extremely tiny samples have been observed ( $\sim 10 \mu\text{g}$  of lead, resulting in total moment  $\sim 10^{-6}$  emu). To our best knowledge, there is only one other facility in the world possessing the pressure cell with similar abilities [44].

(3) Series of uniaxial pressure cells for measuring DC magnetization, AC susceptibility, electrical resistivity and neutron diffraction of studied single crystals has been built. This experimental arrangement is particularly tempting in the research of the materials displaying pronounced anisotropy of physical properties. In addition, two interchangeable internal setups allowing the different pressure vs. cell axis orientation have been built for the magnetization and neutron diffraction pressure cells. This is an important option enabling us to choose from the variety of combinations of the directions of applied stress with respect to the direction of applied magnetic field (and/or the scattering vector).

The magnetization, electrical resistivity, AC susceptibility and specific heat of the ErCo<sub>2</sub> sample has been measured under the hydrostatic pressures up to 3 GPa. All types of measurements consistently displayed the decrease of the ferrimagnetic ordering temperature  $dT_C/dp \sim -6.85$  K/GPa in the pressures up to  $\sim 1.7$  GPa ( $T_C \sim 33$  K at ambient pressure). Observed small increase of the saturated magnetization leads to a conclusion of gradual suppression of the Co moment (Er and Co are antiparallel) at a rate  $d\mu_{Co}/dp \sim -0.126$   $\mu_B$ /GPa. Above the 1.7 GPa pressure, more complex behavior has been observed. The AC susceptibility peak at  $T_C$  splits into two peaks, one of them following the same  $dT_C/dp$  rate as in lower pressure region and the other one following slower rate  $dT_C/dp \sim -3$  K/GPa. This observation corroborates the previously proposed scenario of decoupling of the magnetic ordering of the Er and Co sublattices [78]. The loss of temperature hysteresis confirms the change of the order of the transition from the 1<sup>st</sup> to 2<sup>nd</sup> type, which has been predicted as well. Important result, obtained with the new high pressure AC susceptibility setup, is the observation of the tiny anomaly in the paramagnetic regime of ErCo<sub>2</sub>, which is related to the onset of paramagnetism. The small peak-like feature has been visible on the AC susceptibility curves at the „flipping temperature“  $T_f$  ( $\sim 98$  K at ambient pressure) in the entire pressure range up to  $\sim 3$  GPa and a linear decrease of its position  $dT_f/dp \sim -3.4$  K/GPa has been observed. The remarkable similarity of pressure induced changes of  $T_C$  and  $T_f$  suggest that the two phenomena are intimately connected. Our results also clearly demonstrated that the paramagnetic state is rather robust, surviving the application of highest pressures, despite the almost unnoticeable features on the bulk properties data, related to this effect.

Samples with small substitution of silicon on the cobalt site were studied to compare the influence of high pressures on the electronic properties of parent compounds to the „dilution“ of magnetic Co sublattice. Our study of the diluted Er(Co<sub>0.975</sub>Si<sub>0.025</sub>)<sub>2</sub> compound confirmed that even very small substitution of Si for Co has a dramatic effect on magnetic properties of ErCo<sub>2</sub>.  $T_C$  increased from 33.5 K to 43 K, whereas the  $T_f$  dropped from the 98 K to 74 K. Faster saturation of the low-temperature  $M(H)$  curves, considerably sharper transition at  $T_C$  observed in the  $M(T)$  measurements and namely the missing upturn above  $T_C$  in the resistivity data suggest

much weaker role of spin fluctuations in the substituted system. The behavior observed under high pressures is also rather different than in  $\text{ErCo}_2$ . The qualitative character of the resistivity curves remain intact by the pressure and no apparent splitting of the AC susceptibility data at  $T_C$  has been observed. The obtained results clearly point to a conclusion that magnetism of the cobalt sublattice is stabilized with the silicon substitution. One similarity between both systems can, however, be observed. The change in the slope  $dT_C/dp$  from  $\sim -10$  K/GPa to  $\sim -3.2$  K/GPa appears at a pressure  $p \sim 1.7$  GPa, almost identically to the parent  $\text{ErCo}_2$  sample. Concerning the paramagnetism phenomenon, the decrease of the flipping temperature  $T_f$  is observed in the Si substituted sample as well. To conclude the microscopic nature of the observed effects, the XMCD and SANS experiments under high are highly desired.

In the  $\text{HoCo}_2$  and  $\text{Ho}(\text{Co}_{0.0975}\text{Si}_{0.025})_2$  samples, the decrease of the ordering temperature has been observed, with the rates  $dT_C/dp = -12.3$  K/GPa and  $dT_C/dp = -12.8$  K/GPa, respectively. The anomalous bump at the AC susceptibility data, reflecting the cobalt clustering and the onset of paramagnetism has been observed at  $T_f = 125$  K and  $T_f = 117$  K, respectively. In addition, one more transition at  $T_{f2} = 148$  K has been observed in  $\text{Ho}(\text{Co}_{0.975}\text{Si}_{0.025})_2$ . In addition to the ferimagnetic ordering at  $T_C$  and paramagnetism phenomenon around the  $T_f$ , the spin reorientation from the [100] to [110] easy direction of magnetization occurs in the  $\text{HoCo}_2$  at  $T_R = 16.5$  K at ambient pressure. With the 2.5 % silicon substitution, the spin reorientation temperature  $T_R$  shifts to lower temperatures  $\sim 9.1$  K. Preliminary measurements of the sample with higher content of the silicon (7.5 %) have shown further decrease of  $T_R$  ( $\sim 5$  K), suggesting the complete suppression of the spin reorientation effect for silicon concentrations  $\sim 20$  %. On the other hand, the pressure induced change of the  $T_R$  remains almost identical for the parent and the 2.5 % substituted sample,  $dT_R/dp \sim +4$  K/GPa in both cases.

The development of the complicated magnetic phase diagram of  $\text{UNiGa}$  has been studied under hydrostatic pressures up to 3 GPa and the uniaxial compression up to 170 MPa applied along the c-axis of the hexagonal crystal structure. Under the hydrostatic pressures, the data obtained in lower pressures below 1 GPa fits very well with existing literature in the same pressure range in almost all aspects. The mild decrease of Neel temperature  $T_N$  and no significant change of the uranium magnetic

moment has been observed. Applied pressure gradually reduced the temperature range of existence of the two AF phases (out of six existing at the ambient pressure), simplifying the phase diagram in pressures above  $\sim 0.65$  GPa. Observed increase of the critical field  $dB_c/dp \sim +0.7$  T/GPa (consistent in entire temperature range below  $T_N$ ) suggest the promotion of the antiferromagnetic coupling of the uranium layers in UNiGa. The only observed difference, compared to previous results – much faster increase of the  $B_c$  with pressure – can be ascribed to the quality of newly grown single crystal. Our resistivity measurements extended the previous studies to pressures up to 3 GPa. Similar trends have been observed, i.e. further increase of the critical field of the metamagnetic transition  $B_c$  and only small influence on the uranium moments and  $T_N$ . At high hydrostatic pressures ( $p > 1$  GPa) the remarkable extension of the uncompensated  $,++-$  phase to lower temperatures has been observed, related to the suppression of the phase boundary between  $,++- - -$  ground state and the field-forced ferromagnetic state.

DC magnetization, electrical resistivity and the neutron diffraction techniques have been used to study the UNiGa sample under the uniaxial compression along the c-axis. Similarly weak influence on  $T_N$  and magnetic moment value has been observed as well. However, the effect on the magnetic phase diagram is fundamentally different compared to the hydrostatic case. We observe the tendency to destabilize the antiferromagnetic structures and form the ferromagnetic ground state when applying the uniaxial pressure. Transition to the field forced ferromagnetic state decreases with the increased compression across the whole temperature range from 2 K to  $T_N$  at a rate  $dB_c/dp \sim -3.8$  T/GPa (order of magnitude larger compared to the hydrostatic pressures), regardless of the nature of the (low-field) AF phase at a given temperature. The qualitatively different influence of the uniaxial and hydrostatic pressures can be explained in the following way. Whereas the hydrostatic pressure leads to contraction in both, a-axis and c-axis directions and reduction of volume, in the case of the uniaxial pressure, the shortening along the c-axis is accompanied by a small expansion in the perpendicular direction, leaving no (or very small) volume change. From this point of view, the stronger sensitivity to the uniaxial pressure than to the hydrostatic ones is in agreement with the observed shrinkage of the a-axis and expansion of the c-axis with decreasing the temperature below the  $\sim 70$  K at ambient pressure [], which almost cancels out, leaving negligible volume change in the magnetically ordered state. Observed contraction of the lattice

in the c-axis direction at the metamagnetic transition at  $B_c$  is in agreement with the tendency to form a ferromagnetic ground state, deduced from our work.

Variety of different experimental techniques, used in this study required significant improvements in the high pressure instrumentation. This work showed the successful utilization of the new pressure cells for the magnetization measurements in the commercial SQUID magnetometer, electrical resistivity and the neutron diffraction experiments. Very recent experiments in the new dilution refrigerator in JLMS showed the feasibility of experiments under the combination of very high pressures and very low temperatures. In the first preliminary measurements with the new apparatus, the properties of the novel superconductor  $Ce_2PtIn_8$  has been probed by resistivity and AC susceptibility measurements, confirming the existence of the „superconducting dome“ around the antiferromagnetic quantum critical point at a pressure of  $\sim 1.25$  GPa.

## Bibliography

- [1] [www.betsa.fr](http://www.betsa.fr)
- [2] [www.easylab.co.uk](http://www.easylab.co.uk)
- [3] Weiss P. (1907) *J. de Physique* **6** 667
- [4] Pauli W. (1927) *Z. Phys* **41** 81
- [5] Mott N. F. (1935) *Proc.Phys. Soc.* **47** 571
- [6] Ashcroft N. W., Mermin N. D. (1976) *Solid State Physics*, Cornell University
- [7] Stoner E. C (1936) *Proc. Roy. Soc. A* **154** 656
- [8] Wolfarth E. P., Rhodes P. (1962) *Phil. Mag.* **74** 1817
- [9] Shimizu M. (1982) *J. de Physique* **43** 155
- [10] Yamada H. (1993) *Phys. Rev. B* **47** 11211
- [11] Shimizu M. (1981) *Rep. Prog. Phys.* **44** 329
- [12] Kittel Ch (2005) *Introduction to Solid State Physics 8<sup>th</sup> edition*, J. Wiley and Sons Inc.
- [13] Blundell S. (2001) *Magnetism in Condensed Matter*, Oxford University Press
- [14] O’Handley R.C. (2000) *Modern Magnetic Materials*, John Wiley & Sons, 2000
- [15] Hill H. (1971) *Plutonium and other actinides*, AIME, New York
- [16] Sechovský V., Havela L. (1998) *Magnetism of ternary intermetallic compounds of uranium (in Handbook of Magnetic Materials 11)*, Elsevier Science,
- [17] Bradley R. S.(Edt.) (1969) *Advances in High Pressure Research 1 -3*, Academic Press
- [18] Arnold Z. (1999) *High pressure in basic and material science*, Inst. Of Phys. ASCR, Prague
- [19] <http://kfes-80.karlov.mff.cuni.cz/techlab/tech/>
- [20] [www.vakuum.cz](http://www.vakuum.cz)
- [21] Pospíšil J (2011) *Electronic properties and structure of selected rare earth and uranium compounds; influence of impurities*, PhD Thesis, Charles University in Prague, Prague
- [22] Uhlířová K. (2010) *Single crystal studies of novel strongly correlated electron compounds*, PhD thesis, Charles University in Prague, Prague
- [23] Rodriguez-Carvajal J. (1993) *Phys B* **192** 55

- [24] Rietveld H. M. (1969) *Journal of Applied Crystallography* **2** 65
- [25] [www.qdusa.com](http://www.qdusa.com)
- [26] <http://www.qdusa.com/techsupport/softwareUpgrades.html>
- [27] Kamarád J., Machátová Z., Arnold Z. (2004) *Rev. Sci. Inst.* **75** 5022
- [28] Bridgman P. W. (1949) *The Physics of High Pressure*, G. Bell and Sons Ltd., London
- [29] Sherman W. F., Stadtmuller A. A. (1987) *Experimental techniques in high pressure research*, John Wiley & Sons, New York
- [30] <http://www.ngkmetals.com>
- [31] Rajput J. S. (1970) *Solid State Commun.* **8**, 711
- [32] Baruchel J., Hodeau J. L., Lehmann M. S, Regnard J. R., Schenkler C. (Eds.) (1994) *Neutron and synchrotron radiation for condensed matter studies Vol. I*, Springer-Verlag, Berlin
- [33] Valvoda V., Polcarová M., Lukáč P. (1992): *Základy strukturní analýzy*, Karolinum, Praha
- [34] Brückel T., Heger G., Richter D., Zorn R. (Eds.) (2001) *Neutron Scattering*, Forschungszentrum Jülich GmbH, Jülich
- [35] Campbell J. W., Hao Q., Harding M. M., Nguti N. G., Wilkinson C. (1998) *J. Appl. Crystallogr.* **31** 496
- [36] Prokleška J. (2008) *Cohesive and magnetoelastic properties of materials with strongly correlated electrons*, PhD Thesis, Charles university in Prague, Prague
- [37] Sullivan P. F., Seidel G. (1968) *Phys. Rev.* **173** 679
- [38] Kraftmakher Y. (2004) *Modulation Calorimetry: Theory and Applications*, Springer – Verlag, Berlin
- [39] Holmes A. T., Jaccard D. (2006) *Phys. B* **378-80** 339
- [40] Tomioka F., Umehara I., Ono T., Hedo M., Uwatoko Y., Kimura N. (2007) *Jpn J. Appl. Phys.* **46** 3090
- [41] Kubota O., Nakazawa Y. (2008) *Rev. Sci. Ins.* **79** 053901
- [42] Eremets M. I. (1996) *High Pressure Experimental Methods*, Oxford University Press
- [43] Mito M., Hitaka M., Kawae T., Takeda K., Kitai T., Toyoshima N. (2001) *Jpn. J. Appl. Phys.* **40** 6641
- [44] Alireza P. L., Lonzarich G. G. (2009) *Rev. Sci. Ins.* **80** 023906

- [45] Girit G., Wang W., Atfield J. P., Huxley A. D., Kamenev K. V. (2010) *Rev. Sci. Instr.* **81** 073905
- [46] Vettier C., Bloch D., Paureau J., Yelon W. B. (1975) *Rev. Phys. Chem. Jpn, Suppl 1* 369
- [47] Kouvel J. S., Wilson R. H. (1961) *J. Appl. Phys.* **32** S276
- [48] Kamarád J., Arnold Z., Schneider J., Krupička S. (1980) *J. Magn. Magn. Mater.* **15** 1409
- [49] Koyama K., Hane S., Kamashima K., Goto T. (1998) *Rev. Sci. Instr.* **69** 3009
- [50] Herrero-Albillos J., Bartolome F., Garcia L. M., Campo J., Young A. T., Funk T., Cuello G. J. (2007) *J. Magn. Magn. Mater.* **310** 1645
- [51] Herrero-Albillos J., Garcia L. M., Bartolome F., Young A. T., Funk T. (2007) *J. Magn. Magn. Mater.* **316** E442
- [52] Herrero-Albillos J., Bartolome F., Garcia L. M., Young A. T., Campo T., Cuello G. J. (2007) *Phys. Rev. B* **76** 094409
- [53] Turčinková D. (2008) *Pressure influence on magnetic parameters of intermetallic compounds*, Diploma thesis, Charles University, Prague
- [54] Bundy F. P. (1961) *J. Appl. Phys.* **32** 483
- [55] [www.anbesmt.co.jp](http://www.anbesmt.co.jp)
- [56] <http://www.lakeshore.com/Documents/F037-00-00.pdf>
- [57] Eremets M. I., Timofeev T. A. (1992) *Rev. Sci. Instr.* **63** 3123
- [58] <http://www.almax-industries.com/>
- [59] [www.apiezon.com](http://www.apiezon.com)
- [60] Nataf L., Decremps F., Chervin J. C., Mathon O., Pascarelli S., Kamarád J., Baudelet F., Congeduti A., Itie J. P. (2009) *Phys. Rev. B* **80** 134404
- [61] Sidorov V. A., Sadykov R. A. (2005), *J. Phys.: Condens. Matter* **17** 3005
- [62] Yokogawa K., Murata K., Yoshino H., Aoyama S. (2007) *Jpn. J. Appl. Phys.* **46** 3636
- [63] Beznosov A. B., Desnenko V. A., Fertman A. L., Ritter C., Khalyavin D. D. (2003) *Phys. Rev. B* **68** 054109
- [64] Yamamizu T., Endo M., Kimura N., Aoki H. (2004) *Phys. Rev. B* **69** 014423
- [65] Takeshita N., Sasagawa T., Sugioto T., Tokura Y., Takagi H. (2004) *J. Phys. Soc. Jpn.* **73** 1123
- [66] Alireza P. L., Julian S. R. (2003) *Rev. Sci. Instr.* **74** 4728

- [67] Haase J., Goh S. K., Meissner T., Alireza P. L., Rybicki D. (2009) *Rev. Sci. Inst.* **80** 073905
- [68] Settai R., Kubo T., Shiromoto T., Honda D., Shishido H., Sugiyama K., Haga Y., Matsuda T. D., Betsuyaku K., Harima H., Kobayashi T. C., Onuki Y., *J. Phys. Soc. Jpn.* **74** 3016
- [69] Giorgetti C., Dartyge E., Baudelet F., Galera R. M. (2004) *Phys. Rev. B* **70** 035105
- [70] Garcia F., dos Santos H., Soares M. R., Takeuchi A. Y., da Cunha S. F. (1998) *J. Appl. Phys.* **83** 6969
- [71] Garcia F., Soares M. R., Takeuchi A. Y., da Cunha S. F. (1998) *J. Alloy. Compd.* **279** 117
- [72] Goto T., Fukamichi K., Sakakibara T., Komatsu H. (1989) *Solid State Commun.* **72** 945
- [73] Goto T., Katori H. A., Sakakibara T., Mitamura K., Fukamichi K., Murata K. (1994) *J. Appl. Phys.* **76** 6682
- [74] Cuong T. D. (1998) *Magnetism and related properties of RECo<sub>2</sub> compounds: Co – dilution*, PhD Thesis, Charles University in Prague, Prague
- [75] Syshchenko O., Fujita T., Sechovský V., Diviš M., Fujii H., *J. Magn. Magn. Mater.* **226** 1062
- [76] Syshchenko O. (2002) *Anomalous phenomena connected with the phase transitions in intermetallics*, PhD Thesis, Charles University in Prague, Prague
- [77] Khmelevskiy S., Mohn P. (2000) *J. Phys.: Condens. Matter* **12** 9453
- [78] Hauser R., Bauer E., Gratz E., Muller H., Rotter M., Michor H., Hilscher G., Markosyan A. S., Kamishima K., Goto T. (2000) *Phys. Rev. B* **61** 1198
- [79] Cuong T. D., Duc N. H., Brommer P. E., Arnold Z., Kamarád J., Sechovský V (1998) *J. Magn. Magn. Mater.* **182** 143
- [80] Syshchenko O., Fujita T., Sechovský V., Diviš M., Fujii H. (2001) *J. Alloy. Compd.* **317** 438
- [81] Hauser R., Bauer E., Gratz E. (1998) *Phys. Rev. B* **57** 13929
- [82] Bonilla C. M., Calvo I., Herrero-Albillos J., Figueroa A. I., Castan-Guerrero C., Bartolome J., Rodriguez-Velamazan J. A., Schmitz D., Weschke E., Paudyal D., Pecharsky V. K., Gschneidner K. A., Bartolome F., Garcia L. M. (2012) *J. Appl. Phys.* **111** 07E315

- [83] Prokleška J. (2003) *Magnetoelastické jevy ve sloučeninách  $Er(Co,X)_2$ ,  $X = p$ -element*, Diploma Thesis, Charles University in Prague, Prague
- [84] Cuong T. D., Duc N. H., Brommer P. E., Arnold Z., Kamarád J., Sechovský V. (1998) *J. Magn. Magn. Mater.* **182** 143
- [85] Baranov N. V., Kozlov A. I. (1992) *J. Alloy. Compd.* **190** 83
- [86] Cooper R., Siemann R., Yang D., Thayamballi P., Banerjea A. (1985) *Handbook on the Physics and Chemistry of Actinides 2*, Elsevier Science
- [87] Andreev A. V., Deryagin A. V., Yumaguzhin R. Yu. (1984) *Sov. Phys. JETP* **59** 1082
- [88] Andreev A. V., Zelený M., Havela L., Hřebík J. (1984) *Phys. Status Solidi* **81** 307
- [89] Palstra T. T. M., Nieuwenhuys G. J., Vlastuin R. F. M., van den Berg J., Mydosh J. A. (1987) *J. Magn. Magn. Mater.* **67** 331
- [90] Zelený M., Schreiber J., Kobe S. (1985) *J. Magn. Magn. Mater.* **50** 27
- [91] Brück E. (1991) *PhD Thesis*, University of Amsterdam
- [92] Prokeš K., Gukasov A., Javorský P., Sechovský V., Mihalik M. (2001) *Phys. B* **301** 255
- [93] Prokeš K., Feyerherm R., Dudzik E., Sechovský V., Mihalik M. (2011) *J. Phys.: Condens. Matter* **23** 076001
- [94] Honda F., Oomi G., Andreev A. V., Havela L., Prokeš K., Sechovský V. (1997) *Phys. B* **239** 109
- [95] Sechovský V., Havela L., Jirman L., Brück E., de Boer F. R., Nakotte H., Ye W., Takabatake T., Fujii H., Suzuki T., Fujita T. (1992), *Phys. B* **177** 155
- [96] Honda F., Prokeš K., Olšovec M., Bourdarot F., Burlet P., Kagayama T., Oomi G., Havela L., Sechovský V., Andreev A. V., Brück E., de Boer F. R., Menovský A. A., Mihalik M. (1998) *J. Alloy. Compd.* **271** 495
- [97] Kratochvílová M., et al (2011) *Česko-Slovenská studentská konference*, Košice
- [98] Kratochvílová M., et al (2012), submitted to *Phys. Rev. B*
- [99] Kratochvílová M., et al (2012), *International Conference on Magnetism 2012*, Busan, South Korea
- [100] Pfeleiderer Ch. (2009) *Rev. Mod. Phys.* **81** 1551

## List of publications:

- [1] Prchal J., Naka T., Míšek M., et al. (2007), Magnetic disorder in  $RNi_{1-x}Cu_xAl$  compounds: *J. Magn. Magn. Mater.* **316** E499
- [2] Míšek M., Arnold Z., Isnard O., et al (2008): Magnetic and transport properties of  $CeCo_{12}B_6$  and  $CeFe_2Co_{10}B_6$  compounds under pressure, *Acta Phys. Pol. A* **113** 263
- [3] Skorokhod Y., Arnold Z., Isnard O., Míšek M., et al. (2008): Transport properties of  $CeCo_{12}B_6$  in vicinity of phase transition, *Acta Phys. Pol. A* **113** 259
- [4] Prokleška J., Míšek M., Sechovský V., et al (2009): Magnetic phase transitions in CePtSn under ambient and hydrostatic pressures, *J. Appl. Phys.* **105** 07E106
- [5] Míšek M., Prokleška J., Javorský P., et al (2009): Magnetoresistance in CePtSn under high hydrostatic pressures, *J. Alloy. Compd.* **480** 147
- [6] Míšek M., Sechovský V., Kamarád J., et al (2010): Effects of high pressures on magnetism in UNiGa, *High Press. Res.* **30** 8
- [7] Prchal J., Míšek M., Isnard O. (2010): Field-induced magnetic ordering in  $ErNi_{1-x}Cu_xAl$ , *J. Phys.: Conf. Series* **251** 012022
- [8] Míšek M., Prokleška J., Kamarád J., et al (2010): Magnetization of UNiGa under pressure, *IOP Conf. Series-Mat. Sci. Eng.* **9** 012052
- [9] Prokleška J., Detlefs B., Sechovský V., Míšek M., et al (2010): Peculiarities of the magnetic-history-dependent phase in CePtSn, *J. Magn. Magn. Mater.* **322** 1120

- [10] Arnold Z., Isnard O., Mayot H., Míšek M., et al (2010): Pressure effect on magnetic properties of  $\text{RCo}_{12}\text{B}_6$  (R=Y,Ce) compounds, *J. Magn. Magn. Mater.* **322** 1117
- [11] Kamarád J., Míšek M., Prokeš K., Mat'áš S., Arnold Z. (2011): Effect of uniaxial pressure on helimagnetic structure of  $\text{Lu}_2\text{Fe}_{17}$ , *J. Phys.: Conf. Series* **340** 012067
- [12] Míšek M., Prokleška J., Sechovský V., Turčinková D., Prchal J., Kusmartseva A. F., Kamenev K. V., Kamarád J. (2012): Effects of High Pressure on the Magnetism of  $\text{ErCo}_2$ , *J. Appl. Phys.* **111** 07E132
- [13] Arnold Z., Isnard O., Mayot H., Skorokhod Y., Kamarád J., Míšek M. (2012): Magnetic properties of  $\text{GdCo}_{12}\text{B}_6$  compound under high pressure, *Solid State Commun.* **152** 1164
- [14] Fikáček J., Prokleška J., Custers J., Míšek M., Daniš S., Prchal J., Sechovský V., Císařová I. (2012): Physics of polymorphic transition in  $\text{CeRuSn}$ , *Phys. Rev. B* **86** 054108